Computer modelling of crack growth in rubber-toughened polymers.

SAURON, Alain.

COMPUTER MODELLING OF CRACK GROWTH IN RUBBER-TOUGHENED POLYMERS

ALAIN SAURON

A thesis submitted in partial fulfilment of the requirements of
Sheffield Hallam University
for the degree of Doctor of Philosophy

December 1997

Materials Research Institute, Sheffield Hallam University
in collaboration with ICI Research & Technology Centre, Wilton (UK).

Abstract

We present results from a computer modelling study of fracture propagation in a rubber-toughened polymer subject to external uniaxial tension. Using a simple lattice model comprising two bond types (one for rubber and one for polymer), simulations have been performed on both 2- and 3-dimensional systems. Each bond is characterised by two parameters : an elastic constant and a mechanical strength. All bonds behave in a purely elastic manner up to fracture; this limits the model's applicability to impact failure of brittle glassy polymers. We employ a stochastic breaking process based on Eyring's reaction rate theory, and allow the system to equilibrate fully after each bond breakage. It is found that the Conjugate Gradient method is the most efficient technique for calculating these equilibria. The model allows straightforward measurement of the total damage at failure, which is a crude approximation of the material toughness, and the stress distribution during the damage evolution.

We show that, for a wide range of bond parameters, as the rubber loading is increased the damage goes through a sequence of behaviour : embrittlement; toughening; saturation; and weakening. This sequence is consistent with experimental data for rubber-toughened Poly(methyl methacrylate) (RT-PMMA). Our results show that the embrittlement and saturation stages are sensitive to the ratio of the two elastic constants but that they disappear as this ratio approaches unity. The toughening achieved is sensitive to both the concentration and the mechanical strength of the rubber bonds, the most damaged systems being those with large rubber mechanical strength at approximately 50% concentration. We also find that the damage is dependent on the spatial distribution of the rubber bonds, the greatest toughness being achieved using a homogeneous rubber distribution.

We also find that the evolution of the system's failure goes through four regimes. In the first of these, the damage is evenly distributed throughout the system but shows a propensity for occuring adjacent to rubber bonds. Subsequently, short cracks develop between some of these weakly damaged sites. As more of these develop, a number of long rubber-bridged cracks appear. In the third regime, the stabilising effect of the bridging rubber bonds forces the damage to extend throughout the system, leading to branching and interconnecting of rubber-bridged cracks. Finally, the stress experienced by the crack-bridging rubber bonds becomes unsustainable and catastrophic failure occurs. Zones of material consistent with each of these four regimes can be observed in experimentally fractured RT-PMMA. The main toughening mechanisms in operation in our model are, therefore, crazing (which occurs mainly in the second regime) and rubber-bridging (which occurs in the third). The former is enhanced by using a lower rubber elastic constant, whereas the latter is prolonged by a large rubber mechanical strength.

We also apply the model to simulations of 2D and 3D systems containing rubber macro-particles, i.e. large volumes of connected rubber bonds, and we present visual results of the damage and the stress field evolution in such systems. In these, the damage appears to develop in accordance with the four regimes described above. The stress maps of multi-particle 2D systems show the gradual stress transfer which takes place as cracks develop, from initially high-stressed inter-particle polymer regions to the crack tips and, then, to the rubber particles along the crack lines. These visual results also highlight three possible modes of particle-crack interaction : particle debonding, particle splitting and crack reflection.

Acknowledgments

I would like to thank my supervisors, Prof C.M. Care and Dr D. Cleaver for advice and guidance throughout this project; I would also like to thank Dr R. Ettelaie, from ICI Wilton, for his invaluable help and advice on the subject of rubber-toughened polymers and for his comments on the draft of this thesis.

I am also indebted to all my colleagues and friends at the University, to those who have already known the torments of writing up, and to those who will soon...

Finally, I am grateful to my mother and my sister whose unreserved moral support made this project achievable.

Contents

Chapter 1

Introduction

1.1 Aims

Glassy polymers are used in a wide range of engineering applications. Unfortunately, unmodified glassy polymers are very brittle and, therefore, are frequently toughened by the addition of rubber particles. Such modified polymers are indeed experimentally more impact resistant than unmodified ones, without significant loss of their other engineering properties. Fracture initiation, crack growth and toughening mechanisms in this kind of composite material are still to be fully understood. Because such materials are two-component and because damage under tensile loads occurs throughout their bulk and not just at the crack tip, computer models seem well-suited to investigate their failure mechanisms.

Most material failure phenoma involve a variety of processes occuring on a wide range of time and length scales and are, in general, poorly understood. Because of the complexity of the problem, mathematical models of fracture are usually limited to the propagation of a single crack tip in a homogeneous material. However, this simplification is far from satisfactory for real materials which either contain impurities or are composite in nature. In recent years, computer simulation has provided a promising approach to the understanding of facture behaviours, especially in inhomogeneous materials.

The aims of this project are to develop a static model of rubber-toughened polymers and to carry out computer simulations, based on this model, in order to provide some understanding of the fracture growth and toughening mechanisms in composite materials.

The results shown by this model have exhibited consistency with experimental studies and have provided new insight on rubber-toughening mechanisms occuring in the studied materials.

This work has been carried out in collaboration with ICI Wilton.

1.2 Overview of thesis

The work presented in this thesis is articulated around three main section :

- A review of relevant research work which has been published.
- A description of the numerical model that we have studied.
- A presentation of the various results obtained from model-based simulations.

1.2.1 Literature survey

The review of the literature falls in two chapters.

In chapter 2, we survey the research literature related to the materials. We focus on the studies which present experimental work concerning fracture in rubber-modified brittle polymers, and on related analytical modelling of their toughening mechanisms.

In chapter 3, we review the current techniques used in the computer modelling of brittle material's fracture in general and, more specifically, on that of rubber-toughened polymers.

1.2.2 The model

The static model studied in this work is described in chapter 4. Its lattice structure, stochastic nature and fracture mechanics are presented.

The computer implementation of this model requires the use of numerical methods to solve a large set of linear equations. In chapter 5, we present the different numerical methods which have been tested, and we detail that which has been found the most efficient in our case (*Conjugate Gradient*).

1.2.3 The results

The results presented in this thesis fall in three categories : the damage results, the stress results and the visual results.

Chapter 6 gathers all the damage-related results from the various simulations performed. We present and discuss damage and crack complexity data. We also study the influence of rubber concentration and material parameters on the damage.

Chapter 7 presents the stress-related results. These results are then discussed in order to shed light on the damage and crack development.

In chapter 8, we focus on the visual aspect of the results. This concerns the pictorial representation of damage and stress in various 2D and 3D systems.

The last chapter draws conclusions and makes overall comments on the work presented in this thesis. Some further improvements of the model are discussed.

Chapter 2

Literature Survey : Materials

2.1 Introduction

Unmodified glassy polymers are very brittle and exhibit poor resistance to crack propagation. Their fracture properties can be greatly improved with the addition of rubber particles to the polymeric matrix [1]. Such two-component polymers are indeed experimentally found to be more impact resistant than the unmodified ones. In pure glassy polymers, the energy dissipating mechanisms occur at small-scale levels, crazing and shear yielding take place at the vicinity of the crack tip which is only a small volume fraction of the loaded sample. The introduction of a dispersed rubbery second phase (usually spherical rubber particles) allows the energy absorbing region to be extended to practically the whole of the material's bulk and to delocalise the toughening mechanisms from the crack tip to the numerous particles sites.

The toughening mechanisms observed in these modified polymers and reviewed in the literature are essentially the *crazing* and the *shear yielding*, often related to the *particle cavitation*. The contribution of each of them in the overall toughness of the material is still a subject of discussion and its evaluation seems to be a testing- and material- dependent problem.

2.2 Toughening mechanisms

2.2.1 Crazing

From optical microcopy studies on High Impact Polystyrene (HIPS), Bucknall and Smith [2] have concluded that the function of the rubber particles is to initiate multiple craze growth in the polystyrene matrix. Subsequent studies have examined thin sections of various rubber-toughened polymers by transmission electron microscopy, using staining methods to increase contrast [6], and such work has clearly confirmed that crazes frequently initiate from rubber particles. Typical micrographs presented in Fig 2.1[4] for PS blends, and in Fig 2.2 for rubber-toughened PMMA, illustrate this crazing mechanism.

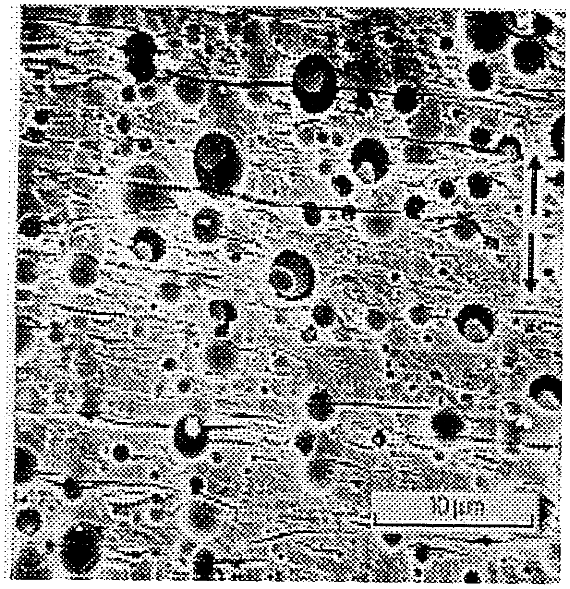

Figure 2.1: Micrograph of microtomed section of PS/ldPE blend (from [4]).

Bucknall *et al* [2] have proposed that the rubber particles have two separate but equally important functions. Firstly, under an applied stress, crazes are initiated

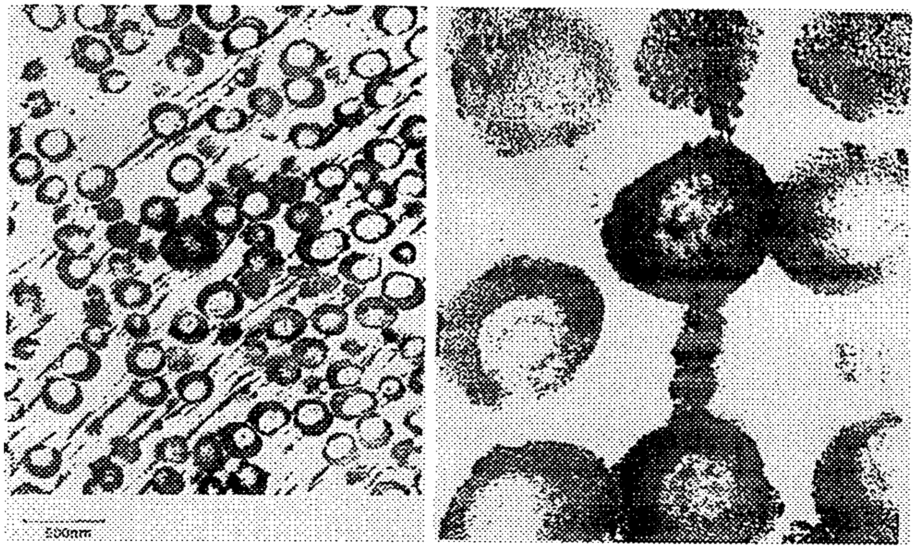

Figure 2.2: Micrographs of section of PMMA modified with core-shell rubber particles at different magnifications (courtesy of Dr. R. Ettelaie, ICI Wilton).

at points of maximum stress concentrations, which are usually near the equator of the rubber particules. The crazes then grow approximately normal to the direction of these maximum internal stresses, although deviations may occur because of interactions between the particles' stress fields. Secondly, the rubber particles are craze terminators, preventing the growth of very large crazes. Poor termination means that large crazes are produced which could act as sites for premature crack initiation and growth. Thus, the result is that a large number of small crazes are generated, in contrast with a small number of large crazes formed in the same polymer in the absence of rubber particles. The multiple crazing that occurs throughout a comparatively large volume of rubber-modified material explains the high energy absorption in fracture tests and the extensive stress whitening which accompanies deformation and failure.

In an impact study performed on blends of propylene-ethylene block copolymers (PEB) [5], the observation of the fracture behaviour has revealed a brittle-ductile transition occuring at a certain rubber concentration (16 wt %) The authors have examined the microdeformation behaviour of the tested samples and found that in the brittle region with low rubber content the deformation mode was crazing and voiding. In the ductile region with higher rubber content, crazing still takes place in the early stage of deformation and contributes to energy dissipation, then, as the applied impact energy is increased, both crazing and shear yielding occur at the same time. Therefore, in the ductile region, the microdeformation mode is found to change from crazing to shear yielding during the deformation.

2.2.2 Shear yielding and internal cavitation

When a polymer undergoes plastic deformation under an applied stress, it is said to yield. Shear deformation consists of a change of shape without significant change of volume. In tough single-phase polymers shear yielding accompanying the fracture process is a major mechanism for energy absorption, and this mechanism can be greatly enhanced in many brittle polymers by the presence of a rubbery second particulate phase [1]. Studies [8] on certain polymeric materials revealed that in uniaxial tensile tests, shear yield deformations occurred and that the polymer matrix had undergone localised plastic deformation around *virtually every* rubber particle.

To investigate these local shear yielding mechanisms, the stress field around a particle has been studied. For the simple case of an isolated elastic spherical particle embedded in a matrix, subjected to an applied uniaxial tensile stress, it has been demonstrated that the stresses are indeed maximal at the equator [9]. Furthermore, finite-element stress analyses have been performed [10] on systems with high rubber loadings. Determination of stress concentrations around the rubber particles indicates that in such cases the maximum stress concentration at the particle's equator may be appreciably higher than for the isolated case. This increase is thought to be primarily due to the interaction of the stress field of neighbouring particles. The rubber particles act, therefore, as stress concentration sites which induce localised plastic deformations, or micro-shear yieldings.

Particle cavitation

The effects on the stress distribution of the volume fraction of rubbery phase and the elastic properties (such as Young's modulus and the Poisson's ratio) have been investigated using finite element simulations in various studies [12, 13]. In these studies the shear yielding process is associated with another toughening mechanism : internal cavitation or interfacial debonding of the rubber particles. This is based on the existence of hydrostatic pressure that the deformed matrix creates within the rubbery phase. This in turn induces triaxial constraints in the surrounding matrix. The actual role of cavitation is still controversial and recent investigations on rubber toughened polymers have attempted to determine whether this mechanism is of significant importance for the overall material toughening. Various questions arise : is particle cavitation a major energy consuming phenomenon ? What promotes cavitation ? Is particle size and distribution of any importance ? How does cavitation influence shear yielding ? How do the rubber properties affect cavitation ? What is the relative importance of the other toughening mechanisms compared to cavitation-yielding ?

In a study performed on rubber-toughened epoxies, Bagheri and Pearson [14] performed comparative examinations of epoxies modified by conventionnal rubber inclusions on one hand, and by hollow plastic particles on the other hand. They showed that the use of these two different modifiers (rubber particles or micro-voids) toughened the material in the same manner and they further concluded that whilst the cavition mechanism does not contribute directly to toughness it does play a role in the formation of shear bands.

The hypothesis of important shear yielding around and between the rubber particles being promoted by their cavition is widely exposed in different experimental [14–17] or numerical works. For rubber-toughened epoxies, Yee and Pearson [18] and Kinloch and co-workers [19, 20, 22] suggested that the deformation processes are : (1) localised cavitation in the rubber followed by, (2) plastic yielding in the epoxy matrix. They further hypothesised that the relief of the triaxial tensile constraint by rubber cavitation is a very important step in toughening. Direct experimental evidence of this constraint relief effect due to rubber cavitation was given by [23]. They concluded that the success of the rubber used as a toughening agent for epoxies is closely related to its ability to cavitate. Cavitation allows local constraint relief; consequently, the surrounding matrix can undergo more plastic deformation and absorb more plastic energy. The same conclusions have been drawn in [24] for rubber-toughened polyamide-6 (PA-6), the particle cavitation relieves the plastic constraint and lowers the mean stress so that the cracking process is postponed and additional plastic deformation can occur, resulting in higher impact toughness.

Rubber cavitation as a precursor to shear yielding is widely exposed in the literature but it was first observed in HIPS [25] and real-time X-ray measurements on this material have shown that rubber cavitation actually precedes crazing of the matix under tensile impact conditions [26].

Cavitation criteria

Further numerical investigations have been performed to better understand the relationship between internal cavitation and shear yielding. In [21], finite element analyses have been carried out in order to determine the sequence of initiation of these two toughening mechanisms in epoxy matrices. The results show the importance of the rubber's material properties, in particular its Poisson's ratio. There is a critical value of the Poisson's ratio above which the initiation of internal cavitation occurs before localised shear yielding of the matrix. These conclusions tend to refute the previous hypothesis according to which cavitation would always be a promoter of shear yielding.

In this work, the criterion for cavitation used is a very simple one, based on hydrostatic pressure exceeding a critical value within the rubber particle ($P_y > 5E_r/6$, where P_y is the hydrostatic pressure and E_r the rubber's Young's modulus). A more complex energy criterion has been evaluated in [28], where cavitation is approached as an energy balance between the strain energy relieved by cavitation and the surface energy associated with the generation of a new surface. This criterion is given by the following expression :

$$U_{strain} + U_{surface} < 0$$

where U_{strain} is the elastic strain energy stored in the rubber particle and $U_{surface}$ is the surface energy associated with the void creation. The authors develop this equation to obtain the following criteria for rubber cavitation :

$$-\frac{\pi}{12} K_r \Delta^2 d_0^3 + \Gamma \pi \Delta^{2/3} d_0^2 < 0$$

where K_r is the rubber bulk modulus, Δ the volume strain, d_0 the particle diameter, and Γ is the surface energy per unit area for the rubber.

It appears from this expresssion that there exists a critical particle size required for cavitation ($d_0 = 12\Gamma / K_r \Delta^{4/3}$). Very small particles, then, are not able to cavitate, since their strain energy never reaches the cavitation energy barrier.

Another concept, related to that of the critical particle size, is the critical inter-particle distance [29]. The average inter-particle distance (IPD) is related to the particle size (d_0) and the rubber volume concentration (Φ_r) as follows :

$$IPD = d_0 \left(\left(\frac{\pi}{6\Phi_r} \right)^{1/3} - 1 \right) \tag{2.1}$$

This distance, also called the matrix ligament thickness τ, corresponds to the surface-to-surface inter-particle distance. In [30], this parameter is presented as responsible for the sharp brittle-tough transition shown by rubber-modified polymers with pseudo-ductile matrix [29]. This transition is found to occur at a single critical

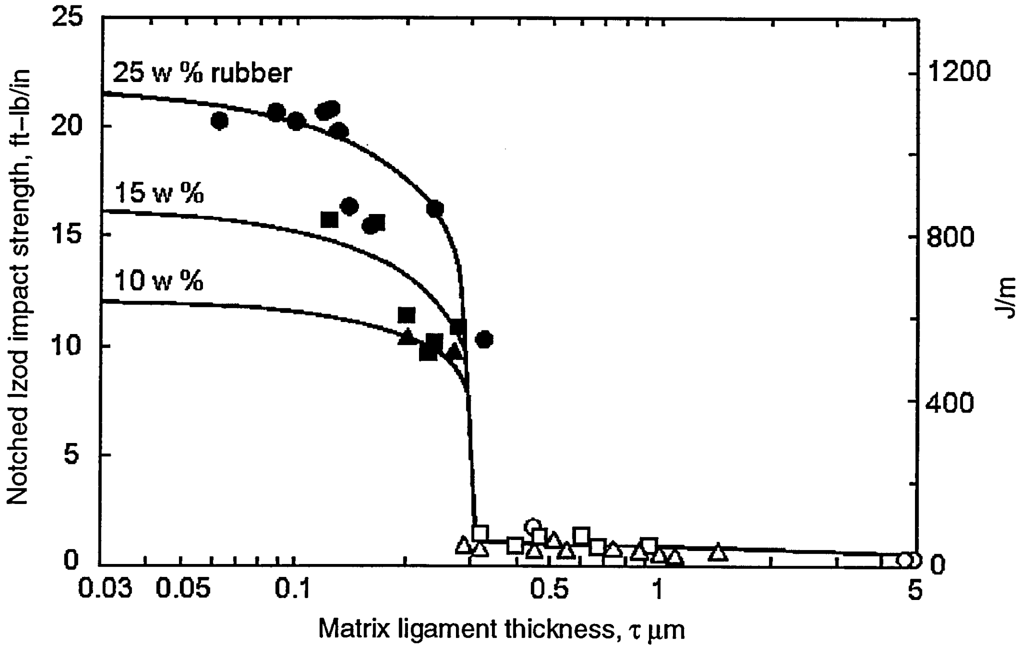

Figure 2.3: Notched Izod impact strength vs. matrix ligament thickness for nylon-66/rubber blends wt% rubber as a function of the rubber particle size (from [29])

value τ_c which is independent of the rubber concentration and the particle size. A simple condition for this kind of material is :

$$\tau < \tau_c$$

Fig 2.3 shows the notched Izod impact toughness for nylon-66/rubber blends and the sharp brittle-tough transition for a critical inter-particle distance $\tau_c \sim 0.3\mu m$. According to [30], the explanation of this critical phenomenon is that when the rubber particles cavitate during an impact fracture, if the matrix ligament is thinner than τ_c, they would yield locally and when all of them are interconnected, the matrix yielding would propagate throughout the entire deformation zone and the blend would be tough. On the other hand, when the rubber particles are too far apart this yielding propagation does not occur and the thick matrix ligaments would fail in a brittle manner. As pointed out in [31] and [38], the percolation concept is the physical explanation behind this inter-particle distance.

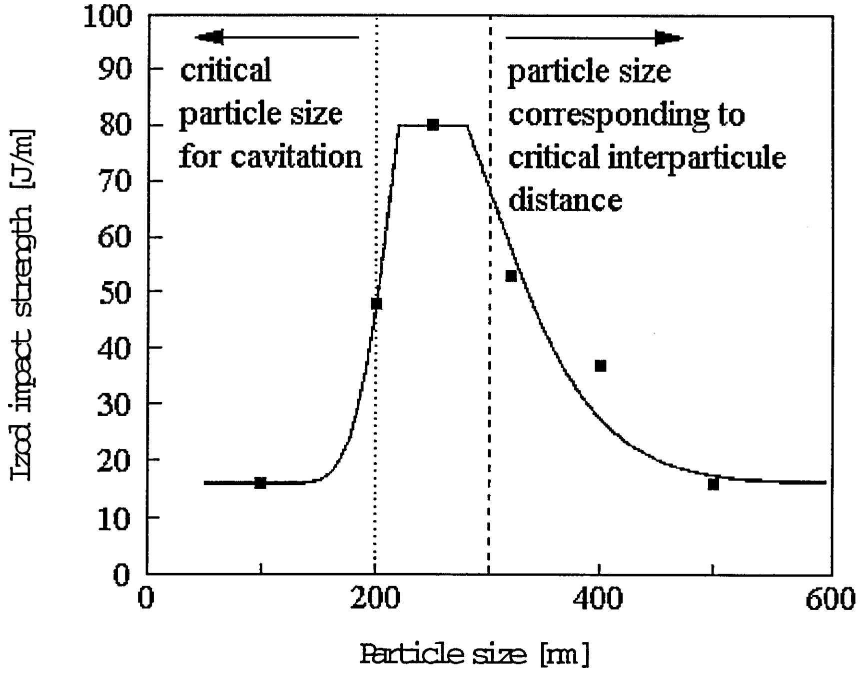

Figure 2.4: Notched Izod impact strength of rubber-modifier PMMA with 20 wt% rubber as a function of the rubber particle size (from [31] and [28])

In [28], the authors have reconsidered results presented in other works in the light of the critical particle size and critical inter-particle distance concept. In [31], the effect of the rubber particle size on the notched Izod impact toughness of modified PMMA has been studied (*cf* Fig 2.4). The sharp increase in toughness occuring at ~ 200nm is then interpretated as a result of the particle reaching the critical particle size for cavitation (cavitation relieving the hydrostatic tension in the matrix, then inducing big energy dissipation through shear yielding). Below this limit, the toughness efficiency of the rubber seems to be negligible. The maximum toughness, which is reached for a particle size of ~ 250nm, is related to the critical inter-particle distance concept. This approach presupposes that the rubber particles cavitate, *ie* the particle diameter being above the critical particle size and that the toughness decreases sharply for rubber particles of greater diameter due to increase in IPD. Fig 2.4 confirms this critical inter-particle distance interpretation.

In parallel to the above work, Lazzeri and Bucknall [32, 33] developed, a similar

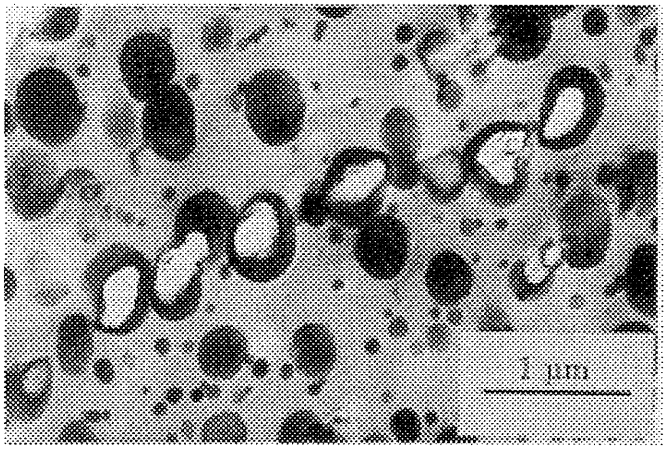

Figure 2.5: Dilatational band in rubber-toughened nylon-6 (from [33])

model again based on a energy balance criterion for cavitation of triaxially stressed rubber particles. Based on experimental work supporting the view that particle cavitation precedes large-scale shear yielding of the polymer matrix [34], specifically in the form of cavited shear bands (or dilatational bands) [35, 36], they proposed a predictive model for dilatational band formation associated with particle cavitation. In a later paper Bucknall [37] further developed this cavitational model in order to take into account the contribution of the energy stored in the matrix and subsequently released as voids expand. A typical micrograph of these dilatational bands is presented in Fig 2.5 [33].

Shear yielding versus Crazing

The main energy dissipating and hence toughening mechanisms in unmodified glassy polymers are known to be (1) crazing and (2) shear yielding and they are concentrated at the vicinity of the crack tip. In intrinsically ductile or rubber modified polymers, by contrast, the deformations take place throughout the whole material. Recent work has been carried out to compare the contribution of each of those two mechanisms to the toughness of composite polymers. In [15], experimental comparisons in rubber modified polystyrenes have shown that the main source of plastic energy absorption is cavitation-induced microscopic shearing yielding. Furthermore, the authors concluded that increasing the rubber loading leads to a decrease in the crazing toughening component whereas the impact toughness increases. It is nevertheless worth noting that these tensile tests were performed at slow strain rate ($1.7 \times 10^{-4} s^{-1}$) which does not reproduce the impact dynamic conditions for which these materials (like HIPS) are engineered.

The nature of the tested materials should also be considered when drawing any conclusions about the toughening mechanisms' contribution. The glassy polymer matrices used for rubber modified materials fall in two main categories : thermoplastics and thermosets. Their different natures lead to different failure behaviours.

2.3 Materials

2.3.1 Thermoplastics

Fracture mechanisms in unmodified glassy thermoplastics, such as Poly(methyl methacrylate) PMMA, Polystyrene (PS), Polycarbonate (PC), etc., can be described in terms of linear elastic fracture mechanisms since their bulk deformation is approximately elastic [1], plastic deformation being concentrated around the crack tip only. The mechanisms involved in modified thermoplastics are more complex, the inclusion of a rubbery second phase inducing localised energy dissipating mechanisms. A mechanism thought to be of major importance in the toughening of these materials is crazing [1], but recent studies tend to contradict this idea.

Concerning rubber toughened PMMA (RT-PMMA) certain authors [39, 40] suggest that the blend mainly deforms via shear yielding and that crazing is actually of no importance at all [15].

Bucknall *et al.* [41] have also attempted to identify the toughening mechanisms in RT-PMMA. From creep experiments they concluded that the dominant deformation mechanism was shear yielding. However, strain rates involved in these creep tests were low ($2 \times 10^{-4} - 1 \times 10^{-2}$ sec^{-1}) which does not reproduce impact conditions.

In investigating the effect of the rubber volume fraction in RT-PMMA [42], the critical energy for crack initiation has been evaluated using a single specimen J-integral method. The resulting data exhibit a sharp increase of the toughness for a critical volume fraction around 30%. This result is correlated to the material's capacity to develop plasticity. This property being quantified by a work-hardening parameter K' which is defined as the slope of the stress-strain ($\sigma - \varepsilon$) curve measured in the earlier stage of the non-elastic deformation (preyield zone) for a given strain rate ($\dot{\varepsilon}$) :

$$K' = \left(\frac{\delta\sigma}{\delta\varepsilon}\right)_{\dot{\varepsilon}}$$

This parameter is related to the number of shear nuclei produced per unit of stress. It appears that the sharp material toughness increase corresponds to a comparable sudden drop of K', which indicates an enhanced tendency to shear nucleation. Here again it should be pointed out that the impact experiments were performed at very slow speed (100μm min^{-1}) and, therefore, the conclusions reported do not necessarily hold for real impact conditions.

This loading-rate dependence of the fracture behaviour of RT-PMMA was studied in [43, 44]. In this the authors investigated the fracture behaviour over a broad range of testing velocities (from 10^{-4} to $14ms^{-1}$) and for different rubber concentrations. In the view of a typical force-displacement diagram (*cf* Fig 2.6), the tested materials showed three successive crack growth transitions as the test speed was increased (*cf* Fig 2.7) :

- Transition 0 : from stable to partially stable
- Transition I : from unstable to fully unstable after F_{max}
- Transition II : beyond this point the crack growth is fully unstable and no

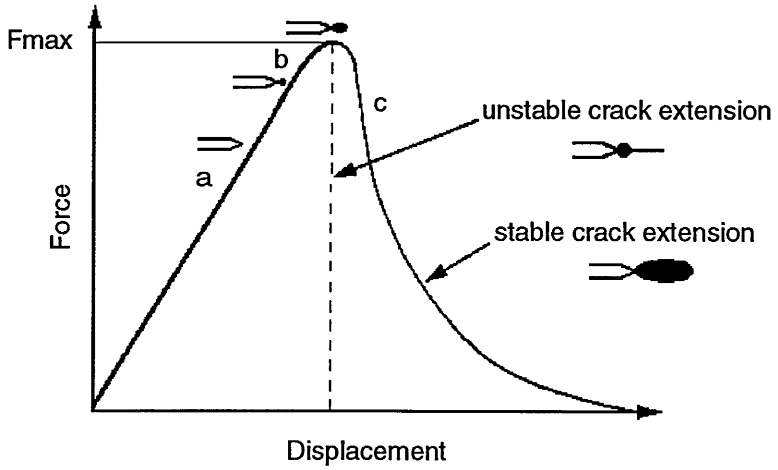

Figure 2.6: Typical force vs. displacement curve associated with growth of the damaged zone. Key : a, initial, linear regime; b, nonlinear regime; and c, the third regime, corresponding to crack extension. (from [44])

stress-whitening is visible.

These results were obtained with notched specimens. The stress-whitening of the material is associated with the instability of the crack propagation, this whitening disappearing for high impact speed where the crack progression is fully unstable. In these experiments, the whitened area of the fracture surface was associated with the plastic deformation the matrix undergoes in the region of the crack. In other words, *the fracture behaviour of the tested RT-PMMAs is found to change from ductile to brittle with the increase of the testing velocity.* The fracture behaviour is a fully time-dependent process, the plastic deformation phenomena need time to develop and propagate throughout the matrix in order to be effective. The observed transitions result from the material's progressive inability to exhibit large-scale plasticity.

However, large stress whitening is also seen in high impact (but non-notched) tests. At these high impacts, no plastic deformation is likely. Indeed experimental TEM results show that most of the stress whitening is due to extensive crazing [45]. As shown in [45, 46], notched and non-notched experiments, as well as different testing methods, provide very different conclusions. Notched experiments proceed

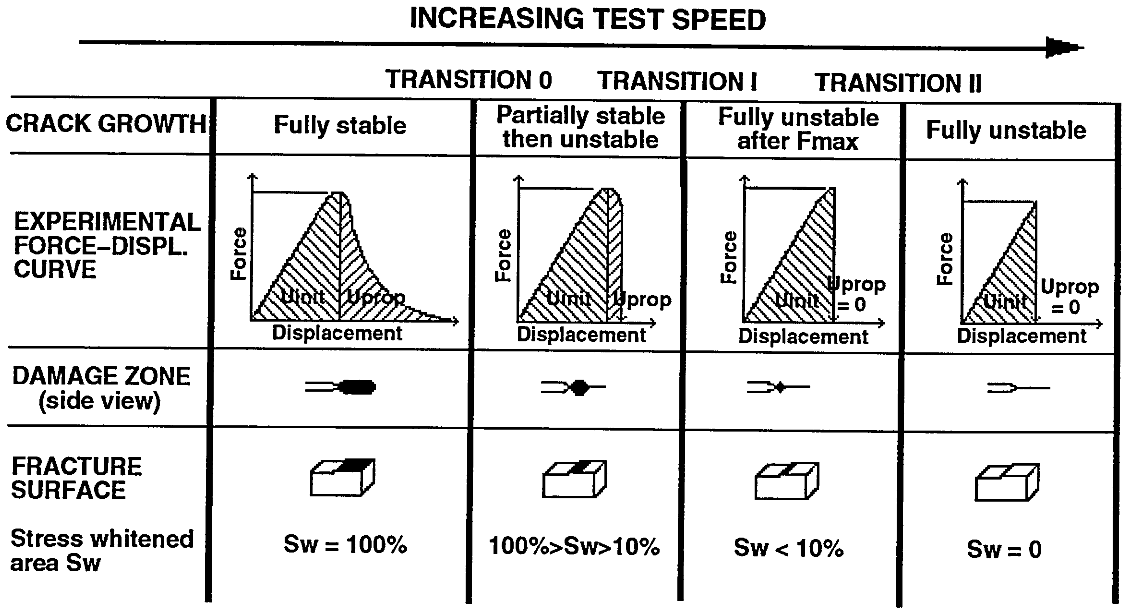

Figure 2.7: Transition and fracture behaviour of RT-PMMA over the range of testing speeds (from [44])

from pre-damaged situations and, therefore, by-pass the important crack nucleation mechanisms.

2.3.2 Thermosets

A lot of experimental studies have been carried out on rubber modified epoxies (thermoset polymers). In [48] the fracture energies of these kinds of materials have been determined over a large range of strain rates (including impact testing). Two forms of rubbery modifiers were used, liquid and solid. Both improved the material's toughness and the best results were obtained with a combination of these two modifiers. For all the compositions tested, modified materials showed the greatest toughness at slow strain rates and a systematic decrease in fracture energies with increasing strain rate. Post-failure SEM examination of the two rubbery phase modified specimens showed local shear yieding of the epoxy matrix induced by large particles ($2 - 4\mu m$). However, when the epoxy was modified with the solid rubber phase alone, the SEM examination did not exhibit specific localised yielding associated with the larger particles, but random shear yielding of the matrix occured anyway.

In another experimental study on rubber toughened epoxies [7] the crack growth behaviour in such materials has been examined over a wide range of temperatures and strain rates. Three main types of crack growth have been observed : (A) ductile stable, (B) brittle unstable and (C) brittle stable. The temperature dependence of the type of crack growth can be ascertained by a progressive change from a type (C) to a type (A) crack growth as test temperature is increased.

2.4 Experimental results

A collection of some of the experimental results regarding the rubber loading, inter-particle distance and particle size effects found in the literature are presented hereafter. They present the effects of various essential parameters on the blends' toughness, such as the ruuber concentration, the inter-particle distance, the particle size, the temperature, etc.

2.4.1 Rubber loading effects

As pointed at in [29], Eq. 2.1, which gives the critical inter-particle distance for the tough-brittle transition, can be rearranged in a form which brings out a critical rubber volume fraction Φ_c :

$$\Phi_c = \frac{\pi}{6}\left(1 + \frac{\tau_c}{d}\right)^{-3}$$

Fig 2.8 illustrates the rubber weight fraction effects on the toughness of nylon-66/rubber blends and the tough-brittle transition occuring at a critical rubber con-

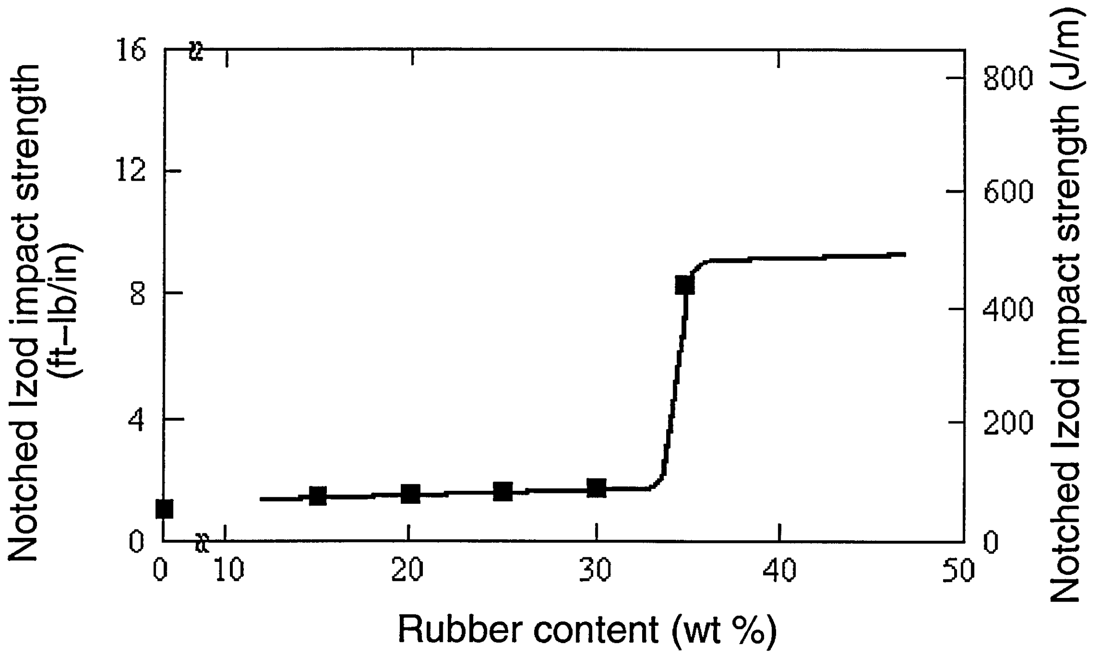

Figure 2.8: Rubber content effects on the notched Izod impact strength for nylon-66/rubber blends (from [29])

tent.

In [17], notched Izod impact tests have been performed on rubber-modified polyamides (PA66/EPDR). The results presented in Fig 2.9 clearly shows the brittle-tough transition at a critical rubber concentration.

In a work carried out on PMMA blends [40], the material toughness has been studied over the full range of rubber fraction. The results are presented in Fig 2.10 and shows again the tough-brittle transition and a toughening saturation effect as the rubber loading is increased further.

Another experimental evidence of the tough-brittle transition is given by Fig 2.11 from [5] for blends of propylene-ethylene block copolymer (PEB).

A clear trend of the rubber fraction effects on the blends' toughness can be drawn from these results. The rubber efficiency on the toughening appears to be unsignificant below a critical rubber concentration; above this critical value this efficiency

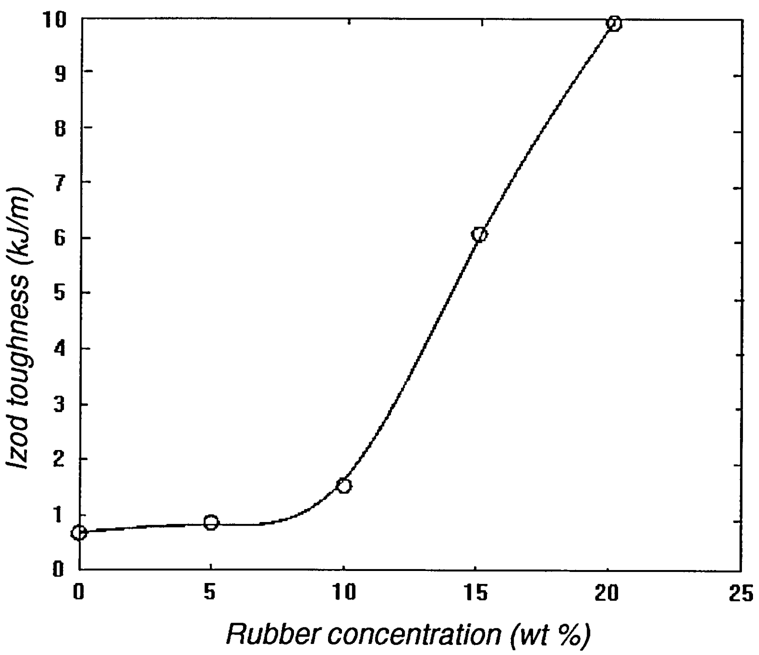

Figure 2.9: Rubber content effects on the notched Izod impact strength for PA66/EPDR blends (from [17])

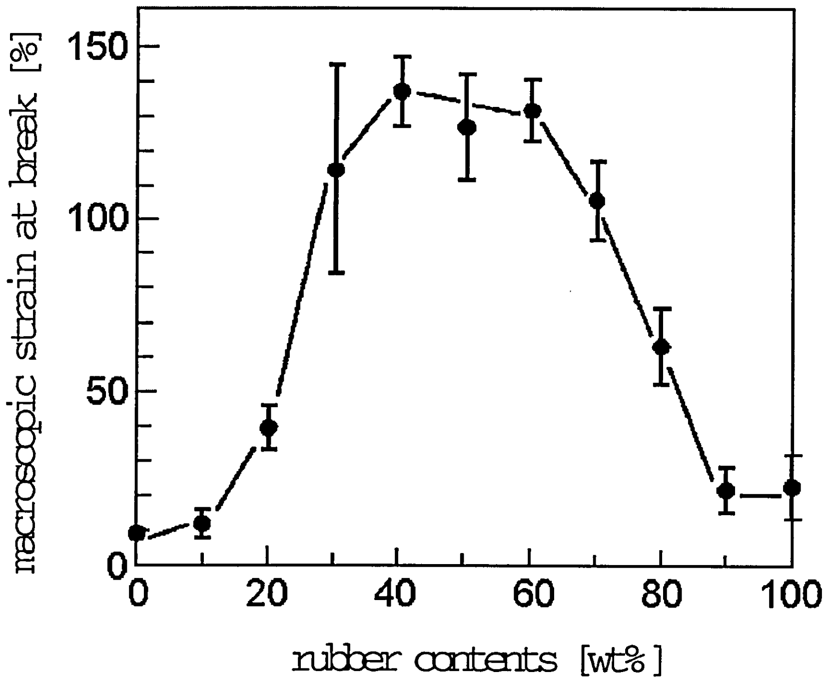

Figure 2.10: Strain at break vs. rubber contents for PMMA/epoxy blends (from [40])

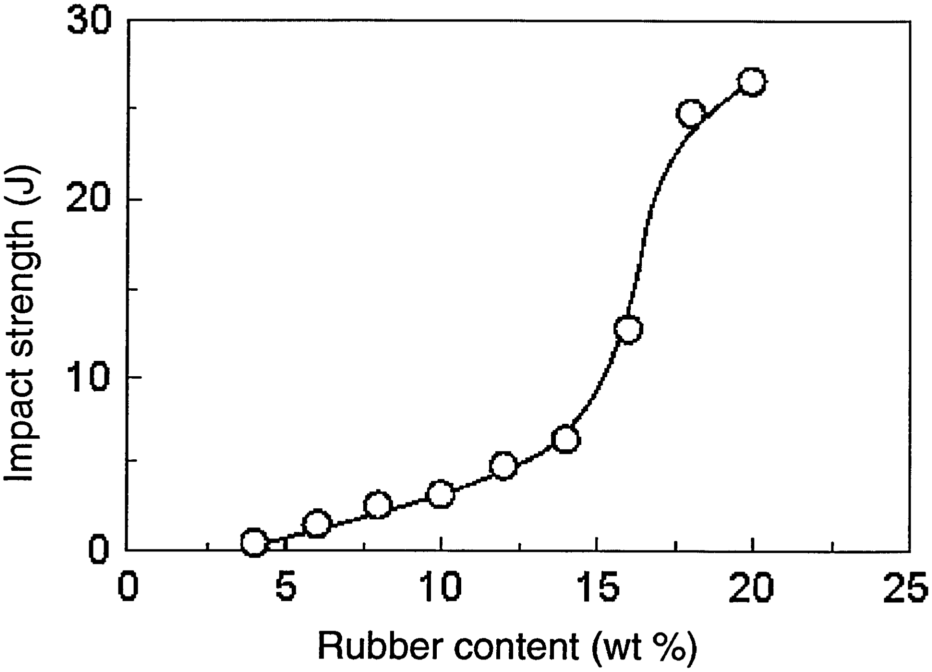

Figure 2.11: Impact strength at -20C vs. rubber content for PEB blends (from [5])

is highly improved up to a saturation point where the rubber toughening effects level out (this is clearly evident in Fig 2.8 and Fig 2.10) and for very high rubber loadings, the rubber toughening effects seems to decrease significantly.

2.4.2 Inter-particle distance effects

The inter-particle distance, or matrix ligament thickness τ, has been proved to be a major concept in the toughening of rubber-modified polymer. Several workers have presented results to back up the toughness dependency on this material parameter.

The first work to come up with significant experimental evidences of the toughening effects of the particle surface-to-surface distance is [29]. From these results shown early on in Fig 2.3 (*cf* section 2.2.2), one can see a sharp brittle-tough transition occuring at a critical value of the inter-particle distance τ_c. If $\tau < \tau_c$, then the blend's toughness is dependent on the rubber concentration. If $\tau > \tau_c$, then the rubber seems to be of no effect on the material's impact resistance.

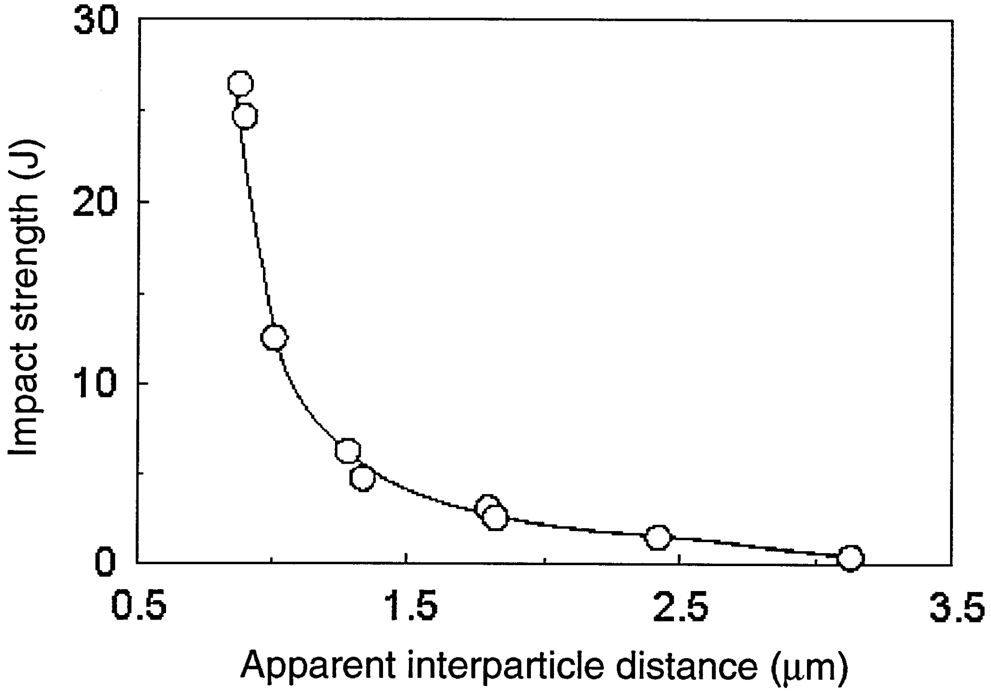

Figure 2.12: Impact strength at -20C vs. rubber content for PEB blends (from [5])

The influence of the inter-particle distance on the blend toughening is reported by other works. In [5], the toughness of propylene-ethylene block copolymer (PEB) blends is correlated with this material parameter to show the existence of a critical value τ_c below which the blends exhibit high impact resistance (*cf* Fig 2.12 from [5] for blends of propylene-ethylene block copolymer (PEB)).

However, this inter-particle distance theory does not give a clue as to why there is a saturation point when the rubber loading is increased above a certain limit (*cf* previous section).

2.4.3 Particle size effects

The particle size effects on the blends toughness have been reported in different works [17, 27–30]. In Fig 2.13 extracted from [29], the notched Izod impact strength of nylon/rubber blends is presented for different rubber fractions when the particle

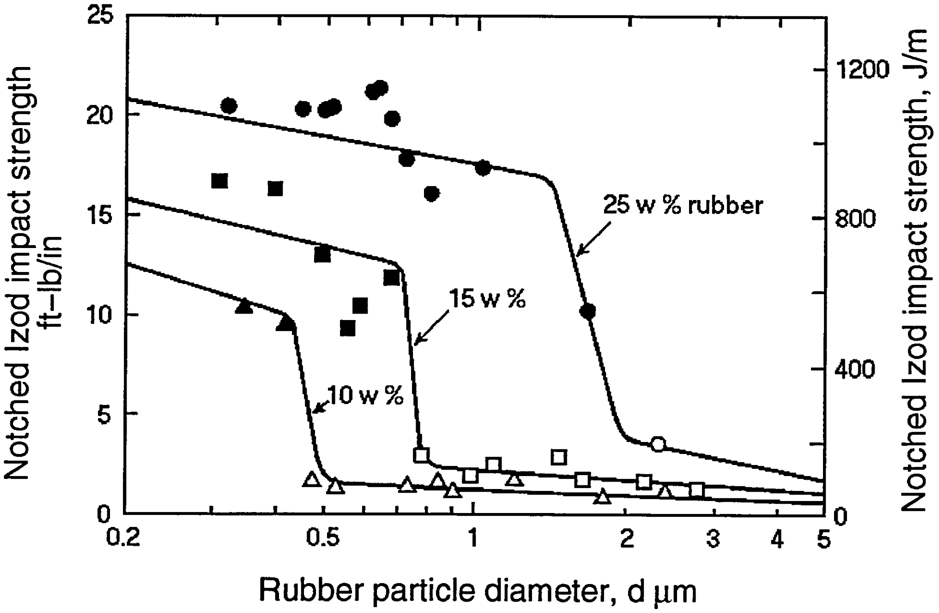

Figure 2.13: Notched Izod impact strength vs. number-average particle diameter d of nylon-66/rubber blends for different rubber fraction : $\triangle 10\%$, $\square 15\%$, $\bigcirc 25\%$. Solid symbols are for tough fracture, open symbols are for brittle fracture (from [29])

size d is changed. Two modes of fracture are observable. The blends break in a tough fashion when $d < d_c$, d_c being the tough-brittle critical particle size, $\sim 75\%$ of the impact energy is dissipated by the matrix yielding and $\sim 25\%$ by crazing. When $d > d_c$, the materials are found to break in a brittle manner.

The existence of a critical particle distance is brought forward by Fig 2.14 from [17] for polyamide/rubber blends.

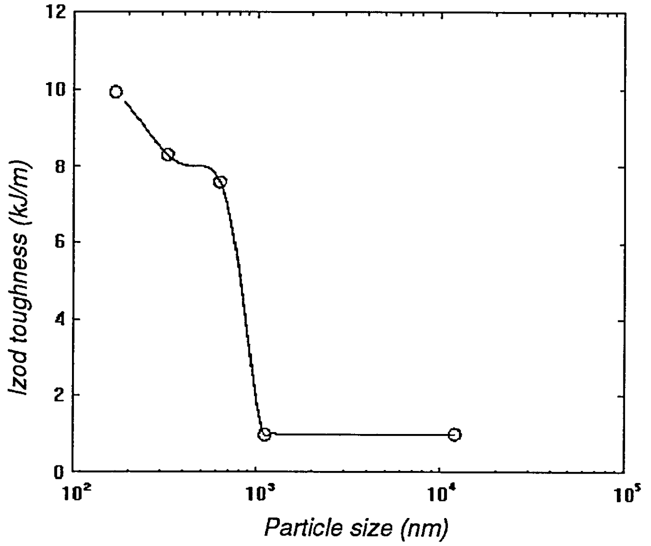

Figure 2.14: Effect of the particle size on Notched Izod toughness for polyamide/rubber blends at room temperature (from [29])

2.5 Conclusion

The various results of the different studies reviewed show the complexity of the crack behaviour of rubber toughened polymers. The results multi-dependence on the various test parameters on one hand, such as temperature, strain rate, not to mention the test method itself (*ie* notched Izod, non-notched Charpy, etc.) and the sample geometry, and, on the other hand, the material differences of the tested specimens (such as its thermoset/thermoplastic nature, the rubber phase concentration, particle size, etc.) suggests that the toughening mechanisms have multiple source and what can be concluded from one experiment can be significantly different to another. Nevertheless, among the different observed mechanisms, crazing, shear yielding, rubber particle cavitation/debonding, crack bridging, etc. the two former ones seem to have a major contribution in the material toughening. For thermoplastic matrices, under normal temperature conditions, crazing seems to be the dominant toughening factor for impact testing [45] whereas it appears to be of less importance for slow strain rate testing [15]. For thermoset matrices, on the other hand, the evidences of shear yielding as a principal toughening mechanisms are numerous [14, 16, 17, 34].

As seen, the various toughening mechanisms occuring in rubber-modified polymers have still to be fully understood and their relative importance in the overall toughening of the material is still a matter of discussion and controversy.

Chapter 3

Literature Survey : Numerical models

3.1 Introduction

Most material failure and deformation phenomena involve a variety of processes occuring on a wide range of time and length scales. Many of these are nonlinear processes occuring under nonequilibrium conditions; as such they are, in general, still quite poorly understood. Considerable effort has been devoted to the propagation of a single crack tip in a homogeneous medium, but real materials are inhomogeneous, crack geometries are often complex, and crack-crack interactions are important. Understanding of crack nucleation and propagation in homogeneous materials has improved recently with the development of simple algorithms to simulate these processes under static loading. A lot of work has been performed using lattice-type or mesh-type models. The success of such models arises due to their relative simplicity and to the ease with which they can be implementated. They are based on a discretisation of continuum equations; the medium being reduced to a set of points embedded into a grid. Simple mechanical laws, such as force equilibrium, are considered at the local level so that their implementation involves, for each site, only a few neighbours. Among those models, the *finite element* method and the *network* models are the most popular, but some studies have been carried out with other lattice-type models, such as the *boundary element* method, and with *energetic* models.

A interesting advantage of the lattice models is that they allow very naturally the introduction of disorder or heterogeneity (this is not easy in FEM).

3.2 Finite element method

In the finite element method (FEM), the stress singularities at the crack tip are captured using mesh elements. When crack propagation is modelled, the mesh has to be continuously modified and adapted as the fracture geometry changes. This kind of mesh redefining at every step makes the FEM inefficient and very computationally expensive. Even though this method is not well-adapted to crack growth simulations, it has been used successfully to study local toughening mechanisms (such as cavitation or band shearing [19, 20]) and stress field evolution [12] in rubber-modified polymers.

A good example of where the FEM have been applied with success to fracture mechanisms of the rubber-modified polymers is the study of systems limited to one single, or two, rubber particles. The first FEM attempt to model numerically the rubber-modified polymers was reported by Broutman and Panizza [10]. Their model assumed that the material was an assembly of axisymmetric cells, each containing a single rubber particle as illustrated in Fig 3.1. A typical FEM meshing employed for this axisymmetric model is presentend in Fig 3.2. This principle was later extended to a three-dimensional model by Argarwal and Broutman [11], but because of the three-dimensional complexity of the analysis and the computational cost, the

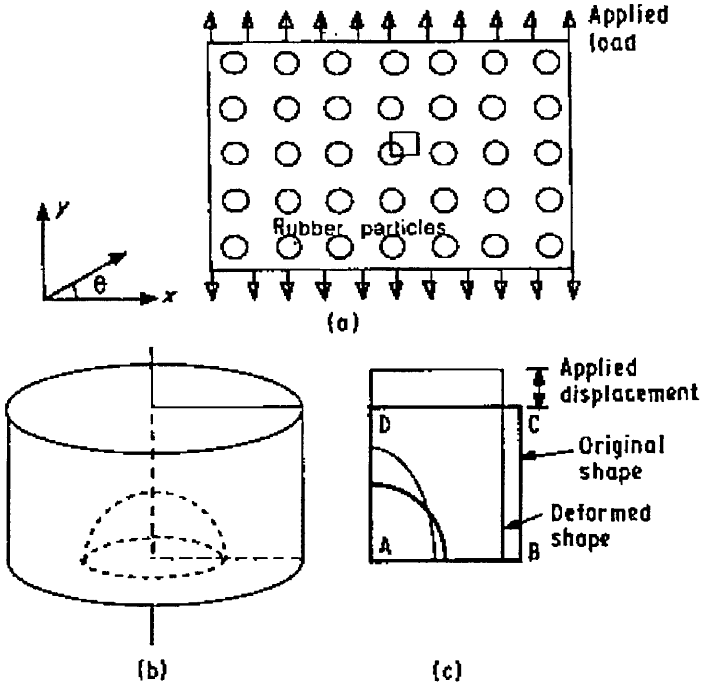

Figure 3.1: The axisymmetric model : (a) the packing of the particles; (b) the selected cylinder; (c) the boundary conditions. (from [19])

authors concluded that the former axisymmetric model could be used without a significant loss of accuracy. The study of the axisymmetric model and its FEM implementation revealed that the maximum direct and shear stresses were located at the equator of the particle, indicating that this region would be prone to initiating matrix yielding. This model also showed a stress concentration increase as the particle volume fraction was increased.

Huang and Kinloch [19, 20] have developed a two-dimensional FEM model which illustrates how FEM solutions can be used to simulate and analyse the stress fields and deformation processes around interacting single rubber particles or alternatively, around neighbouring circular voids. Their model extended the axisymmetric model. Indeed, as they pointed out, the latter was essentially elastic in nature and therefore could not correctly exhibit initiation and propagation of localised matrix shear yielding. Their model introduced the elastic-plastic behaviour of the matrix in the form of a piecewise stress-strain curve (*cf* Fig 3.3) which was derived from exper-

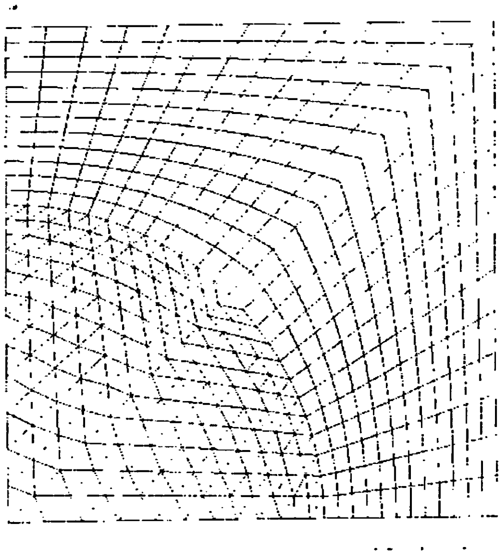

Figure 3.2: A typical finite element mesh employed for axisymmetric model. (from [19])

imental data for unmodified epoxy. In order to model the localised matrix shear yielding (shear-banding) process, a new two-dimensional meshing was adopted to better expose the inter-particle regions (*cf* Fig 3.4).

Huang and Kinloch also used their model to determine the sequence of initiation of the toughening micromechanisms in rubber-toughened epoxies [21]. The aim of their study was to verify the assumption that particle cavitation was a precursor to matrix shear yielding. Therefore, they implemented in their FEM simulation a simple criterion for particle cavitation, which is assumed to occur when the hydrostatic stress inside the particle reaches a threshold value. On the other hand, they used the Von Mises criterion for the shear yielding of the epoxy matrix, assumed to happen when the maximum Von Mises stress in the matrix, which occurs at the particle/matrix interface, attains the uniaxial yield stress of the matrix. The von Mises criterion may be stated as

$$(\sigma_1 - \sigma_2)^2 + (\sigma_2 - \sigma_3)^2 + (\sigma_3 - \sigma_1)^2 = 6\tau_y^2$$

where σ_1, σ_2 and σ_3 are the principal stresses of the applied stress tensor and the

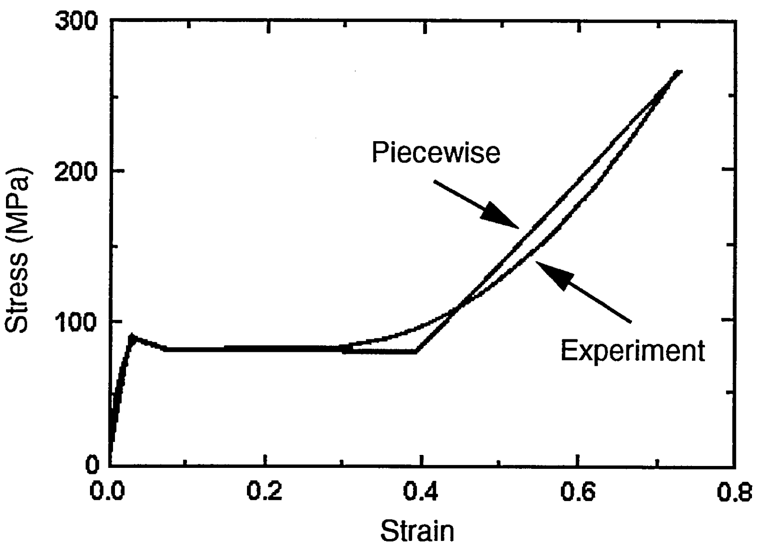

Figure 3.3: The experimental and the simplified piecewise tensile stress versus strain curve for the expoxy matrix. (from [19])

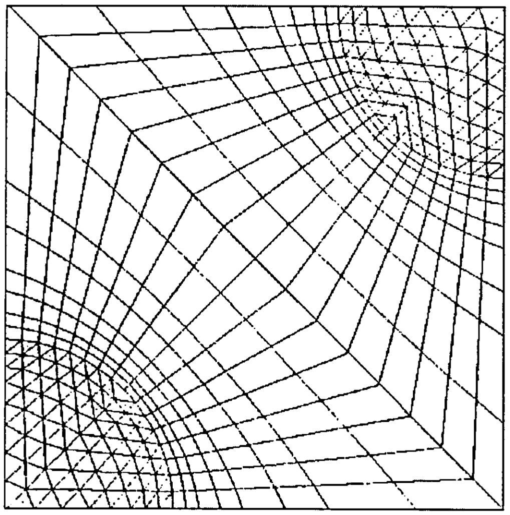

Figure 3.4: A typical finite element inter-particle region mesh employed in [19]

constant τ_y is the shear stress for flow in pure shear.

This FEM-based model allowed them to conclude that the sequence of initiation between those two toughening mechanisms (cavitation/yielding) was strongly dependent on the properties of the rubber particles, and, in particular their Poisson's ratio.

Guild and Kinloch [22, 49] have presented an example of the use of FEM to model the macroscopic properties of two-component materials from the local modelling of rubber particles embedded in a polymeric matrix. Their model is based on the idea of analysing a representative cell of the material. The representative cell concept assumes that the macroscopic material properties can be determined from averaging the effects of all interacting particles. The material is then divided into cells containing a single rubber particle surrounded by a polymeric matrix. These representative cells are the Voroni cells, a given cell is centered upon a single rubber particle and its domain covers the region of the matrix region closer to this particle than to any other one. For a random particle distribution, these cells are spherical and their size can be calculated [50]. The material is then summarized as a collection of spherical cells and its properties can be obtained by summing all the cells' individual contributions. The authors used this representative cell concept in a FEM formulation where a single cell, which describes the overall volume fraction, was meshed as illustrated in Fig 3.5. This model allowed them to study the effects of the rubber properties on the stress distributions.

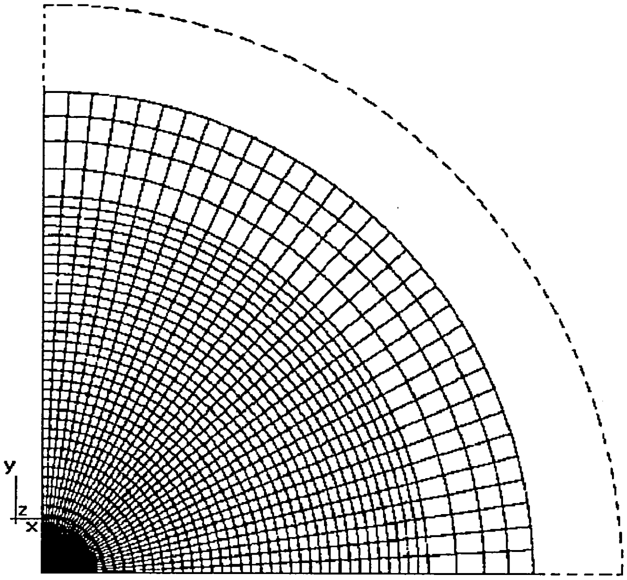

Figure 3.5: Finite-element grid of a representative cell (from [22])

3.3 Network models

3.3.1 Introduction

In this approach, the material is modelled by a two-dimensional or three-dimensional network of mechanical elements, such as bonds, springs or beams, each with its own set of specified mechanical properties. These one-dimensional elements represent the system on a mesoscopic scale and are characterised by a constitutive law which in the simplest case is just a linear stress-strain relation up to a breaking threshold value. A static, usually uniaxial, tensile stress is applied to the network. Under this circumstance, the displacement field is calculated at each equilibrium step, usually through the solution of a large set of linear equations. When the system has been equilibrated and stresses on the elements have been determined, the mechanical element to be broken is selected according to a breaking rule and is removed from the network. The equilibration and element breaking processes are then repeated until some completion criterion (such as debonding of two parts of the lattice) is satisfied. A more detailed discussion of this procedure will be given later.

3.3.2 Bond breaking criteria

In many models, the choice for the bond breaking criterion derives from a kinetic approach to the fracture process that occurs on a molecular scale. In this approach, the basic rupture event (bond breakage) is considered to be a stochastic phenomenon governed by a failure rate depending on the local stress. The underlying principle is that bond failure is a chemical process and, therefore, the Arrhenius model, which expresses the rate of chemical reactions, can be extended to material breakdown problems. Eyring's reaction-rate theory is an extension of the Arrhenius model, in which the lattice bonds are viewed as *coupled oscillators in a state of thermal vibration* [58]. Bond failure is then treated as a random process activated by the random thermal fluctuations. The basic principle is that in order to change its status, a molecule must pass over an energy barrier (also called an activation energy). Similar principles are applied to co-operative motion of many molecules making up a single bond. The rate of bond failure can then be written as (*cf* [53]) :

$$R = b\,(T)\,e^{-E_a/k_bT}$$

where E_a is the activation energy, k_b is the Boltzmann's constant, T is the temperature, and $b(T)$ is a weakly temperature-dependent preexponential factor.

In a stress free state, a single bond (set of molecules) is unlikely to change its status, its thermal energy being too small to exceed the energy barrier. When a stress is applied, the bond's energy is shifted up by an amount corresponding to the mechanical energy $E\,(f)$ gained by the action of the applied force f (in an elastic bond model, this energy is the stress-induced elastic energy stored in the bond). The energy change required to cross the barrier is therefore reduced by this amount, and the bond's probability to change status is increased. The failure rate under

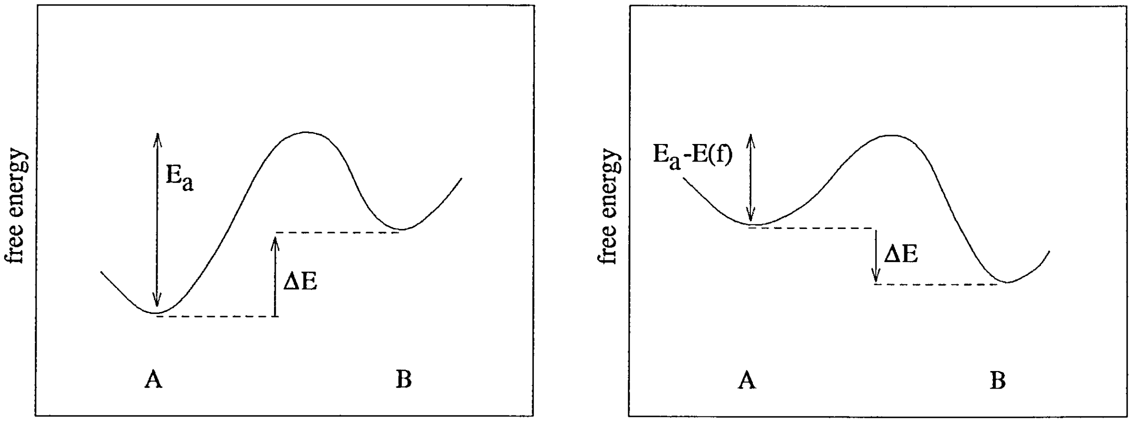

Figure 3.6: Schematic representation of the free energy change from stress-free (left) to stressed (right) situations. State A represents the unbroken bond and state B the broken bond

stress conditions can then be expressed as [53]:

$$R = b\,(T, f)\, e^{-(E_a - E(f))/k_b T} \tag{3.1}$$

This situation is illustrated in Fig 3.6 for the unstressed and stressed conditions. In the unstressed condition, the system is stable since bond breaking can only occur through an increase in free energy, ΔE. At a sufficiently high level of applied stress, ΔE becomes negative and bond rupture becomes more likely.

For a simple harmonic potential the elastic energy stored in a distorted bond is :

$$E\,(f) = \frac{1}{2} k \Delta l^2 = \frac{f^2}{2k} \tag{3.2}$$

where k is the bond's elastic coefficient and Δl is the bond's elongation.

As pointed out in [53], a considerable amount of experimental data for polymers supports the idea that in a stressed situation, the activation energy E_a is reduced by an amount which is proportional to the applied local stress σ [1]. Under these circumstances, the bond failure rate can be formulated as [1,53] :

$$R = \nu_0 e^{-(E_a - v^* \sigma)/k_b T} \tag{3.3}$$

where ν_0 is a thermal vibration frequency and v^* is an activation volume. In the case of a bond network, v^* can be reinterpretated as an activation length l^* and σ replaced by the force f.

As an extension of this reaction-rate theory, the average time needed for the failure of a bond, τ, can be expressed from Eq 3.3 in the following form [54,55] :

$$\tau = \left(\sum_i R_i\right)^{-1} = \left(\sum_i e^{-(E_a - E(f_i))/k_b T}\right)^{-1} \tag{3.4}$$

where R_i is the failure rate of the i^{th} bond under a force f_i, and the index i runs over all the unbroken bonds.

Another statistical approach to bond failure, derived from fracture mechanics, is reported by both Harlow and Phoenix [51] and Leath and Duxbury [52]. They considered the fracture of fibre-bundle systems. In the fibre-bundle model the local failure thresholds are drawn from continuous distributions, such as the Weibull and uniform distributions. The Weibull statistical method is a fracture mechanics tool used to describe the scatter in failure stress exhibited by brittle materials. The statistical aspect of material strength comes from the fact that the strength of a sample is determined by weak pre-existing defects in that sample which cause fracture initiation and propagation at relatively low applied stresses. Since the defects vary in size and weakness from one sample to the other, the strengths measured are therefore identically distributed. According to Weibull [56], the material breakdown stress distribution $f_w(\sigma)$ is assumed to be of the following cumulative form :

$$\begin{aligned} F(\sigma) &= \int_0^{\sigma} f_w(\sigma')\, d\sigma' \\ &= 1 - e^{-\left(\frac{\sigma}{\sigma_0}\right)^m} \end{aligned}$$

where $F(\sigma)$ is the probability of mechanical failure in a material upon application of an external stress σ, σ_0 is a normalising constant and m is the material-dependent Weibull modulus. The value of m increases with decreasing scatter. This distribution, which concerns the failure stress of the overall material, is then assumed to also apply on a local level to each bond, determining the bond-failure probability under stressed conditions.

In another probabilistic approach, the uniform distribution, the bond-failure probabilities are expressed by the following probability density :

$$\begin{aligned} f_u(\sigma) &= \frac{1}{W} \quad \text{if } 0 \leq \sigma \leq W \\ &= 0 \quad \text{otherwise} \end{aligned}$$

where W is the distribution width.

Other bond-breaking criteria have been proposed : the bond-failure probability is set to be proportional to the bond deformation ($p \propto \Delta l$) [62], a bond breaks when its strain energy exceeds a prefixed threshold value [63], or more simply, the most stressed/strained bond is broken at any stage of the simulation [64, 68].

3.3.3 Examples of lattice models

Termonia and co-workers [60, 61] have modelled a two-dimensional single-phase polymer surface using a network of nodes connected in the x and y directions by elastic bonds representing the easily deformable and easily breakable regions (*cf* Fig 3.7). The nodes represent the elementary repeat units of the polymeric macromolecules. The network is stretched along the y axis by a constant force. A stochastic breakage law is implemented, the bond breakage probability being derived from Eq 3.3 and defined by :

$$p_i \propto e^{(-U_i+E_i)/k_B T}$$

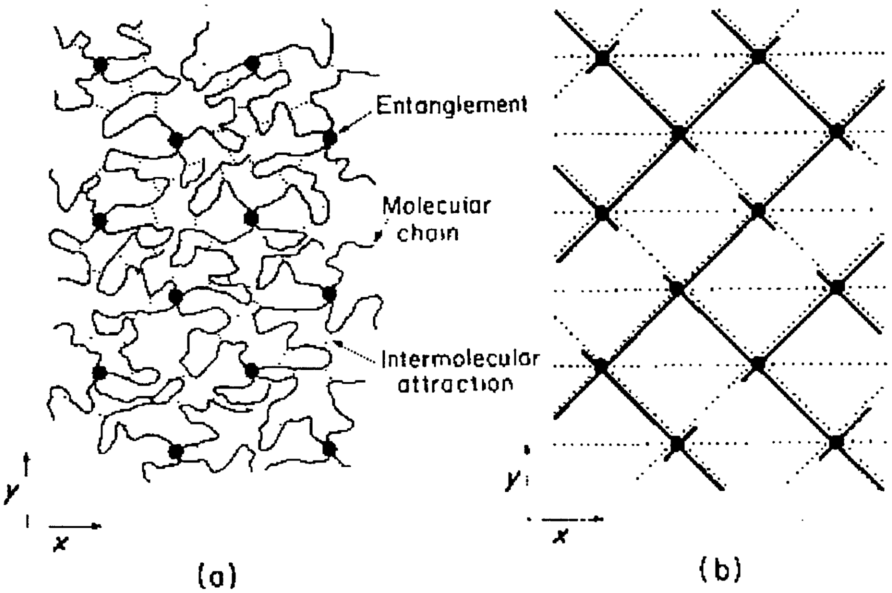

Figure 3.7: (a) Network representation of a polymer glass; (b) schematic representation (from [61])

where U_i is an activation energy, E_i is the elastic energy stored in the bond i, k_B is the Boltzmann's constant, and T is the absolute temperature. The elastic energy E_i is defined by :

$$E_i = \frac{1}{2}k_i(\Delta l_i)^2$$

in which k_i is the force constant for bond i and Δl_i is the bond's elongation. After a small number of bonds have been broken, the network is relaxed to its minimum energy configuration. This is realised using overrelaxation or block relaxation methods, the latter method being more efficient because it treats more than one node at a time. The authors used this model to study the fractal dimension of two-dimensional cracks and successfully applied it to the fracture of perfectly ordered and oriented polyethylene fibers.

The same stochastic bond-failure mechanism has been applied to creep rupture of polymers by Vujosevic and Krajcinovic [55]. Creep is a time-dependent deformation occuring in materials subjected to stress levels which are well below their mechanical strength. In [55], an unmodified epoxy matrix has been approximated by a two-dimensional, triangular lattice. A constant load σ has been applied to this network. For the purpose of modelling creep fracture in a thermoset polymer, the authors chose to use the energy form for the bond-failure rate as expressed in Eq 3.1 with $E(f)$ being the elastic energy stored in the bond (Eq 3.2. This model allowed the authors to show the exponential dependence of the time to failure t_f on the applied tensile stress as observed experimentally :

$$t_f \sim e^{-a\sqrt{\alpha}}$$

t_f is expressed as the sum over all the broken bonds of the bond breakage time as defined by Eq 3.4. The parameter a is a system-size dependent constant. Since lattice failure depends on the largest defect and since the size of stress-induced defects is distributed according to Weibull's law [57], the model successfully exhibited a distribution of the time to failure $F(t_f)$ governed by the Weibull distribution :

$$F(t_f) = 1 - e^{-\left(\frac{t_f}{t^*}\right)^m}$$

where m is the Weibull modulus (shape factor) and t^* is the scale factor.

A different model has been proposed by Hassold *et al* [63] in which a square lattice of Born springs, as explained below, is submitted to a uniaxial tensile strain. In this work, the spring breakage process does not obey a probabilistic law. Instead, the springs fail completely once a critical strain energy is exceeded. The advantage of using a Born-spring model compared to a Hookean-spring one lies in the fact that it penalises rotation of the spring away from lattice directions, as it is free to do in a Hookean-spring network. The Born potential energy for a two-dimensional lattice is given by :

$$E_i = \frac{1}{2}k_i(\Delta l_i)^2 + \frac{1}{2}c_i(\Delta d_i)^2$$

where k_i and c_i are constant potential parameters of spring i, Δl_i its elongation, Δd_i its deviation along its perpendicular axis. The first term accounts for spring stretching with a force constant k_i, which penalises deviations from the equilibrium length along the prefered spring direction. The second term accounts for the deviation of the spring from its preferred direction by inclusion of an additional spring with force constant c_i; this prevents the stressless elongation of the lattice due to spring rotation as observerd in the classical spring case.

3.3.4 Fuse networks

Another approach to fracture modelling is to consider the electric analogue of the elastic problem, replacing the force by the current and the displacement by the voltage. Electricity and elasticity are quite similar (Ohm's law versus Hook's law), so that this kind of model can capture some of the major physical aspects of the materials problem.

De Arcangelis and co-workers [64, 65] have presented models which are based on a two-dimensional network of linear resistors where each resistor can fuse if the voltage exceeds a threshold value. Different ways to distribute these threshold voltages are presented : they can be uniformly distributed over a lower and upper limits [64], or the distribution function can be a power-law or a Weibull distribution [65]. The results obtained from these models have proved to be consistent with those from mechanical models.

Similar work on random-fuse networks has been carried out by Duxbury and co-workers [66, 67]. They have studied the breakdown properties of 2D networks of resistors with a distribution of preset defects (pre-fused resistors or insulators). Above the percolation threshold, there is a connected path of fuses across the lattice. A voltage difference V is applied to the two opposite sides of the network which is then distributed between the resitors. When the potential difference applied across a resistor exceeds a common limit value, the resitor fuses and turns into a perfect insulator. To perform numerical simulations of this model, the basic numerical method is to solve Kirchhoff's current law at each node in the network. This gives rise to the following matrix equation to solve :

$$\mathbf{Mv} = \mathbf{b}$$

where **M** is a square sparse matrix representing the conductivity context of the lattice, **b** is the vector containing the applied external voltage and **v** is the solution vector of the voltage at each node of the network. Because **M** is very sparse, an iterative method (the Conjugate Gradient) is prefered to solve this system.

3.4 Other models

3.4.1 Dynamical models

Many models presented in the literature deal with static fracture. however, crack growth usually includes dynamical features which are left aside by those static models. Mori *et al.* [69] have proposed a more realistic model, based on a triangular lattice, which obeys the following equation :

$$m\frac{\mathrm{d}^2\mathbf{x_i}}{\mathrm{d}t^2} = -\eta\frac{\mathrm{d}\mathbf{x_i}}{\mathrm{d}t} + \sum_j \mathbf{F}\left(\mathbf{x_i} - \mathbf{x_j}\right) \tag{3.5}$$

where $\mathbf{x_i}$ is the displacement of the ith site and the sum runs over the neighbouring sites j of site i, m is the mass of the particle sitting on site i, η is the phenomenological viscosity, and **F** is the force between two sites which is linear in this model. **F** becomes null should the distance between two sites exceed a critical value x_c (that is, the bond breaks). Taguchi [70] has extended this model, introducing a short-range elastic potential :

$$U(\mathrm{x}) = \int \mathrm{dx}k\mathrm{x}U_0\left(x, x_c\right)$$

where $x = |\mathbf{x}|$ and $U_0(x, x_c)$ is choosen as a decaying function such as $exp\left[-(x/x_c)^2\right]$. The model obeys Eq. 3.5 with $\mathbf{F} = -k\mathbf{x}U_0(x, x_c)$.

3.4.2 Energetics models

Shimamura and co-workers [71, 72] have developed an energy-based model for crack growth in homogeneous materials. This model is based on the release and transfer of strain energy in a cubic lattice system. In terms of energetics, crack initiation and propagation are dissipation processes of the strain energy strored in solids. Shimamura [73] applied this model to impact fracture of brittle solids. During an impact, a certain amount of energy is communicated to the system, and, during crack extension, local strain energy disappears near both sides of the crack surface and it is transfered to the crack tips. In the cubic lattice system, a cube is seen as a grain which is the spatial unit for the storage, release and transfer of strain energy. A crack initiation and propagation process is introduced. If the strain energies of two adjacent grains E_i and E_j satisfy the condition : $E_iE_j \geq E_t^2$ (E_t is a cracking threshold energy, a crack is generated at the boundary of the two grains). The strain energies of the two grains are then reduced to zero and an energy E_r is released from the system. The remaining energy $E_i + E_j - E_r$ is equally transfered to the four grains at the crack tip. The simulations of impact fracture are performed in two steps. First, an initial strain energy is distributed through the system. Secondly, an impact energy is supplied to the system from a central grain on the lattice surface. The storage of strain energy is carried out by a random process and damage occurs when the cracking condition is satisfied. As the processes of energy storage and cracking proceed, the system eventually settles into a stationary state. Then the impact simulation is performed on this equilibrated system. The cracking condition and the subsequent release and transfer of strain energy are performed in the same way as described above.

Chapter 4

The model

4.1 The lattice

Lattice models have been successfully used in the study of disorder in a variety of statistical problems such as : percolation, disordered magnetic [74] and liquid crystalline [75] systems, macroscopic fluid simulation (lattice Boltzmann BGK [76]), etc. The aim of these models is not to reproduce the full quantitative details of the systems studied. Rather, they focus on the few key features that are considered most important in determining the physical behaviour of the investigated systems. This coarse approximation of real systems provides, nevertheless, satisfying insights and trends.

In the model used in this work, the surface or volume of the material is represented by a simple cubic lattice of nodes. Each node of the lattice is connected to its neighbours by bonds (4 in 2D, 6 in 3D). Each bond represents a mesoscopic portion of the system (it is *not* a single molecule) and has a set of parameters which characterise the nature of the represented material (polymer or rubber). The bonds are randomly distributed according to the desired rubber concentration Φ. A constant force is applied in the x direction at each end of the lattice, which results in the deformation and the elongation of the bonds. This elongation is governed by a Hookean law. Bonds are allowed to break according to a probabilistic law which depends on the bonds' elongation. When a bond is broken, it is removed from the lattice.

Figures 4.1 and 4.2 illustrate 2D- and 3D- lattice representations of the composite material. The rubber bonds are shown in green and the polymer bonds in red. The side bonds, on which the external stress is applied, are shown in blue. These are very strong and stiff in order to prevent the crack from going through one of the system's sides.

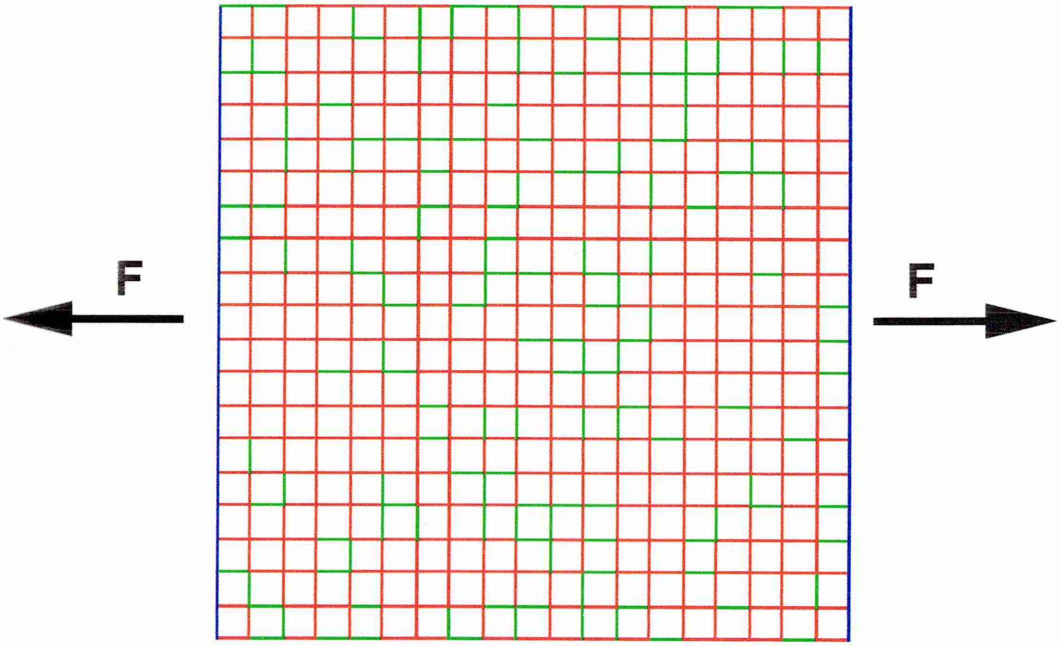

Figure 4.1: 2D-lattice representation of the composite material (20×20, $\Phi = 20\%$).

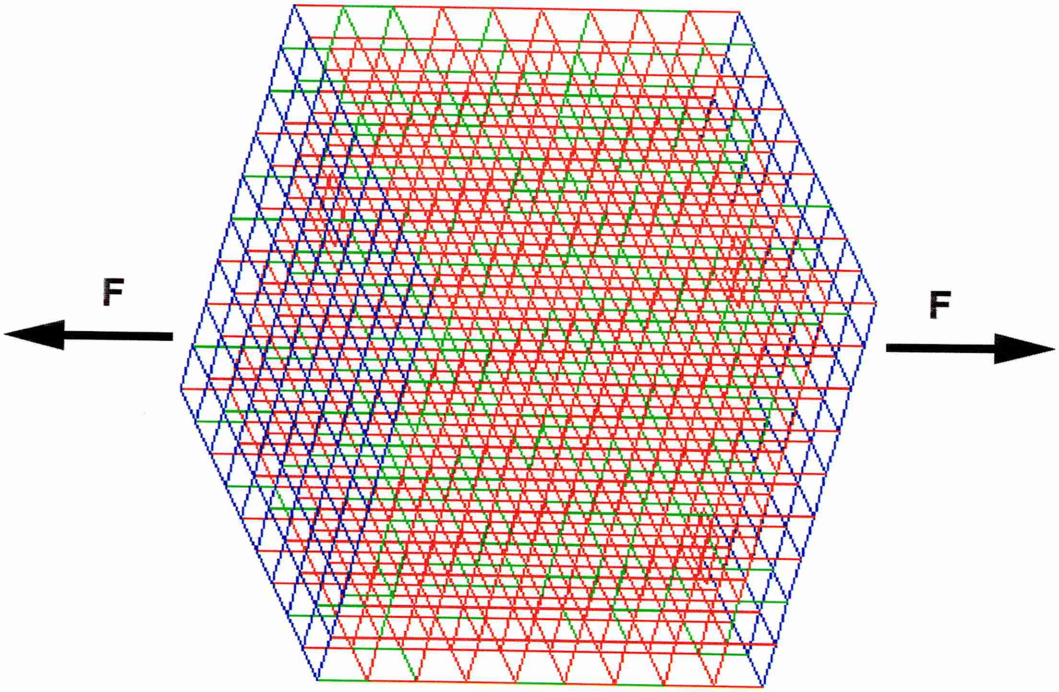

Figure 4.2: 3D-lattice representation of the composite material ($10 \times 10 \times 10$, $\Phi = 20\%$).

4.2 Deformation mechanism and breakage process

The aim of this model is to reproduce the deformation mechanisms which take place in rubber-toughened polymers under impact conditions. We focus on glassy polymer composites whose polymer matrix, in its unmodified version, behaves in a brittle manner at room temperature and is known to deform mainly by crazing (composite materials such as RT-PMMA or HIPS). Therefore, the stress-strain behaviour of the bonds is limited to being linear up to failure; the bonds are considered to be perfectly elastic. The model, then, does not reproduce plastic deformation mechanisms, such as shear yielding, as observed in other kinds of polymer composites (modified epoxy resins, nylon blends, etc.), or under other testing conditions (slow strain rates, high temperatures).

When stretched, the elastic bonds elongate according to the Hookean law :

$$f = k\Delta x \tag{4.1}$$

where :

f is the tensile force applied to the bond,

k is the bond's elastic coefficient,

Δx is the bond's elongation.

The bond's elongation is given by the difference of the displacement along the x axis of its two nodes :

$$\Delta x = x_1 - x_2$$

where :

x_1 is the displacement of one end of the bond relatively to its original position

x_2 is the displacement of the other end of the bond relatively to its original position

The bond breaking criterion used in this model derives from Eyring's reaction-rate theory as discussed in section 3.3.2. Following [53, 59], we therefore set the breakage probability of an elongated bond as a function of the elastic energy :

$$p_i = \frac{e^{-(E_a - E_i)/k_B T}}{p_{max}} \tag{4.2}$$

where :

E_a is a material dependent activation energy,

E_i is the elastic energy stored in the bond i,

k_B is the Boltzmann constant,

T is the absolute temperature

p_{max} is a normalization constant ($p_{max} = \sum_{i=1}^{n} e^{-(E_a - E_i)/k_B T}$).

The elastic energy is given by :

$$E_i = \frac{1}{2} k_i (\Delta x_i)^2$$

or

$$E_i = \frac{1}{2} f_i \Delta x_i$$

For polymers a considerable amount of experimental data [1] supports the idea that E_a is reduced by an amount which is proportional to the stress (σ). Therefore Eq. 4.2 can be rewritten as :

$$p_i = \frac{1}{p_{max}} e^{-(E_a - \beta\sigma)/k_b T} \tag{4.3}$$

where β can be interpreted as an activation area for three-dimensional systems. In a bond network context, β can be interpreted as an activation length (β') and σ can be replaced by the bond's stretching force f_i. Eq. 4.3 can be rewritten as follows :

$$p_i = \frac{1}{p_{max}} e^{-E_a/k_b T} e^{\beta' f_i / k_b T}$$

or

$$p_i = \frac{1}{p_{max}} e^{-E_a/k_b T} e^{\beta' k_i \Delta x_i / k_b T} \tag{4.4}$$

Eq. 4.4, which is expressed in energy terms, can be transposed into dimensionless force terms and renormalised without altering its validity as follows :

$$p_i = \frac{1}{p_{max}} e^{-f_a} e^{k_i \Delta x_i} \tag{4.5}$$

where :

f_a is a dimensionless material dependent constant corresponding to an activation force (force threshold or mechanical strength),

k_i is a material dependent constant with unit of inverse length which corresponds to the elastic coefficient of bond i.

The form of this probability law is shown in Fig 4.3 for $k_i = 1$ and different values of f_a. One can notice the steep rise in the breaking probability when the bond's sustained force $k_i \Delta x_i$ becomes greater than its force threshold f_a.

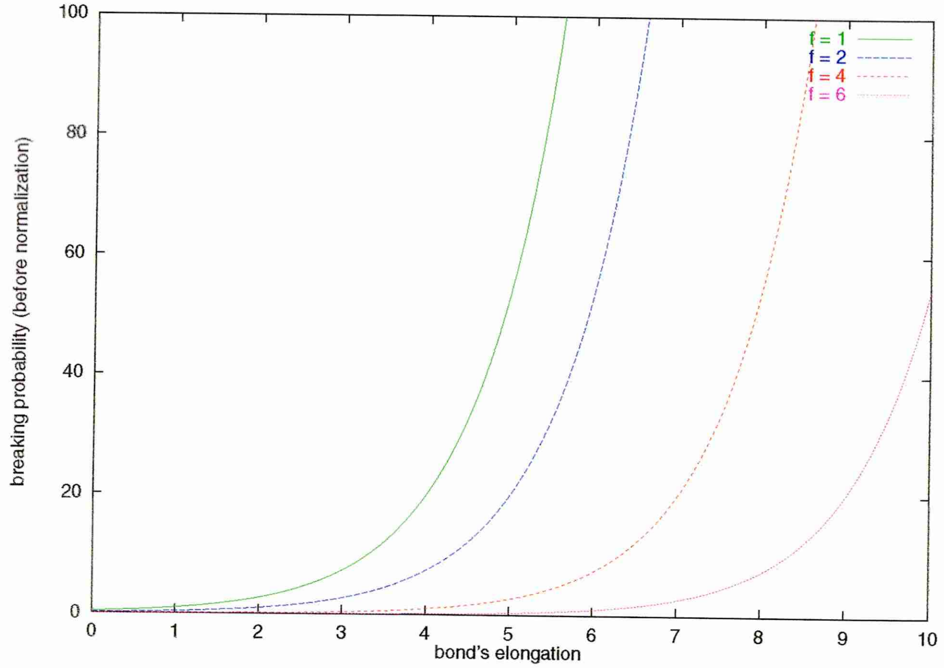

Figure 4.3: Bond breaking probability (before normalization) for different values of the force threshold f ($k = 1$).

4.3 Simulation step

At each step of the simulation, a single bond is to be broken. In order to select this bond, the breakage probability p_i must be worked out for each unbroken bond. This implies the calculation of every bond's elongation Δx_i when the system is at force equilibrium.

4.3.1 Equilibrating the system

Because the model is static, the system is allowed to return to a complete equilibrium state after each bond breakage. To simplify the calculation, we consider only the the forces that the system sustains in the direction of the external applied stress. The forces experienced by the bonds along the stretching direction x follow the Hookean law (Eq. 4.1). We assume that the same law governs the x-contribution of the forces on the bonds along the perpendicular directions (y and z), with their coefficient k accounting for their bending stiffness. The (x-contribution) forces on these bonds are then similarly expressed by Eq. 4.1, where Δx is the bond's bending displacement along the x axis. Therefore, for a given node i the force equilibrium can be expressed by :

$$\sum_{j=1}^{N_{nbour}} k_{ij}(x_{ij} - x_i) = 0$$

or

$$-K_i x_i + \sum_{j=1}^{N_{nbour}} k_{ij} x_{ij} = 0 \tag{4.6}$$

where :

N_{nbour} is the number of neighbouring nodes (4 in 2D systems, 6 in 3D systems),

k_{ij} is the elastic coefficient of the bond connecting node i to its jth neighbour,

$K_i = \sum_{j=1}^{N_{nbour}} k_{ij}$,

x_i is the displacement along the x axis of node i from its original position,

x_{ij} is the displacement along the x axis of the jth neighbouring node from its original position.

Fig 4.4 illustrates the load transfer occuring during the breakage of one bond (x direction bond) in a 2D system. View a shows the initial equilibrated situation for a node of the system fully connected to its four neighbours (North, South, East and West). In this case, the contribution of the perpendicular bonds (North and South) is null; we have then $f_W = -f_E$ and $f_N = f_S = 0$. View b presents the new equilibrated situation after the failure of the West bond. The contributions of the perpendicular bonds (f_N and f_S) are now balancing the East bond's new force (f_E'); we then have $f_N + f_S + f_E' = 0$. This node-level load transfer is extended to all the nodes of the system, and to non-uniform bond arrangements.

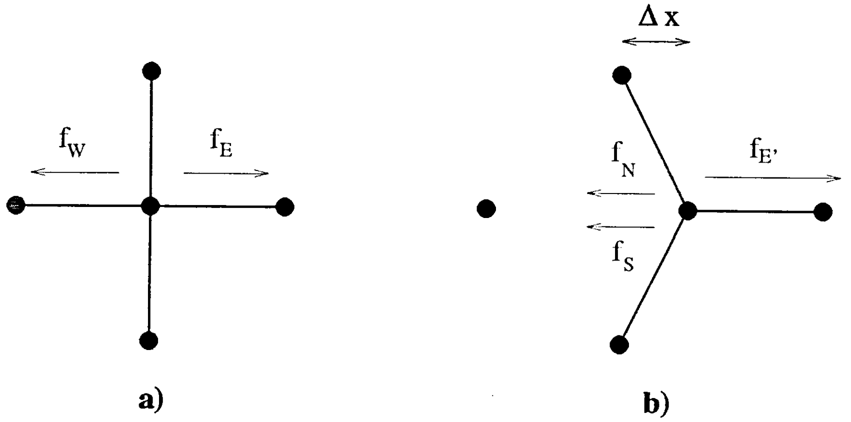

Figure 4.4: Load transfer on a node in a 2D system : a) undamaged situation, b) after failure of west bond.

Eq. 4.6 is valid for any node within the bulk of the material. It must be slightly altered for the boundary nodes, since these have fewer neighbours than the others. For these nodes

$$-\left(\sum_{j \neq j_{dir}}^{N_{nbour}} k_{ij}\right) x_i + \sum_{j \neq j_{dir}}^{N_{nbour}} k_{ij} x_{ij} = F_{dir} \tag{4.7}$$

where :

j_{dir} is the boundary direction index,

F_{dir} is the applied force.

4.3.2 Choosing the bond to break

When the system has been equilibrated, the breaking probabilities p_i are calculated. The bond choosing process must then satisfy this probability distribution. In order to select a bond in accordance with this, the following method is applied :

1. The exponential factors $e^{-f_a}e^{k_i \Delta x_i}$ are calculated for each bond and summed to give p_{max}. The individual probabilities, p_i, are then calculated using Eq. 4.5.
2. All the bonds' probabilities are added up keeping track of each bond's cumulated value $c_i = \sum_{j=1}^{i} p_j$ ($p_i = c_i - c_{i-1}$, with the convention $c_0 = 0$). The probabilities add up to 1 ($\sum_{i=1}^{N} p_i = c_N = 1$, N being the total number of unbroken bonds).
3. A random number r is generated ($0 < r \leq 1$).
4. The unique bond i which satisfies $c_{i-1} < r \leq c_i$ is the bond to be broken.

This method assures that the distribution of the breaking probabilities is respected. Indeed, the chances of a bond i being selected is equal to the span of its associated interval $]c_{i-1}, c_i]$. The method is illustrated in Fig. 4.5.

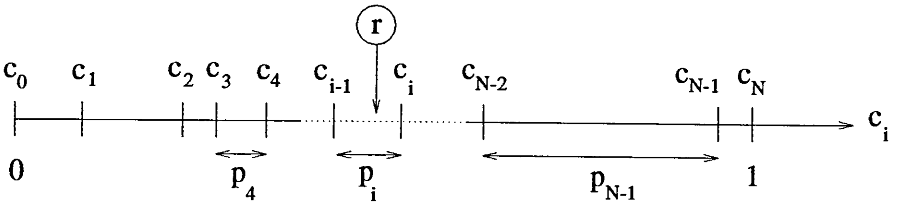

Figure 4.5: Bond selection method

4.4 Matrix form

The linear system of equations which results on applying equations 4.6 and 4.7 to all the nodes of the lattice can be written under the matrix form :

$$\mathbf{K}\mathbf{x} = \mathbf{f} \tag{4.8}$$

where :

K is the matrix of elastic coefficients

$$\mathbf{K} = \left(\begin{array}{ccccccccccc}
\ddots & \ddots & & & \ddots & & & & & & \\
\ddots & \ddots & \ddots & & & k_{i4} & & & & & \\
& \ddots & \ddots & \ddots & & & \ddots & & & & \\
& & \ddots & \ddots & \ddots & & & \ddots & & & \\
\ddots & & & \ddots & \ddots & k_{i3} & & & \ddots & & \\
& k_{i4} & & & k_{i3} & -K_i & k_{i1} & & & k_{i2} & \\
& & \ddots & & & k_{i1} & \ddots & \ddots & & & \ddots \\
& & & \ddots & & & \ddots & \ddots & \ddots & & \\
& & & & \ddots & & & \ddots & \ddots & \ddots & \\
& & & & & k_{i2} & & & \ddots & \ddots & \ddots \\
& & & & & & \ddots & & & \ddots & \ddots
\end{array}\right) \tag{4.9}$$

x is the vector of nodes' displacements,

$\mathbf{f}$ is the vector of applied forces.

The system's current equilibrium state is then given by the solution, $\mathbf{x}$, of Eq. 4.8. To solve this kind of equation, we need to use an appropriate numerical method. This will be presented in the next chapter.

4.5 Effect of the crack size on the failure stress

In this section we want to study the effect of the crack size on the failure stress. We consider a 2D system with a single initial straight and centered crack of length $2a$ perpendicular to the applied stress. as shown in Fig. 4.6.

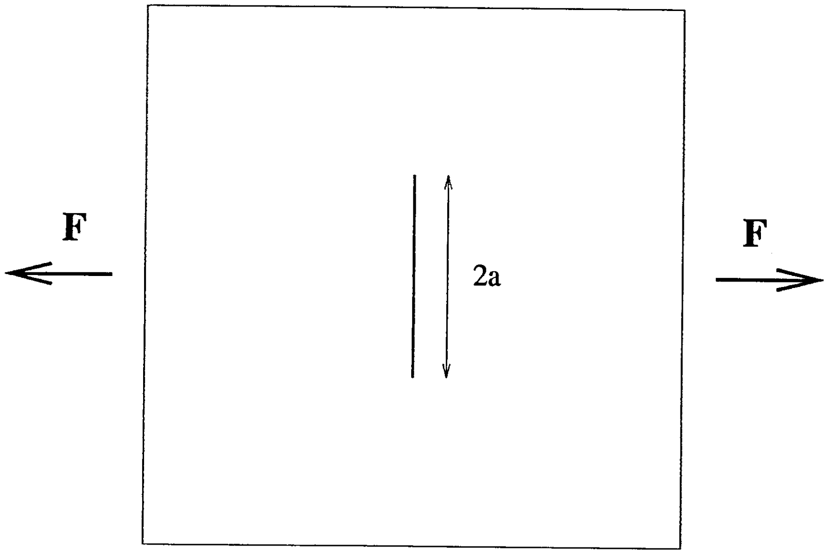

Figure 4.6: 2D system with initial crack of length $2a$.

In the model we present, one bond is broken at each simulation step, whatever the external applied stress. This process eventually forces the system to fail, even under very low applied stress. In order to determine an acceptable fracture stress, one must look at the damage at failure (d) versus the applied force (F) diagrams as shown in Fig 4.7 for different initial crack lengths $2a$ (in this figure, F is the force applied to each boundary bond). d is the number of broken bonds at material failure; in the case of a sharp crack extending from the initial one in a system of size n, the minimum value of d is $d_c = n - 2a$. We define the critical fracture force F_f as being the minimum applied force which leads to a failure damage $d = d_c$ (with a precision of one bond). When the external applied force F is greater than F_f, the failure damage d is always equal to d_c.

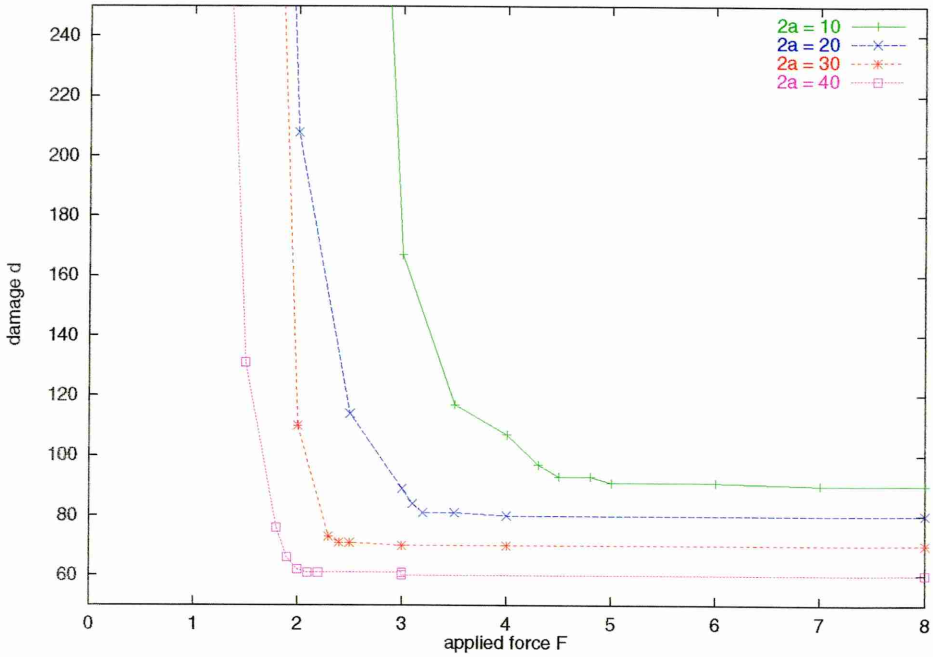

Figure 4.7: Damage d versus applied force F in 100×100 systems for different initial crack lengths $2a$.

Fig 4.8 shows the F_f-$\sqrt{a}$ relationship for two system sizes ($n = 100$ and 70). One can notice that, although the fits have non-null origin ordinates, they are linear and, therefore, the fracture force seems to obey the following form :

$$F_f = \frac{\alpha(n)}{\sqrt{a}} + F_0(n)$$

where $\alpha(n)$ and $F_0(n)$ are system size dependent parameters.

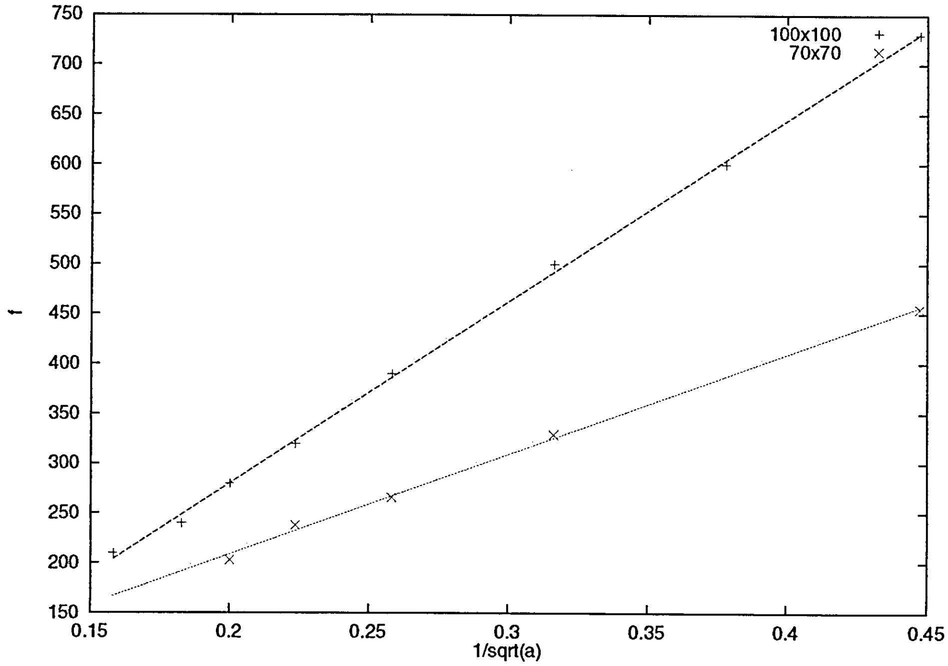

Figure 4.8: Plots and linear fits of fracture force F_f versus $\frac{1}{\sqrt{a}}$ for two different system sizes $n = 100$ and 70.

Chapter 5

Numerical methods

5.1 Introduction

Numerical methods to solve a system of linear equations fall in two main classes. *Direct* methods and *iterative* methods.

Direct methods, like the *Jordan's* method, *Gaussian elimination* or *Cholesky factorisation*, involve repeated application of a single process on the matrix to give the exact solution to the system after a finite number of operations; whereas *iterative* (or *indirect*) methods, such as *Jacobi's, Gauss-Seidel, successive over-relaxation (SOR)* and *Conjugate Gradient (CG)* methods, are based on the repetition of a rather simple converging process. The methods start from an initial approximation to the solution and then yield a value within a specified tolerance of the exact solution.

In the case of a system whose matrix of coefficients is *sparse*, with a high proportion of zero elements, as in Eq. 4.8, the use of iterative methods is preferred to the use of direct ones. The direct methods process all of the coefficients identically, zero or non-zero, whereas the iterative methods can be adapted to consider only the non-zero ones, especially in a diagonally sparse context. Moreover, direct methods tend to destroy the sparseness of the matrix, replacing zero elements with linear combinations of non-zero ones. Therefore the direct methods carry out operations on all the elements and reserve storage for all of them; on the other hand, iterative methods need only consider the non-zero coefficients and, since the sparseness of the matrix is maintained throughout the solving process, only storage for the non-zero coefficients is required.

The following iterative methods have been implemented in order to solve Eq. 4.8. The fastest one, which has been used to generate the results in Chapter 6, is the *conjugate gradient* method.

5.2 Jacobi's method

The first iterative method which has been tested is a very simple one, known as *Jacobi's* method. Usually this method is very slow and is just of theoretical interest. Let $\mathbf{A} = \{a_{ij}\}$ be an $n \times n$ non singular matrix, with non-zero diagonal elements, a_{ii}. Let the system to be solved be :

$$\mathbf{A}\mathbf{x} = \mathbf{b} \tag{5.1}$$

The matrix **A** can be expressed as the sum of three matrices :

$$\mathbf{A} = \mathbf{L} + \mathbf{D} + \mathbf{U} \tag{5.2}$$

where :

L is the lower triangular part of **A**

D is the diagonal part of **A**

U is the upper triangular part of **A**

Therefore Eq. 5.1 can be reformulated as follow :

$$\mathbf{D}\mathbf{x} = -(\mathbf{L} + \mathbf{U})\mathbf{x} + \mathbf{b}$$

whence

$$\mathbf{x} = -\mathbf{D}^{-1}(\mathbf{L} + \mathbf{U})\mathbf{x} + \mathbf{D}^{-1}\mathbf{b} \tag{5.3}$$

It is assumed that $\mathbf{D}^{-1} = diag(a_{11}^{-1}, \ldots, a_{nn}^{-1})$ exits, which is valid if $a_{ii} \neq 0, \forall i \leq n$.

From Eq. 5.3, the following recurrence relation can be established :

$$\mathbf{x}^{(r+1)} = -\mathbf{D}^{-1}(\mathbf{L} + \mathbf{U})\mathbf{x}^{(r)} + \mathbf{D}^{-1}\mathbf{b} \tag{5.4}$$

Where $\mathbf{x}^{(r)}$ is the estimated solution after r iterations.

Jacobi's method does not always converge, but a sufficient condition for convergence is that the matrix is *strictly diagonally dominant* i.e. :

$$\forall i \leq n, \qquad |a_{ii}| > \sum_{j \neq i}^{n} |a_{ij}|$$

5.3 Gauss-Siedel method

The Gauss-Siedel method is simply derived from the Jacobi's method. The idea behind the Gauss-Siedel method is that the new $x_i^{(r)}$ values can be used as soon as they are known. This requires storage of just one set of solution values ($\mathbf{x}^{(r)}$) instead of the two ($\mathbf{x}^{(r)}$ and $\mathbf{x}^{(r+1)}$) needed by the Jacobi's method.

This can be formulated by re-expressing Eq. 5.3 as follows:

$$\mathbf{x} = -\mathbf{D}^{-1}\mathbf{L}\mathbf{x} - \mathbf{D}^{-1}\mathbf{U}\mathbf{x} + \mathbf{D}^{-1}\mathbf{b} \tag{5.5}$$

whence the recurrent formulation:

$$\mathbf{x}^{(r+1)} = -\mathbf{D}^{-1}\mathbf{L}\mathbf{x}^{(r+1)} - \mathbf{D}^{-1}\mathbf{U}\mathbf{x}^{(r)} + \mathbf{D}^{-1}\mathbf{b} \tag{5.6}$$

In this rearrangement of the system, it appears that the vector quantity of $\mathbf{x}^{(r+1)}$ is found on both side of the equality. Actually, this vector formulation hides the fact that when the value of $x_i^{(r+1)}$ is being calculated using the i^{th} equation, the values of $x_1^{(r+1)}, \dots, x_{i-1}^{(r+1)}$ are already available. To better see this, Eq. 5.6 can be written in its scalar form: $\forall i \leq n$,

$$x_i^{(r+1)} = \frac{1}{a_{ii}} \left(-\sum_{j=1}^{i-1} a_{ij} x_j^{(r+1)} - \sum_{j=i+1}^{n} a_{ij} x_j^{(r)} + b_i \right)$$

This can be re-expressed as follows:

$$x_i^{(r+1)} = x_i^{(r)} + \frac{1}{a_{ii}} \left(-\sum_{j=1}^{i-1} a_{ij} x_j^{(r+1)} - \sum_{j=i}^{n} a_{ij} x_j^{(r)} + b_i \right)$$

or

$$x_i^{(r+1)} = x_i^{(r)} + d_i^{(r)} \tag{5.7}$$

with $\mathbf{d}^{(r)} = \left\{ d_i^{(r)} \right\}_{i \leq n}$ being the *displacement vector*. The vectorial form of Eq. 5.7 is simply :

$$\mathbf{x}^{(r+1)} = \mathbf{x}^{(r)} + \mathbf{d}^{(r)} \tag{5.8}$$

or

$$\mathbf{x}^{(r+1)} = \mathbf{x}^{(r)} + \left[\mathbf{D}^{-1}\mathbf{b} - \mathbf{D}^{-1}\mathbf{L}\mathbf{x}^{(r+1)} - \left(\mathbf{I} + \mathbf{D}^{-1}\mathbf{U} \right) \mathbf{x}^{(r)} \right] \tag{5.9}$$

This recurrent form of the Gauss-Siedel method as expressed in Eq. 5.8 leads to the next method, the *successive over-relaxation* method.

5.4 Successive over-relaxation method

In Eq. 5.8, the next estimation of the solution is deduced from the previous one by addition of the displacement vector. In order to speed up the convergence, a simple technique that can be used is to extend the new estimate a bit further along this displacement direction. The successive over-relaxation method (SOR) does this by increasing the displacement term by a factor ω, the *relaxation factor*, which usually lies between 1 and 2 (values between 0 and 1 can also be used, for which the term *under-relaxation* is more appropriate). The recurrent form of SOR is then

$$\mathbf{x}^{(r+1)} = \mathbf{x}^{(r)} + \omega \mathbf{d}^{(r)} \tag{5.10}$$

The method is not assured to converge for every initial guess $\mathbf{x}^0$, unless $0 \leq \omega \leq 2$. The rate of convergence is dependent on the value of ω and there is an optimal value ω_0 for which the convergence is the fastest.

All iterative methods can be expressed in the form

$$\mathbf{x}^{(r+1)} = \mathbf{M}\mathbf{x}^{(r)} + \mathbf{c}$$

where $\mathbf{M}$ is called the *iteration matrix* and $\mathbf{c}$ is a constant vector.

Therefore a recurrent expression of the SOR method is

$$\mathbf{x}^{(r+1)} = \mathbf{M}_S\mathbf{x}^{(r)} + \mathbf{c}$$

with $\mathbf{M}_S$ being the S.O.R. iteration matrix. An expression for $\mathbf{M}_S$ can be deduced from Eq. 5.9 : introducing the factor ω and reordering gives

$$\mathbf{M}_S = -\left(\mathbf{D} + \omega\mathbf{L}\right)^{-1}\left[(\omega - 1)\,\mathbf{D} + \omega\mathbf{U}\right]$$

The optimal over-relaxation factor, ω_0, may be determined by minimising the *spectral radius* of M_S, $\rho(\mathrm{M}_S)$ (the *spectral radius* $\rho(\mathrm{M})$ of a matrix M is defined by $\rho(\mathrm{M}) = \max\{|\lambda_i|\}$ where the λ_i are the eigenvalues of M). This can be done indirectly by minimising the spectral radius of M_G, the iteration matrix of the Gauss-Siedel method, since the following relation holds

$$\rho\left(\mathrm{M}_G\right) > \rho\left(\mathrm{M}_S\right).$$

ω_0 can be expressed in term of the spectral radius of the Gauss-Siedel iteration matrix [78], $\rho\left(\mathrm{M}_G\right)$ as follows

$$\omega_0 = \frac{2}{1+\sqrt{1-\rho\left(\mathrm{M}_G\right)}} \tag{5.11}$$

The problem is then to work out the value of $\rho\left(\mathrm{M}_G\right)$, or ρ_G.

It can be shown [78] that, when $r \to \infty$,

$$\mathbf{d}^{(r+1)} \to \rho_G \mathbf{d}^{(r)}$$

Therefore ρ_G can be evaluated by averaging all the $\left(\frac{d_i^{(r+1)}}{d_i^{(r)}}\right)_{i \leq n}$ when $r \to \infty$, as follows

$$\rho_G = \lim_{r \to \infty} \frac{\sum_{i=1}^{n} \frac{d_i^{(r+1)}}{d_i^{(r)}}}{n} \tag{5.12}$$

In the implementation of the SOR method, the computation of Eq. 5.12 is actually performed periodically after a large number of iteration steps have been processed. The longer this calculation period, the more accurate the value of ρ_G. The first simulation step is carried out with an initial value of $\omega = 1$. When a new value of ρ_G is available, it is used in Eq. 5.11 in order to update the estimation of the optimal over-relaxation factor, ω_0.

5.5 Conjugate gradient method

Another iterative method, totally different form the three just described, has also been implemented and tested : the *conjugate gradient* method (CG). It has been found that for the intrinsically inhomogeneous problem dealt with in this work, this method is faster than all others tested.

If the matrix **A** in Eq. 5.1 is symmetric and positive definite, then the solution of this system of linear equations is equivalent to the minimization of the following quadratic function

$$\mathcal{Q}(\mathbf{x}) = \frac{1}{2}\mathbf{x}\mathbf{A}\mathbf{x} - \mathbf{b}\mathbf{x}. \tag{5.13}$$

Indeed, making its gradient

$$\nabla\mathcal{Q}(\mathbf{x}) = \mathbf{A}\mathbf{x} - \mathbf{b}$$

null is equivalent to solving Eq. 5.1.

The CG method consists of generating a sequence of direction vectors which move from the original guess to the solution. The reccurent form of the method is

$$\mathbf{x}^{(r+1)} = \mathbf{x}^{(r)} - \alpha_r \mathbf{p}^{(r)}$$

where the $\mathbf{p}^{(r)}$ are the direction vectors and the α_r are the scalars which determine the distance to be moved along direction $\mathbf{p}^{(r)}$. The problem, then, is to choose the α_r and the $\mathbf{p}^{(r)}$. A natural way to choose the α_r is to minimise $\mathcal{Q}$ along the direction $\mathbf{p}^{(r)}$. Therefore α_r must satisfy

$$\mathcal{Q}(\mathbf{x}^{(r)} - \alpha_r \mathbf{p}^{(r)}) = \min_{\alpha} \mathcal{Q}(\mathbf{x}^{(r)} - \alpha \mathbf{p}^{(r)}) \tag{5.14}$$

To simplify the notation, the superscripts are dropped and we write $q(\mathbf{x}) = \mathcal{Q}(\mathbf{x} -$

$\alpha\mathbf{p}$). Then, using Eq. 5.13

$$\begin{aligned} q(\mathbf{x}) &= \frac{1}{2}(\mathbf{x}-\alpha\mathbf{p})\mathbf{A}(\mathbf{x}-\alpha\mathbf{p})-\mathbf{b}(\mathbf{x}-\alpha\mathbf{p}) \\ &= \frac{1}{2}\mathbf{xAx}-\alpha\mathbf{pAx}+\frac{1}{2}\alpha^2\mathbf{pAp}+\alpha\mathbf{pb}-\mathbf{bx} \\ &= \frac{1}{2}\mathbf{pAp}\alpha^2-\mathbf{p}(\mathbf{Ax}-\mathbf{b})\alpha+\frac{1}{2}\mathbf{x}(\mathbf{Ax}-2\mathbf{b}) \end{aligned}$$

it follows that

$$\frac{dq(\alpha)}{d\alpha}=\mathbf{pAp}\alpha-\mathbf{p}(\mathbf{Ax}-\mathbf{b})$$

To satisfy Eq. 5.14, we need $\frac{dq(\alpha)}{d\alpha}=0$. Since $\mathbf{A}$ is positive definite, $\mathbf{pAp}>0$, therefore

$$\alpha=\frac{\mathbf{p}(\mathbf{Ax}-\mathbf{b})}{\mathbf{pAp}} \tag{5.15}$$

The name of the C.G. method originates from the fact that it generates direction vectors which are orthogonal, with respect to $\mathbf{A}$. This means that

$$\mathbf{p}^{(i)}\mathbf{A}\mathbf{p}^{(j)}=0, \quad i\neq j. \tag{5.16}$$

An interesting property of this method of generating the direction vectors is that, since the solution space has dimension n, the solution is assured to be reached after a maximun of n iterations. If the initial error vector $\epsilon^{(0)}=\hat{\mathbf{x}}-\mathbf{x}^{(0)}$, $\hat{\mathbf{x}}$ being the exact solution of Eq. 5.1, $\epsilon^{(0)}$ can be decomposed uniquely in the $\left\{\mathbf{p}^{(i)}\right\}_{i\leq n}$ space base.

The iteration step of the C.G. algorithm can be formulated as follows (the iteration index here being k and $\mathbf{r}^{(k)} = \mathbf{b} - \mathbf{A}\mathbf{x}^{(k)}$ being the residual at the kth step).

Choose $\mathbf{x}^{(0)}$. Set $\mathbf{p}^{(0)} = \mathbf{r}^{(0)} = \mathbf{b} - \mathbf{A}\mathbf{x}^{(0)}$.

For $k = 0, 1, ...$

$$\begin{aligned}
\alpha_k &= -\frac{\mathbf{r}^{(k)}\mathbf{r}^{(k)}}{\mathbf{p}^{(k)}\mathbf{A}\mathbf{p}^{(k)}} && (5.17)\\
\mathbf{x}^{(k+1)} &= \mathbf{x}^{(k)} - \alpha_k\mathbf{p}^{(k)} && (5.18)\\
\mathbf{r}^{(k+1)} &= \mathbf{r}^{(k)} + \alpha_k\mathbf{A}\mathbf{p}^{(k)} && (5.19)\\
\text{if } \|\mathbf{r}^{(k+1)}\| &\geq \epsilon, \text{ continue} && (5.20)\\
\beta_k &= \frac{\mathbf{r}^{(k+1)}\mathbf{r}^{(k+1)}}{\mathbf{r}^{(k)}\mathbf{r}^{(k)}} && (5.21)\\
\mathbf{p}^{(k+1)} &= \mathbf{r}^{(k+1)} + \beta_k\mathbf{p}^{(k)} && (5.22)
\end{aligned}$$

Eq. 5.19 is equivalent to $\mathbf{r}^{(k+1)} = \mathbf{b} - \mathbf{A}\mathbf{x}^{(k+1)}$ since

$$\begin{aligned}
\mathbf{r}^{(k+1)} &= \mathbf{b} - \mathbf{A}\mathbf{x}^{(k+1)}\\
&= \mathbf{b} - \mathbf{A}(\mathbf{x}^{(k)} - \alpha_k\mathbf{p}^{(k)})\\
&= \mathbf{b} - \mathbf{A}\mathbf{x}^{(k)} + \alpha_k\mathbf{A}\mathbf{p}^{(k)}\\
&= \mathbf{r}^{(k)} + \alpha_k\mathbf{A}\mathbf{p}^{(k)}.
\end{aligned}$$

Eq. 5.17 is actually equivalent to Eq. 5.15, since starting from Eq. 5.19 it can be deduced

$$\begin{aligned}
\mathbf{p}^{(k)}\mathbf{r}^{(k+1)} &= \mathbf{p}^{(k)}\left(\mathbf{r}^{(k)} + \alpha_k\mathbf{A}\mathbf{p}^{(k)}\right)\\
&= \mathbf{p}^{(k)}\mathbf{r}^{(k)} + \alpha_k\mathbf{p}^{(k)}\mathbf{A}\mathbf{p}^{(k)}
\end{aligned}$$

then from the definition of α_k in Eq. 5.17

$$\mathbf{p}^{(k)}\mathbf{r}^{(k)} + \alpha_k\mathbf{p}^{(k)}\mathbf{A}\mathbf{p}^{(k)} = 0$$

therefore

$$\mathbf{p}^{(k)}\mathbf{r}^{(k+1)} = 0 \tag{5.23}$$

Finally, rewriting Eq. 5.22 for rank k and multiplying both sides of the equation by $\mathbf{r}^{(k)}$ gives

$$\begin{aligned} \mathbf{r}^{(k)}\mathbf{p}^{(k)} &= \mathbf{r}^{(k)}\left(\mathbf{r}^{(k)} + \beta_{k-1}\mathbf{p}^{(k-1)}\right) \\ &= \mathbf{r}^{(k)}\mathbf{r}^{(k)} + \beta_{k-1}\mathbf{r}^{(k)}\mathbf{p}^{(k-1)}. \end{aligned}$$

Then using the result of Eq. 5.23

$$\mathbf{r}^{(k)}\mathbf{p}^{(k)} = \mathbf{r}^{(k)}\mathbf{r}^{(k)}$$

therefore, replacing $\mathbf{r}^{(k)}\mathbf{r}^{(k)}$ by $\mathbf{r}^{(k)}\mathbf{p}^{(k)}$ in Eq. 5.17 gives

$$\alpha_k = -\frac{\mathbf{r}^{(k)}\mathbf{p}^{(k)}}{\mathbf{p}^{(k)}\mathbf{A}\mathbf{p}^{(k)}} \tag{5.24}$$

as stated in Eq. 5.15.

5.6 Efficiency of the Numerical Methods

We present here data measuring the comparative efficiency of the SOR and CG methods for our types of problems and the CG's efficiency for different heterogeous systems. Their applicability to our problem is presented in appendix A.

5.6.1 SOR versus CG

The SOR method is well-adapted for problems with high correlation between neigbouring values, as, for example, in the numerical solution of differential equations using a discrete grid in a homogeneous medium. But in the system studied in this thesis, there are two kinds of inhomogeneity:

- The material is a two-component material (polymer + rubber)
- As cracks appear and interconnect, the material fragments, decreasing the correlation level between neigbouring sites (Fig 5.1).

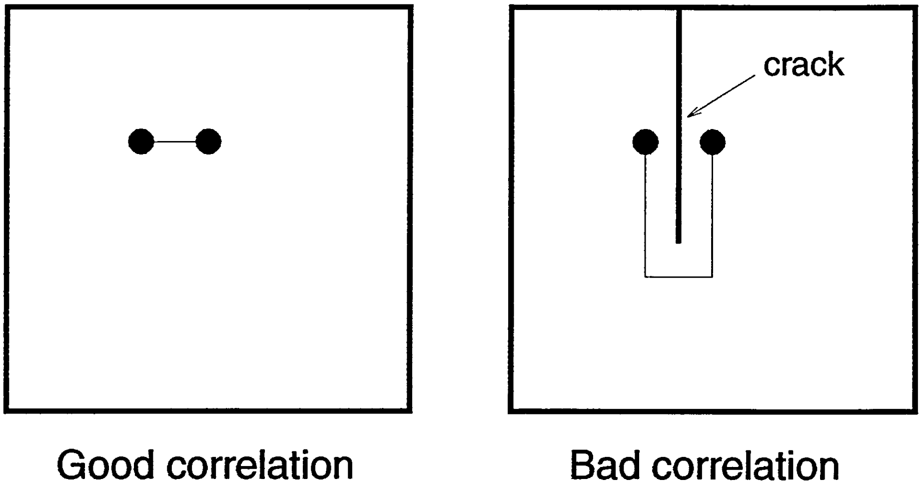

Figure 5.1: Correlation level between two neighbouring nodes in undamaged (left) and damaged (right) systems

This induces a slowing down of the nominal convergence rate. This becomes specially painful forwards the end of the simulation, when the material is, in effect, constituted by several almost dissociated parts (Fig 5.2).

This problem, though also present with CG, seems to be of less importance. Fig 5.3 shows the comparative performances of SOR and CG for systems with different rubber concentrations. From this figure, CG is clearly faster than SOR, being almost twice as fast as for low rubber loadings.

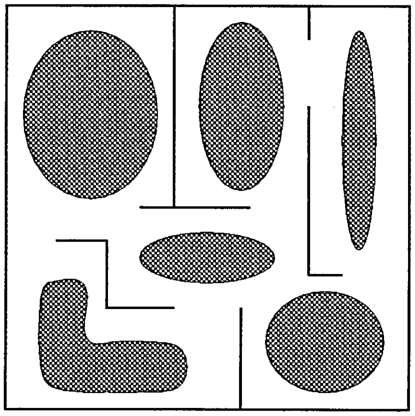

Figure 5.2: Creation of decorrelated sub-systems in a highly damaged system

5.6.2 CG convergence rate

The comparative evolution of the CG convergence rate during the whole simulation is shown in Fig 5.4 for different rubber loadings. The number of CG iterations required to reach the solution is plotted at each simulation step, for three different degrees of heterogeneity : $0\%, 20\%$ and 40% rubber loading.

The convergence rate is evidently dependent on the degree of heterogeneity of the system: the purer the system is, the faster CG converges to the solution. As the simulation draws closer to the material failure, the damage increases to a point where certain neighbouring nodes are highly decorrelated (*cf* Fig 5.2) and, as for SOR, the convergence rate of the method rapidly decays.

5.7 Divergence and Material failure detection

At the material failure point, when the damage in the system eventually creates a main crack, we end up with two totally decorrelated sub-systems. In this situation, there is no solution to Eq. 4.8 and the iterative solving methods diverge.

An advantage of CG lies in the fact that, though it looks like an iterative method, it

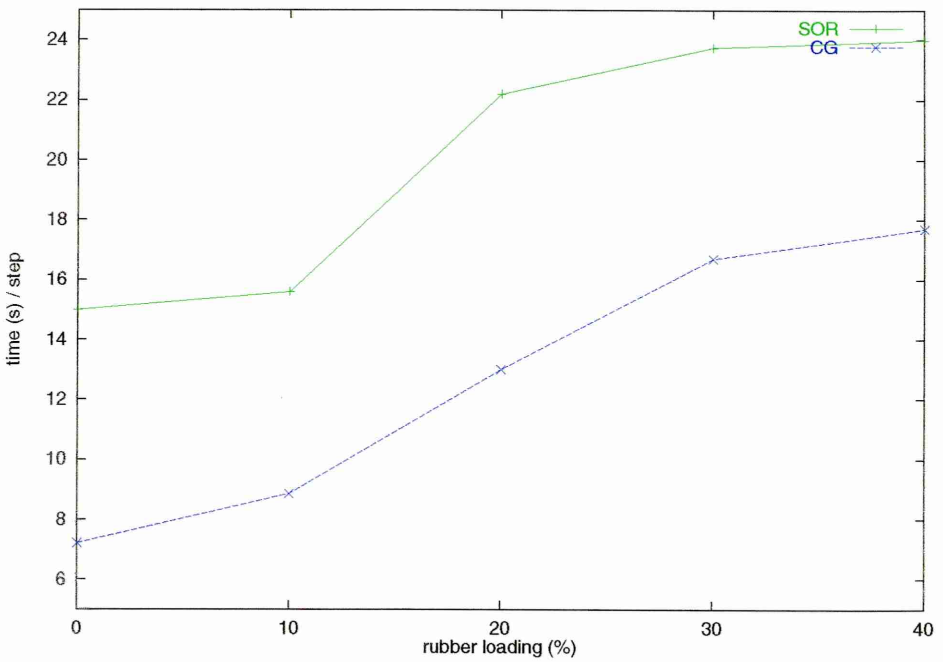

Figure 5.3: Comparison of the average simulation step time for SOR and CG in 70 × 70 systems for different rubber loadings

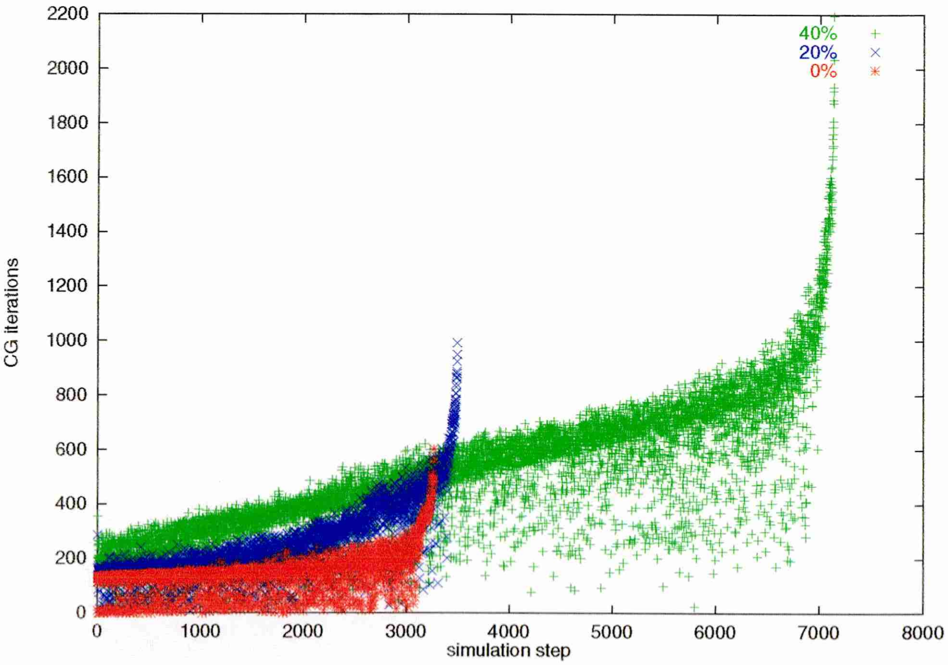

Figure 5.4: Evolution of the CG convergence rate in $20 \times 20 \times 20$ systems for different rubber loadings

is actually a direct one in the sense that when a solution exists, it is bound to reach it after a maximum of n iterations, n being the solution space dimension. Thus, when the material failure point is passed and the system has no solution, the CG method reaches the iteration limit n without converging. The material failure test is therefore very unexpensive and easy to implement :

```
begin simulation
    do
        nIter ← 0
        do
            CG iteration
            nIter ← nIter + 1
        while $||\mathbf{r}|| \geq \epsilon$ and nIter $< n$
        if nIter $< n$ then
            bond breaking
    while nIter $< n$
    material failure
end simulation
```

$||\mathbf{r}||$ is the CG residual (*cf* Eq. 5.20), ϵ, the required convergence precision and `nIter` the CG iteration counter.

Chapter 6

Damage results

6.1 Introduction

Two kinds of analysis were performed on the data obtained from the different simulations. One concerns the damage (in the sense which will be defined shortly) the system undergoes before failure and related results such as the crack complexity, whereas the other concerns the stress evolution in the system during the bond breaking process. Simulations were mainly carried out on 3D systems but data were also obtained for 2D systems. We also examined the effects of the finite system size on the simulation results.

In our model, the failure behaviour of the simulated composite material is driven by three kinds of parameters :

- The rubber loading Φ
- The bond elastic coefficients k_p (polymer) and k_r (rubber), relating stress to strain on each bond
- The bond force thresholds, as defined prefiously, F_p (polymer) and F_r (rubber)

The relevant parameters for this model are a) the ratio value of k_p and k_r, and b) the difference between F_p and F_r. We have therefore studied the effects of the variation of just the rubber parameters (k_r,F_r), the polymer parameters (k_p,F_p) being both set to 1.0. These studies have been carried out for the full range of rubber loadings ($0\% \leq \Phi \leq 100\%$).

We have also extended the study of this model to macro-systems where the shapes of the rubber particles are simulated more realistically.

6.2 Damage

The more impact-resistant a material is, the more impact energy it is able to dissipate before it fails. In this lattice model, the energy dissipating process is bond breakage (loss of elastic energy stored in a bond). We therefore expect that the damage a system undergoes before catastrophic failure (i.e. the number of broken bonds before failure) is a measure of its impact-toughness. The situation is made more complex because the energy dissipated by bonds of different types might not necessarily be the same. Nevertheless, we continue to use the number of broken bonds as a crude measure of toughness. A comparison of the experimental data with our simulation results will be presented to justify this assumption to some extent.

We define the damage d as the ratio of the number of bonds (polymer plus rubber) broken before the complete failure of the material with the total number of bonds in the system.

$$d = \frac{N_b}{N_T}$$

Here N_b is the number of broken bonds and N_T is the total number of bonds in the undamaged system.

6.2.1 System size dependence

Fig. 6.1 presents the system size dependence results for 2D systems. The rubber parameters are $k_r = 0.1$ and $F_r = 8$. The data points have been averaged between 4 and 10 systems. For a rubber loading $\Phi = 20\%$, the relative damage d seems to be constant (around $d = 10\%$) and not to depend significantly on the system size once it exeeds 20×20. For $\Phi = 40\%$, the system size dependence seems to be greater but it also weakens after a certain size (about 40×40). As for $\Phi = 20\%$, the system size effects appear relatively unimportant from 70×70 upwards.

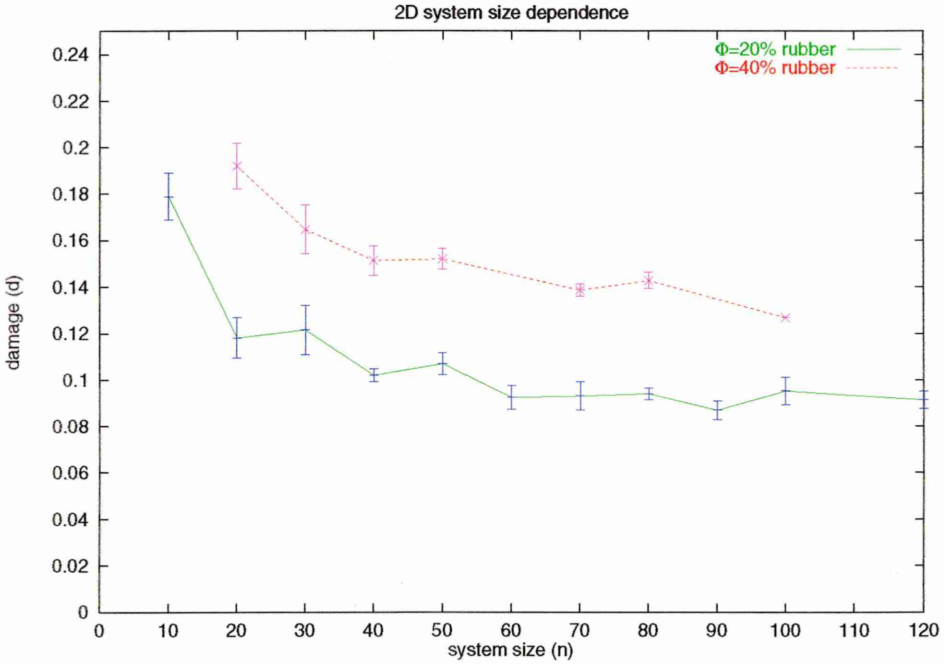

Figure 6.1: Damage system size dependence in 2D systems for $\Phi = 20\%$ and $\Phi = 40\%$

An explanation of the small systems results may be the discrepancy of the rubber loading in these systems. Indeed, the proportion of stiff boundary bounds is not negligible and therefore alters measurably the actual ratio of rubber and polymer bonds (the proportion of these stiff bonds is system size dependent). This problem tends to disappear with the increase of the system size. A good balance between the computational cost of system size and the desire to reduce size dependence is achieved for 70 × 70 systems. The 2D damage studies presented in what follows will therefore be carried out for this system size.

For 3D systems, the results of Fig. 6.2 show that for $\Phi = 20\%$ rubber loading ($k_r = 0.1$,$F_r = 8$) the damage does not seem to be size dependent. Indeed, for all the system sizes simulated, the damage is virtually constant, at about $d = 0.15$. We do not see any small system size effects as was the case for the 2D systems. We note that here, for a given system size, the proportion of boundary bonds is less important : let n be the system size; for 2D systems the proportion of boundary bonds is $\Phi_b = \frac{2n}{2n^2} = \frac{1}{n}$, whereas for 3D systems it is $\Phi_b = \frac{2n^2}{3n^3} = \frac{2}{3}\frac{1}{n} < \frac{1}{n}$. However this difference seems too small to account for the lack of system size dependence observed in 3D systems. As an alternative, one can advance an explanation based on the increased connectivity.In a 3D system each node is, on average, connected to 6 neighbours, compared with 4 in 2D systems. This might make 2D systems more sensitive to small system sizes.

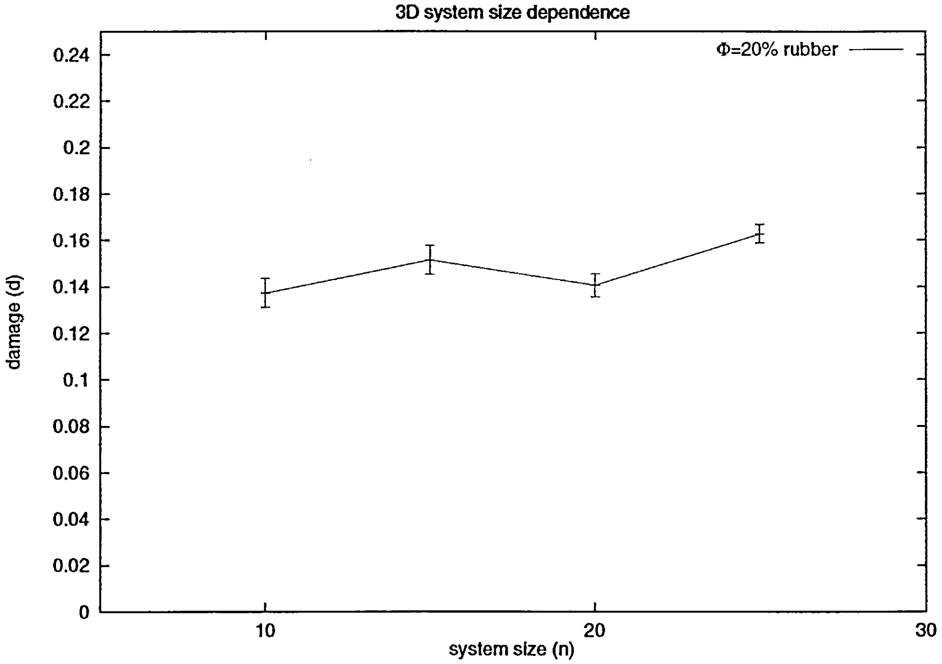

Figure 6.2: Damage system size dependence in 3D systems

2D and 3D simulations show that for systems in which the boundary bond proportion is relatively small (this occurs for relatively big systems) one can assume that the damage d is system size independent. This allows us to perform simulations on finite size systems and to draw system size independent conclusions from their results.

6.2.2 Rubber loading effects

General trend

The general evolution of the damage, d, with the rubber loading, Φ, is shown in Fig. 6.3. These results were obtained for 3D systems ($20 \times 20 \times 20$) with parameter values of $k_r = 0.05$ and $F_r = 8$ (these values were chosen because of the clarity of the damage trend). The external applied force F was set to 2 (this value will be used in all the simulations, unless specified otherwise). Each data point has been averaged over 5 systems.

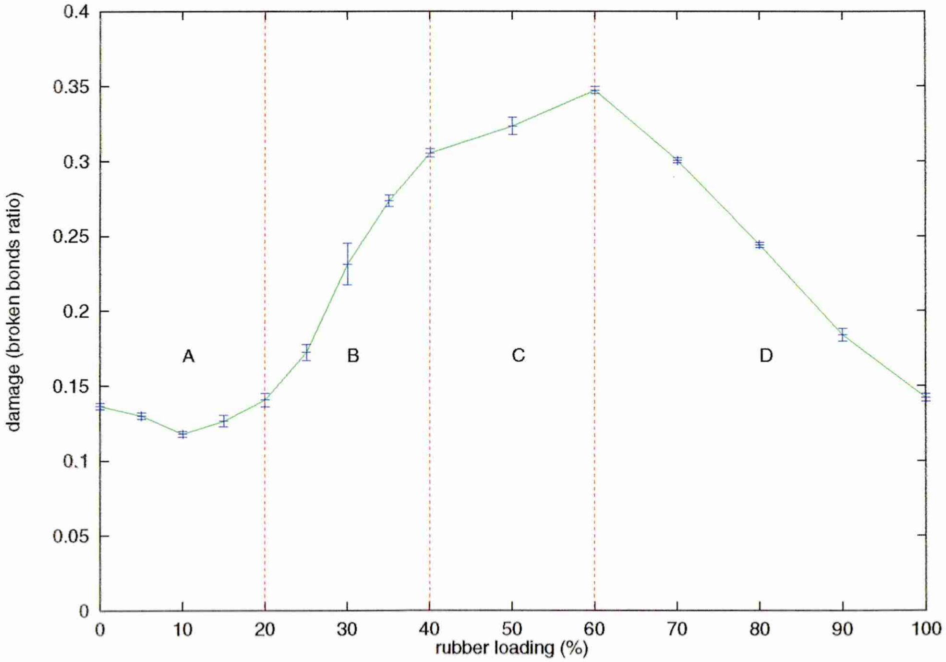

Figure 6.3: Typical damage in $20 \times 20 \times 20$ systems

From this figure we can roughly divide the rubber concentration effects into four regions, which, in future discussions, we shall for convenience refer to as :

A : $\Phi < \Phi_B \approx 20\%$, embrittlement region

B : $\Phi_B \leq \Phi < \Phi_C \approx 40\%$, toughening region

C : $\Phi_C \leq \Phi < \Phi_D = 60\%$, saturation region

D : $\Phi_D \leq \Phi$, weakening region.

The most surprising result is in region **A**. For a small amount of rubber, one might have expected a steady increase of the toughness with the increase in rubber loading as observed for region **B**. This apparently anomalous result can, alternatively, be interpreted as an actual embrittlement phenomenon which occurs when the rubber particles are sparsely distributed within the polymer bulk. As it will be shown later on, rubber particles act as crack initiators (their ability to stretch inducing high stress in the stiffer surrounding polymer matrix), and as crack terminators. Fig 6.4 illustrates these two roles. When there are just a few rubber particles, they are not sufficient to terminate neighbouring cracks but act, none the less, as crack initiation sites themselves. Therefore, once cracks initiate preferentially around these sites, such cracks grow, with one of them becoming dominant rather quickly. As such, catastrophic failure happens with very little damage throughout the system.

This embrittlement may alternatively be viewed as being a result of a pre-damage imposed on the system by the presence of the rubber bonds. In this scenario, the rubber bonds may be viewed as acting as partially broken bonds (due to their low elastic modulus) around which the stress is higher than elsewhere in the system (as it is around real broken bonds). This embrittlement mechanism leads to faster main crack formation and, thus, with no mechanisms for crack termination, lead to earlier material failure. The initial proportion of rubber bonds (Φ) is, then, related to the initial amount of broken bonds (or pre-damage Δd). This pre-damage value

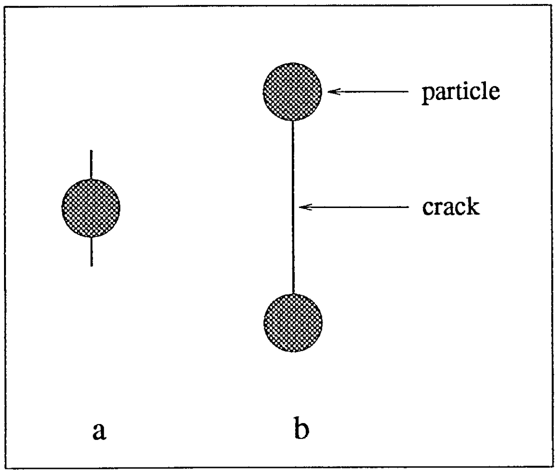

Figure 6.4: Roles of rubber particles : a) crack initiator, b) crack terminator

Δd tends to Φ when the rubber coefficient k_r approaches to zero :

$$\lim_{k_r \to 0} \Delta d = \Phi \tag{6.1}$$

We define the main crack ratio as the broken bonds belonging to the main crack divided by the total number of broken bonds. Fig 6.5 shows the evolution of the main crack ratio with the percentage of simulation performed for $k_r = 0.05$ and $F_r = 16$ and for different rubber loadings Φ. For $\Phi < \Phi_B$, the graph shows a sharp upturn. We note a correlation between the degree of embrittlement and the location of the sharp upturn, late on in the simulation. The table below shows the approximate values for the catastrophic regime relative onset t_c for different rubber loadings (the double vertical line separates the embrittlement and the toughening regions) :

Φ	0%	5%	10%	20%	50%
t_c	92%	87%	80%	96%	98%

It must be noticed that, even though their total damage value is similar, the $\Phi = 0\%$ and $\Phi = 20\%$ systems have very different main crack evolution pattern. Pure

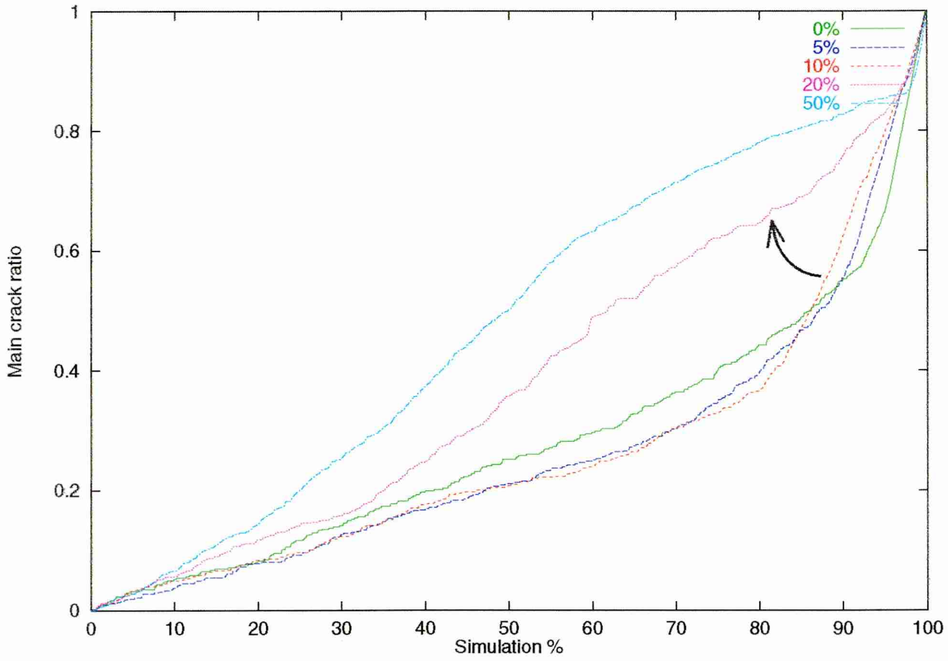

Figure 6.5: Main crack evolution in a $20\times20\times20$ system for different rubber loadings ($k_r = 0.05, F_r = 16$) - the arrow indicates the brittle/tough transition

systems, like the "brittle" ones, are characterised by a constant main crack formation speed before the sharp upturn. For $\Phi = 20\%$ systems, the main crack evolution is not so regular.

When the proportion of rubber bonds exceeds Φ_B, it appears that the balance between embrittlement and toughening mechanisms is reversed and the composite system becomes able to sustain more damage before breakdown than a pure glassy polymer one (region **B**). The role of the rubber particles is to initiate localised energy absorbing mechanisms, such as, in this bond model, through bond breakage. When the number of rubber particles is large enough, numerous small local crack initiations occur. These act as energy dissipators, and so prevent small neighbouring cracks from developing into a main crack. Widespread damage occurs throughout the whole volume of the material and its failure is delayed by the presence of rubber bonds bridging the crack surfaces. Crack-bridging is illustrated in Fig 6.6.

As we increase Φ we can see a phenomenon of saturation of the rubber toughen-

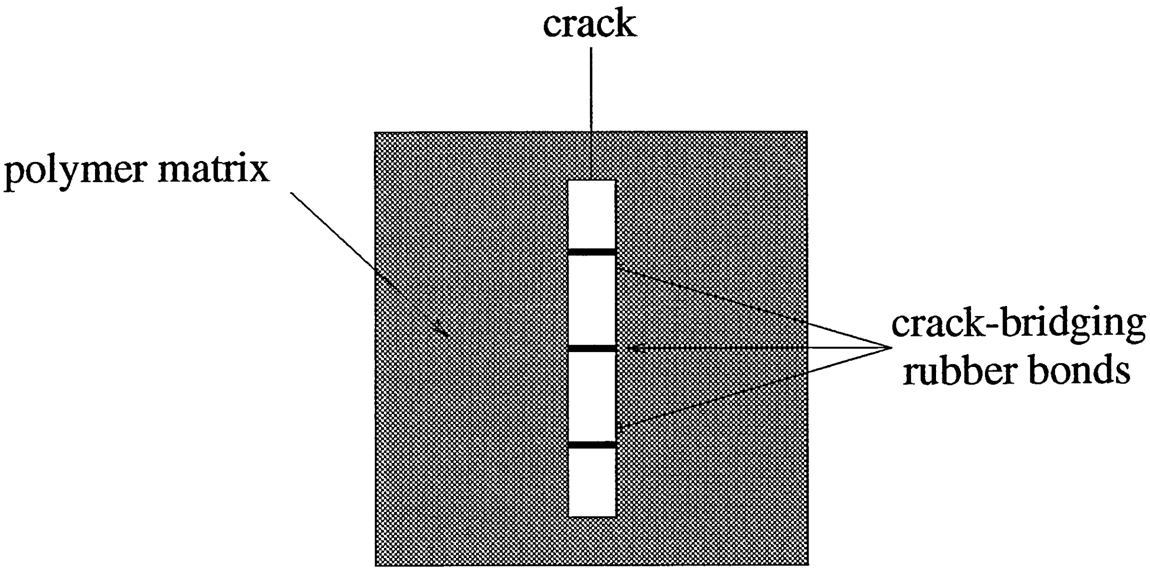

Figure 6.6: Crack-bridging in a bond lattice

ing effect (region **C**). The addition of more rubber does not improve the material toughness to the same extent as in region **B**. Beyond region **C**, further addition of rubber leads to the material's linear weakening (d decays linearly with Φ) (region **D**). In many real systems, region **D** is not accessible to experiments; for high rubber fractions (and, therefore, small polymer ones), the composite materials lose their polymeric nature. This weakening phenomenon could be a model artefact. Indeed, in this linear model, the failure damage of a pure rubber system ($\Phi = 100\%$) must be the same than the one of a pure polymeric system ($\Phi = 0\%$). Let p_{p_i} be the breaking probability of a given bond (i) in a pure polymeric system and p_{r_i} the breaking probability of the same bond (same location) in a pure rubber system. We then have :

$$p_{p_i} = \frac{e^{f_{p_i} - F_p}}{\sum_{j=1}^{n} e^{f_{p_j} - F_p}}$$

and

$$p_{r_i} = \frac{e^{f_{r_i} - F_r}}{\sum_{j=1}^{n} e^{f_{r_j} - F_r}}$$

where f_{p_i} and f_{r_i} are the forces sustained by bond i in each system. We then have :

$$p_{p_i} = \frac{e^{f_{p_i}}}{\sum_{j=1}^{n} e^{f_{p_j}}}$$

and

$$p_{r_i} = \frac{e^{f_{r_i}}}{\sum_{j=1}^{n} e^{f_{r_j}}}$$

In pure polymer and pure rubber systems, for a same damage configuration, the external applied force is distributed identically (the only difference would be in the bonds elongations, but in the same proportion for all of them). Therefore $\forall\ i,\ f_{p_i} = f_{r_i}$. Then, for pure systems, we have :

$$\forall\ i,\ \ p_{p_i} = p_{r_i} \tag{6.2}$$

The breaking probability of a bond in a one-component system differs from the others only by its location in the system and no longer by its different nature. Therefore, for this model, the damage is bound to decrease from its highest value (at the end of the saturation region **C**) to its original value for a pure polymeric system.

The four region splitting we observe in 3D systems is also observed for 2D systems as Fig. 6.7 shows for 70 × 70 systems ($F_r = 8$, $k_r = 0.1$). The damage data follow the same trend : embrittlement, toughening, saturation, weakening.

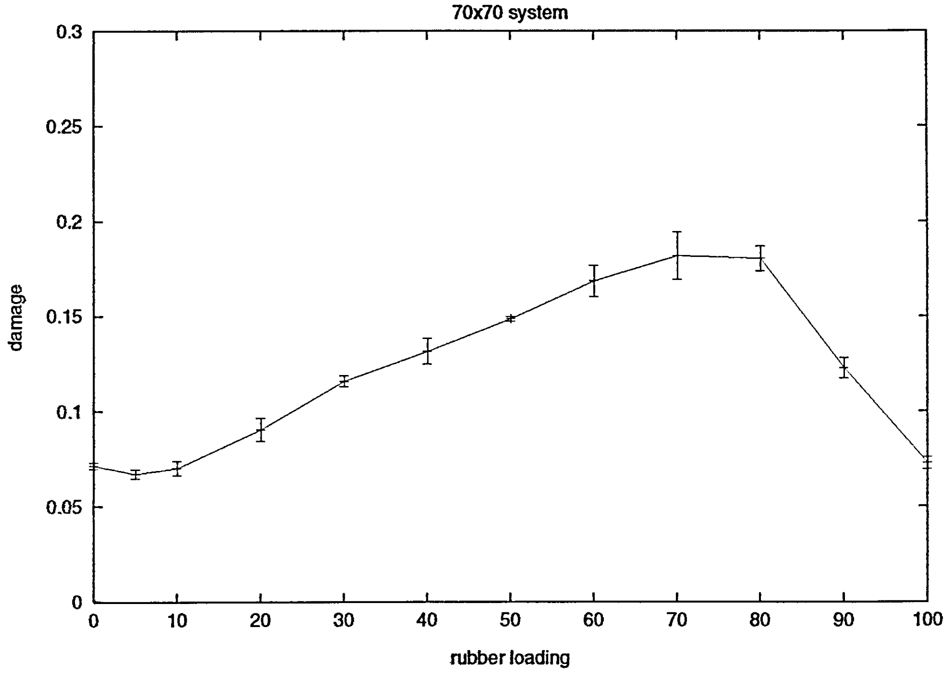

Figure 6.7: Damage in 70 × 70 systems

Effects of varying the value of k_r

For a given rubber force threshold F_r, changing the value of the rubber elastic coefficient k_r does not significantly alter the general trend of the damage results. Fig. 6.8 shows data obtained for various k_r for $F_r = 8$. Different observations can be made :

The embrittlement region **A**, which is important for the smallest values of k_r, tends to disappear when k_r is increased. In other words, the more flexible the rubber bonds, the more significant this embrittlement phenomenon. This is consistent with the above explanation for this region where the rubber bonds are seen as having the same effect as pre-damaged zones for low loadings. That is to say that, for rubber bonds with low modulus k_r, we might assume them to be close to $k_r = 0$ (*ie* broken bonds). Region **A** disappears completely for $k_r \geq 0.5$ or $k_r \geq \frac{k_p}{2}$ and from this value the rubber loading has little effect on the damage for $0 \geq \Phi \approx 25\%$.

The saturation region **C** seems also to be evident for small values of k_r only. When

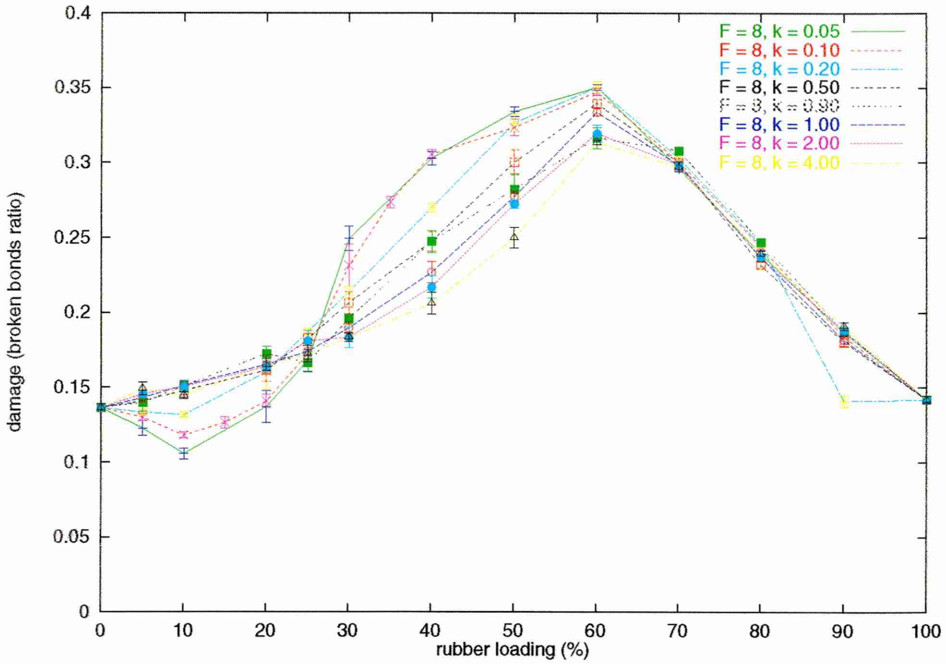

Figure 6.8: Damage in $20 \times 20 \times 20$ systems for $F_r = 8$ and different k_r

$k_r \geq 0.5$, the damage grows steadily up to its maximum value without levelling out. The maximum damage (hence toughness) achevied is also seen to be lower as k_r is increased. The presence of an embrittlement region seems to be associated with the presence of a plateau region : systems that do not exhibit the embrittlement region also do not have a plateau at higher rubber loadings.

This effect is also observed when the values of F_r is decreased, see Fig. 6.9 for $F_r = 2$ and Fig. 6.10 for $F_r = 4$. On the other hand, for $F_r = 16$, the saturation region is not observable irrespective of the value of k_r. This is clearly seen in Fig. 6.11 .

When F_r is large, the maximum damage value d_{max} is the same independent of the values of k_r. Decreasing F_r tends to increase the effect of k_r on this maximum. The smaller k_r is, the bigger d_{max} is found to be.

As a general rule, from all these damage data, two important rubber loading values can be observed at which the effects of k_r are negligible.

- The first one (Φ_α) marks the inversion of the rubber elastic coefficient effects.

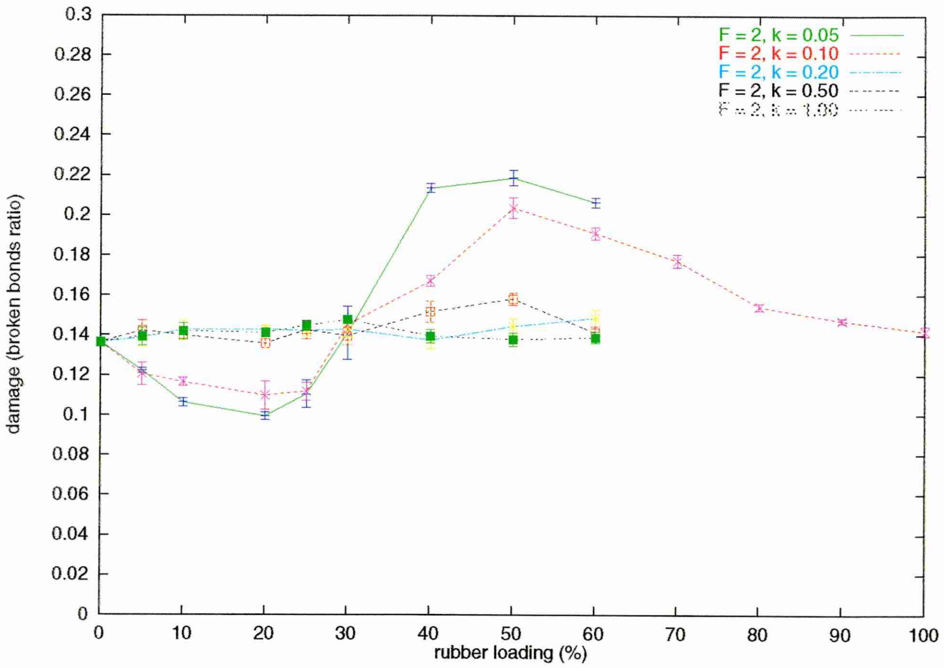

Figure 6.9: Damage in 20 × 20 × 20 systems for $F_r = 2$ and different k_r

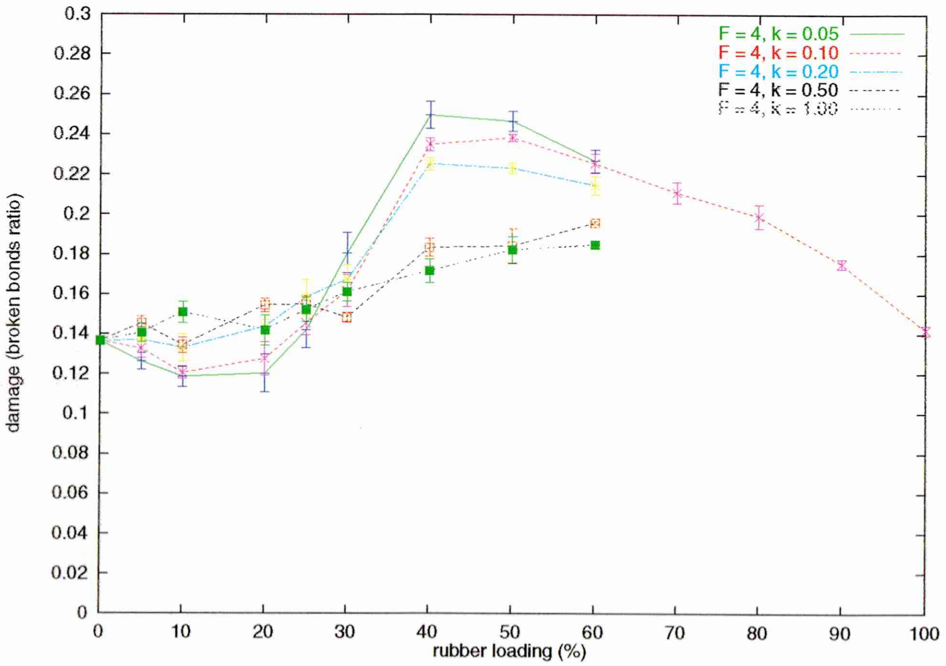

Figure 6.10: Damage in 20 × 20 × 20 systems for $F_r = 4$ and different k_r

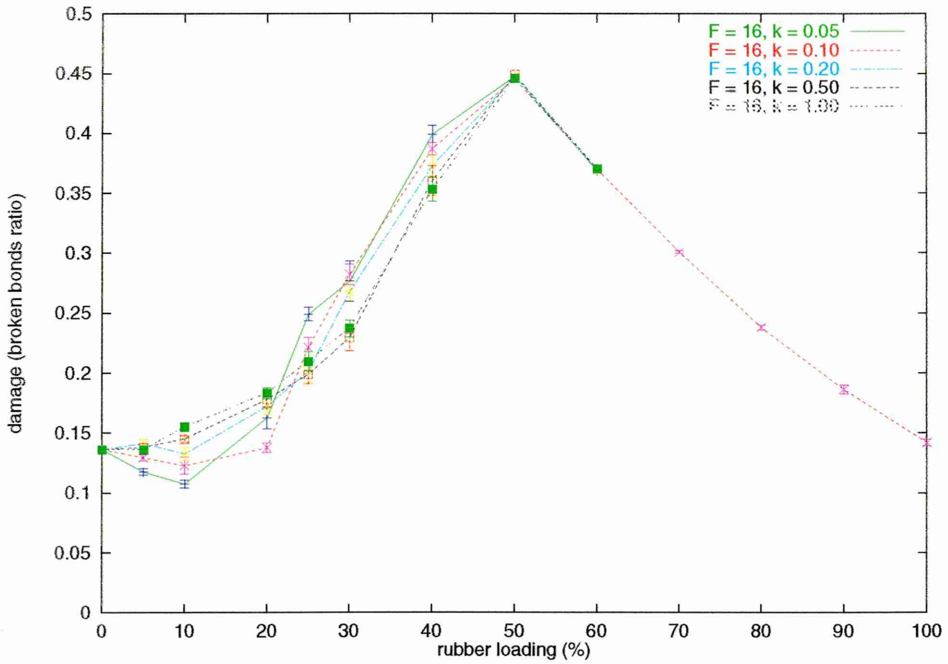

Figure 6.11: Damage in 20 × 20 × 20 systems for $F_r = 16$ and different k_r

Before Φ_α, the damage is greater for the larger values of k_r. Increasing the loading beyond this point sees the reverse situation where the damage is the largest for the smallest values of k_r, up to the point where we reach the second important value of Φ, Φ_β.

- When Φ approaches the value of Φ_β, the influence of k_r tends to disminish and is null when increasing the rubber loading above that point. The damage is then independent.of the elasticity of the rubber.

In Fig 6.3, these values are $\Phi_\alpha \approx 25\%$ and $60\% < \Phi_\beta < 70\%$.

To summarise, we have the following rubber loading effects on the damage :

- $\forall\ \Phi \in [0, \Phi_\alpha[\,, \qquad k_r^1 < k_r^2 \quad \Leftrightarrow \quad d\left(k_r^1, \Phi\right) < d\left(k_r^2, \Phi\right)$
- $\forall\ \Phi \in]\Phi_\alpha, \Phi_\beta[\,, \qquad k_r^1 < k_r^2 \quad \Leftrightarrow \quad d\left(k_r^1, \Phi\right) > d\left(k_r^2, \Phi\right)$
- $\forall\ \Phi \in \{\Phi_\alpha\} \cup [\Phi_\beta, 1]\,, \quad \forall\ k_r^1, k_r^2, \qquad d\left(k_r^1, \Phi\right) \approx d\left(k_r^2, \Phi\right)$

With this ascending order :

$$0 \leq \Phi_B(k_r, F_r) < \Phi_\alpha(F_r) < \Phi_C(k_r, F_r) \leq \Phi_D(k_r, F_r) \leq \Phi_\beta(F_r) < 1$$

where suffix B, C, D refers to the boundary between regions A, B, C in Fig 6.3.

As presented in following table, the value of Φ_α decreases slighly with increasing the mechanical strength of the rubber phase F_r.

F_r	2	4	8	16
Φ_α	30%	$\approx$ 27%	25%	$\approx$ 22%

Discussion on varying k_r

A stress distribution based interpretation of the inversion of the k_r effect occuring at Φ_α could be advanced as follows. For low rubber loadings ($\Phi < \Phi_\alpha$), rubber bonds are relatively isolated from each other and, to extend the embrittlement explanation, the more elastic they are, the higher the stress wiil be in the matrix in their vicinity. This makes it more likely for the surrounding polymer bonds to break, leading to a crack opening. We then have a less homogeneous stress distribution (and therefore a more brittle material) for the smallest values of k_r. The stress distribution becomes relatively more homogeneous on increasing k_r (the difference between the stress within the rubber vicinity polymeric zones and the stress within the other polymeric zones decreases when $k_r \rightarrow k_p$).

The effect of an inhomogenous stress distribution is to isolate certain zones within the material. When there are just a few of these zones, this can have the consequence of initiating crazes, and consequently, microcracks, without control. This is because rubber bonds are too far apart to be able to terminate the microcracks. As such, a single crack quickly dominates and energy dissipation becomes rather localised. However, when these craze intiation zones are numerous, the damage is distributed more evenly throughout the material and the dominance of a single main crack is delayed. Large distributed breaking of bonds throughout the system provides a much more efficient means of dissipating energy.

On the other hand, when the proportion of rubber bonds reaches a certain threshold (Φ_α), the effect of the rubber bonds changes. The rubber bonds can no longer be considered as isolated, on the contrary some may form rubber clusters, due to the decreasing inter-particle distance. The stress is therefore more evenly distributed between the rubber and polymer bonds. This stress distribution becomes even smoother when the rubber-polymer elastic coefficient difference is small (*ie* when $k_r \longrightarrow k_p$). In this situation, the increasingly homogeneous stress distribution has an undesirable effect; in the limit $k_r = k_p$, the stress context becomes identical to that within a pure polymer system (however the breaking process is still differentiated by the different force thresholds F_r and F_p). The system therefore tends to behave more like a pure polymeric one. However, if the stress distribution is kept locally inhomogeneous by having a low value k_r coefficient, the stress contrast between rubber vicinity and polymer matrix regions is preserved. This leads to a widespead distribution of damage, thus delaying the development of a main single crack.

To summarise, for a system with few rubber particles, the more homogeneous the stress distribution in the polymer matrix, the better suited it is to delaying the material failure. This stress distribution homogeneity increases as k_r is increased ($k_r \longrightarrow k_p$). On the other hand, when the rubber concentration become significant ($\Phi > \Phi_\alpha$), toughening improves when the stress distribution is inhomogeneous, favouring widespread damage.

The different damage trends can be sumarised by the following table :

	stress distribution	
	inhomogeneous	homogeneous
$\Phi < \Phi_\alpha$	$\searrow$	$\nearrow$
$\Phi > \Phi_\alpha$	$\nearrow$	$\searrow$

The arrows indicating a relative toughness decrease ($\searrow$) or increase ($\nearrow$) for an identical value of Φ.

For high values of the rubber loading ($\Phi \geq \Phi_\beta$), we observe a common damage behaviour for all systems, independent of the values of k_r. In this case, the behaviour of the systems are dominated by the rubber bonds; this domination occurs because the polymer bonds break in the first stages of the breaking process (see next chapter). For the remainder of each simulation, therefore, the system tends to behave like a single component material, whose damage, in this hookean-bond model, is elastic constant independent (*cf* Eq. 6.2).

Effects of varying the rubber mechanical strength F_r

For a given rubber elastic coefficient k_r, we can alternatively observe the effects of changing the value F_r on the damage d. To this end, we present damage data for F_r values of $1, 2, 4, 8$ and 16 (Figs 6.12, 6.13, 6.14, 6.15, 6.16).

As a general rule, from these figures, we observe that the damage d grows with F_r. It must be noticed that this effect takes place only for values of Φ above a certain value Φ_γ. Before this value, the damage appears to be independent of F_r; futhermore, this value seems to be k_r-independent since, for all k_r values, we have $\Phi_\gamma \approx 10\%$. One can notice that when $\Phi < \Phi_\gamma$, not only is the damage the same for all F_r but also that it does not increase with Φ. It even decreases for the most rubbery systems ($k_r = 0.05$ and 0.1).

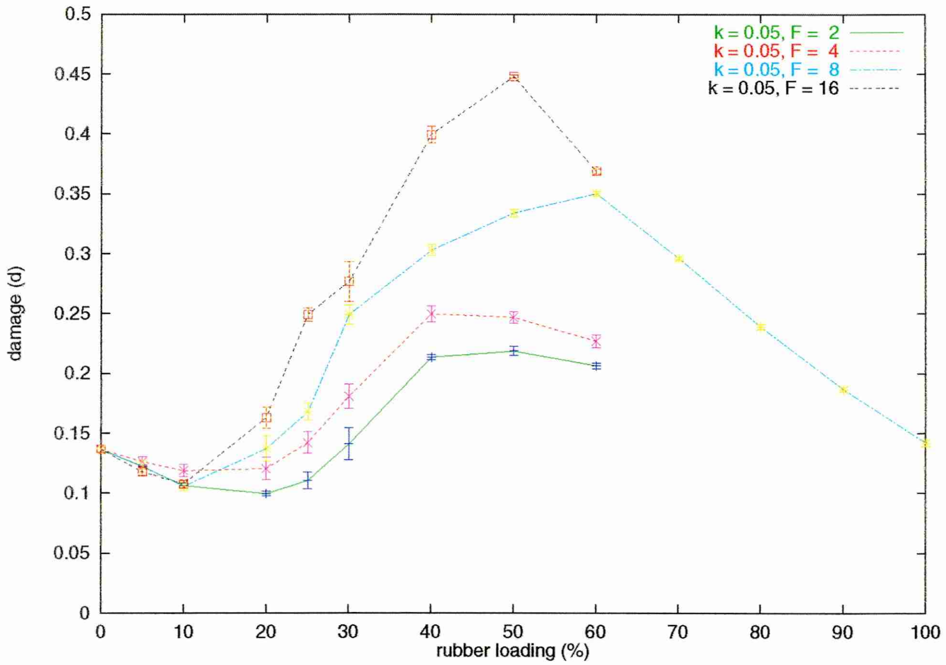

Figure 6.12: Damage in $20 \times 20 \times 20$ systems for $k_r = 0.05$ and different F_r

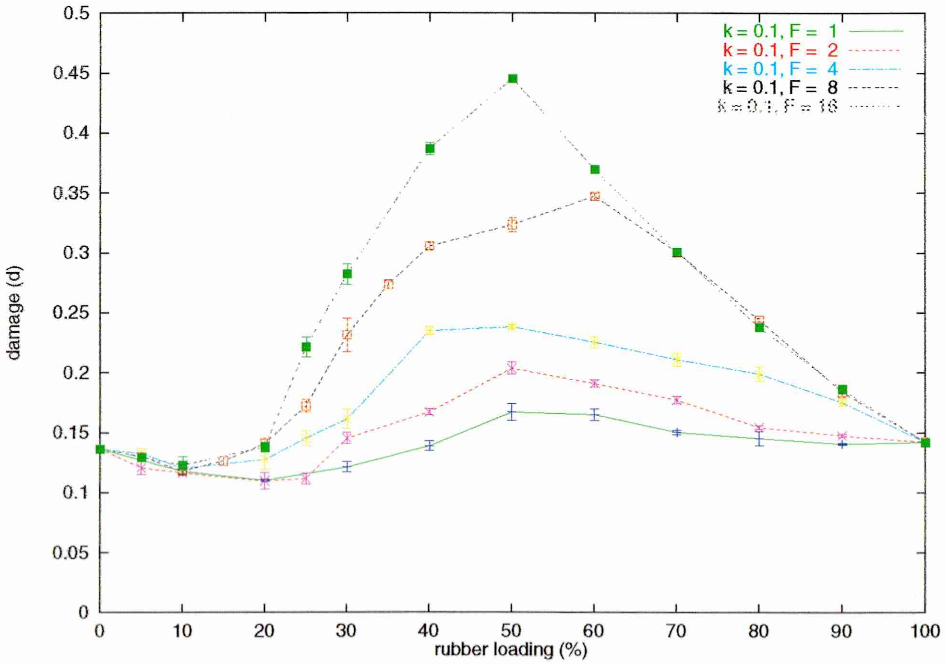

Figure 6.13: Damage in $20 \times 20 \times 20$ systems for $k_r = 0.1$ and different F_r

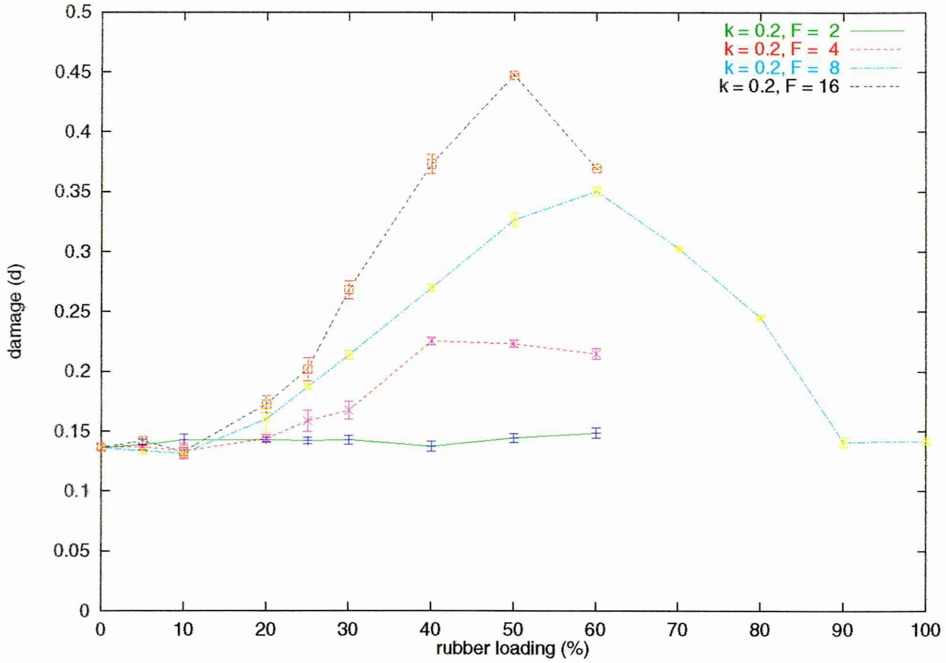

Figure 6.14: Damage in 20 × 20 × 20 systems for $k_r = 0.2$ and different F_r

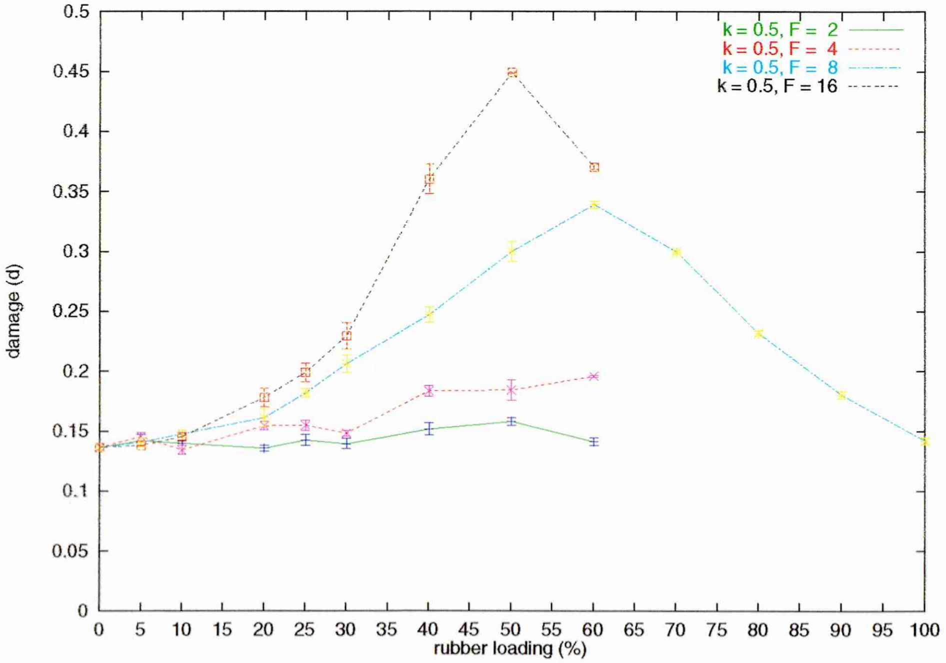

Figure 6.15: Damage in 20 × 20 × 20 systems for $k_r = 0.5$ and different F_r

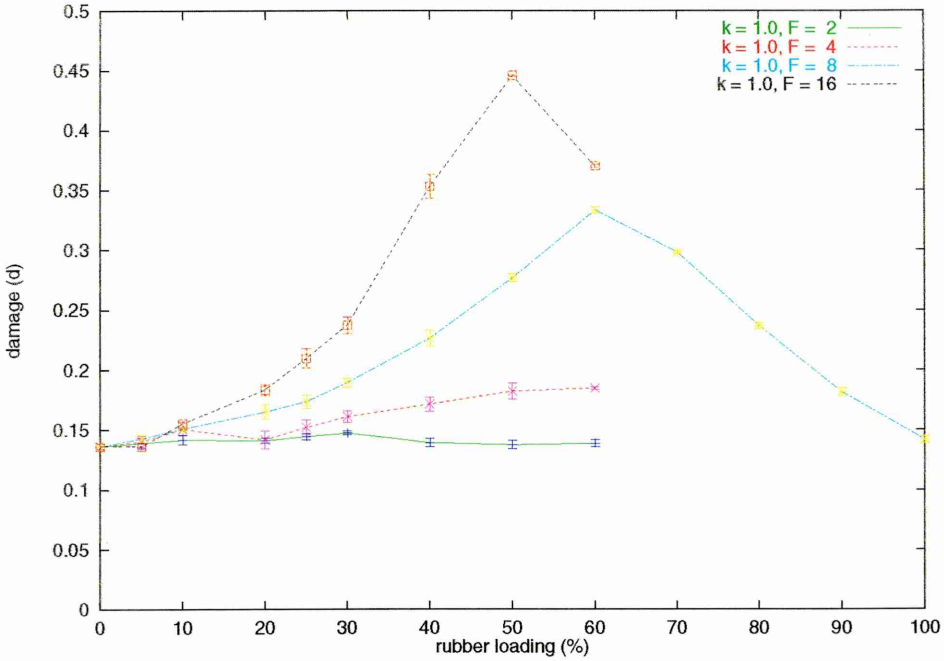

Figure 6.16: Damage in $20 \times 20 \times 20$ systems for $k_r = 1.0$ and different F_r

The mechanical strength of the rubber bonds becomes important when these bonds start to experience high stress. This situation appears when crack-bridging (as illustrated in Fig 6.6) occurs in a system. Indeed, the greater F_r, the more stress the rubber bonds can sustain before breaking. The trend observed in the previous figures suggests that at sufficient rubber loading ($\Phi > \Phi_\gamma$) crack-bridging by rubber bonds is significant since the system's overall damage (hence toughness) is increasing. It also shows that, for low rubber loadings ($\Phi < \Phi_\gamma$), since no toughening is observed, rubber-bridging is of minor importance.

6.3 Crack complexity

A common way to measure the degree of irregularity or complexity of an object is to determine its *fractal dimension* D [79]. The crack complexity of 2D materials' [59] or electrical networks' breakdown has been measured in this way. If an object is covered with n regular cells of size r, this object has a fractal structure if there exists a value D (the object's fractal dimension) such that the following relation holds whatever the value of r :

$$n \sim r^{-D}$$

We have applied this method to characterise the main crack's complexity arising from our 2D and 3D simulations. Because of the square lattice structure of our systems, the covering cells are squares of side r in 2D and cubes of side r in 3D.

As shown in Fig. 6.17 for 2D systems, $\log n$ seems to scale linearly with $\log r$, for both rubber loading $\Phi = 20\%$ and $\Phi = 40\%$, indicating that the 2D cracks have a fractal structure. Nevertheless, the fractal dimensions of these two cracks are both very close to 1 ($D \approx 1.06$ for $\Phi = 20\%$, and $D \approx 1.07$ for $\Phi = 40\%$) which indicates a fairly straight crack line.

For 3D systems, from Fig. 6.18 we can see that the data give a poor fit to the required form. Even though a sensible value of D can be worked out from these plots ($D \approx 2.32$ for $\Phi = 20\%$, and $D \approx 2.37$ for $\Phi = 40\%$), the quality of the fits obtained indicates that the cracks do not have a fractal nature. Applying the fractal dimension concept to them is, therefore, inappropriate.

To summarise, the notion of fractal dimension does not seem appropriate to typify the main crack irregularity in our case : (i) 2D systems give rise to main cracks with straight outlines and the fractal dimension method does not differentiate them significantly from each other. (ii) 3D cracks do not have a fractal nature (this is due to the lack of self-similarity exhibited by the main crack surfaces).

Therefore an alternative measure is required to characterise the geometry of these main cracks. A simple way is to measure their relative sizes. The crack relative size being dimension-dependent, we define, for 2D systems, a *relative crack length* L and

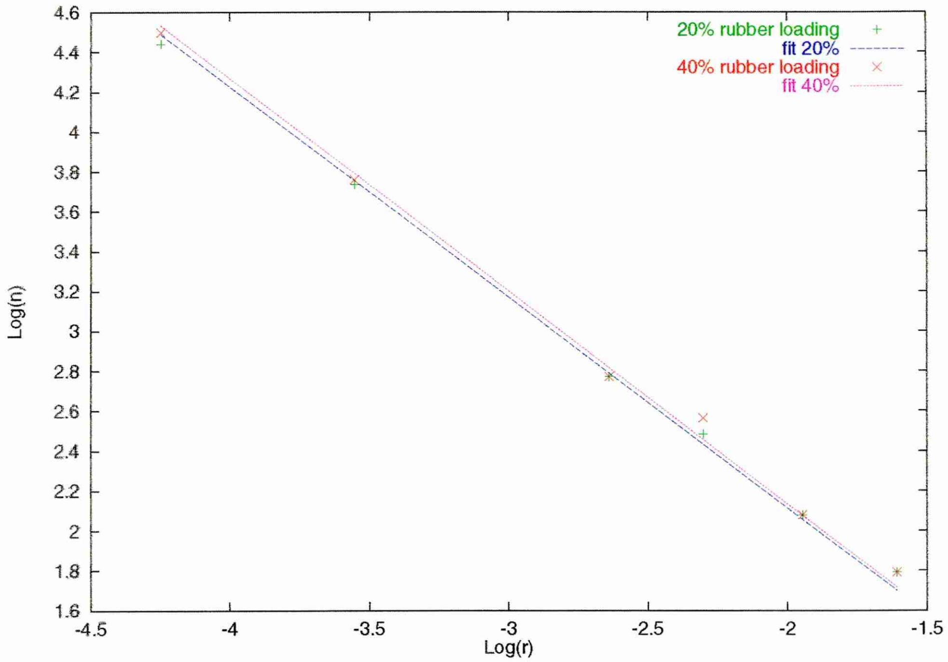

Figure 6.17: Log-log dependence of n on r for 2D systems (70 × 70)

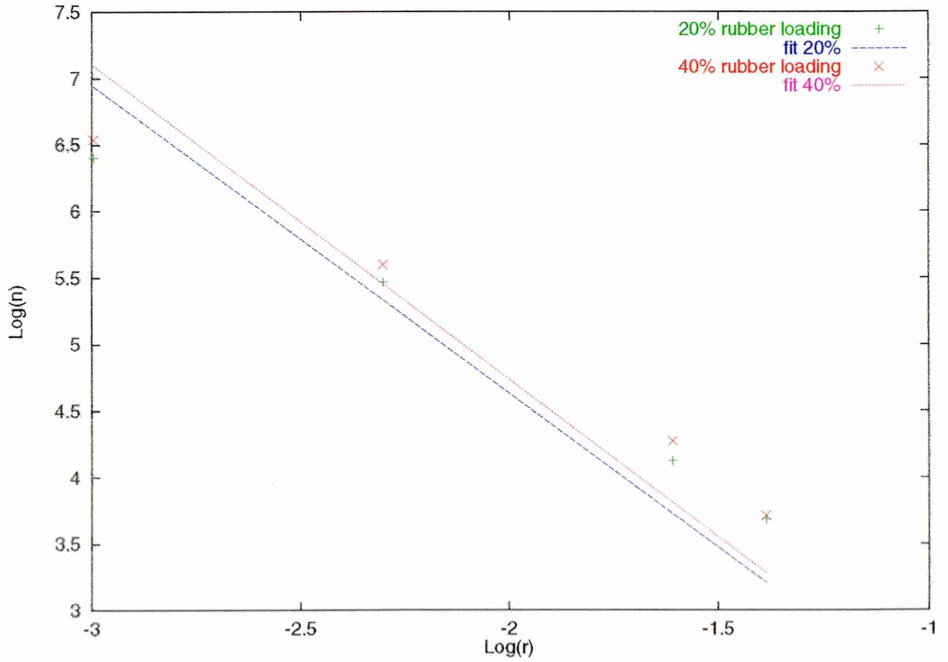

Figure 6.18: Log-log dependence of n on r for 3D systems (20 × 20 × 20)

for 3D systems, a *relative crack surface* S :

$$L = \frac{N_m}{N_y}$$

and

$$S = \frac{N_m}{N_y N_z}$$

Where N_m is the number of main crack's (broken) bonds, N_y and N_z are the system sizes along the axis y and z respectively (Ny is then the length of the system's stretched sides and $N_y N_z$ the surface of the system's stretched planes). A value close to 1.0 for L or S will indicate a crack which is straight and almost parallel to the side or face of the system.

The study of the main crack complexity has therefore been carried out using the relative crack length and surface.

6.3.1 System size dependence

For 2D systems, the system size dependence of the relative crack length for $\Phi = 20\%$ and $\Phi = 40\%$ rubber loadings as presented in Fig. 6.19 ($k_r = 0.1$ and $F_r = 8$) does not seem as obvious as did that for the relative damage(*cf* Fig. 6.1). The fluctuations here are quite significant, as indicated by the relatively large error bars. For systems with $\Phi = 20\%$, within error bars, one can observe that the relative crack length lies between $L \approx 1.15$ and $L \approx 1.3$, except for the 120 × 120 systems whose value is $L \approx 1.38$.

For systems with $\Phi = 40\%$, within the error bars the relative crack length is seen to lie between $L \approx 1.25$ and $L \approx 1.3$, except for the 100 × 100 systems whose value is $L \approx 1.45$.

The system size dependence of the relative crack surface S for 3D systems appears

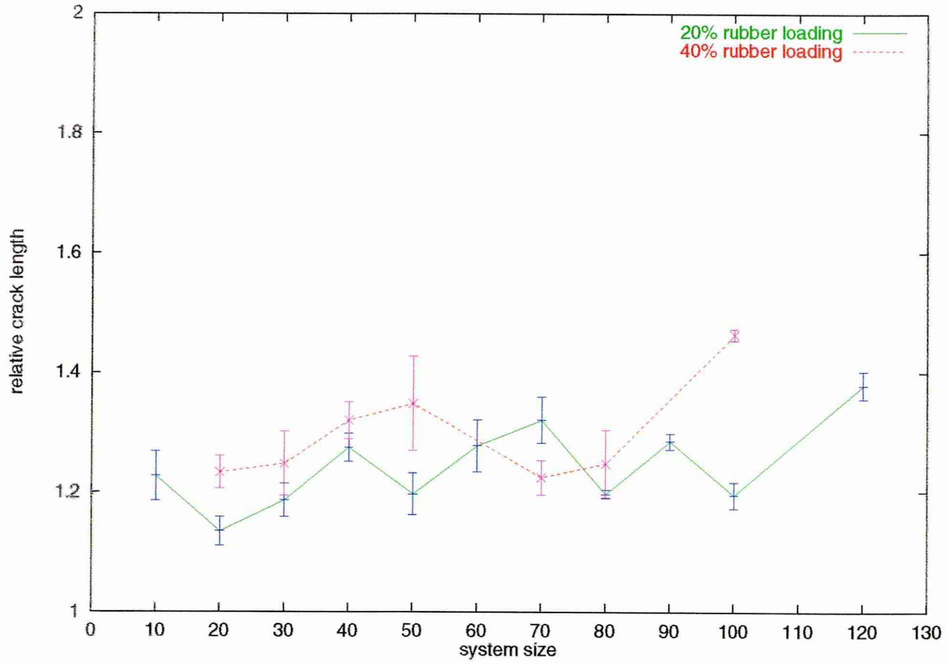

Figure 6.19: System size dependence of the relative crack length in 2D sytems

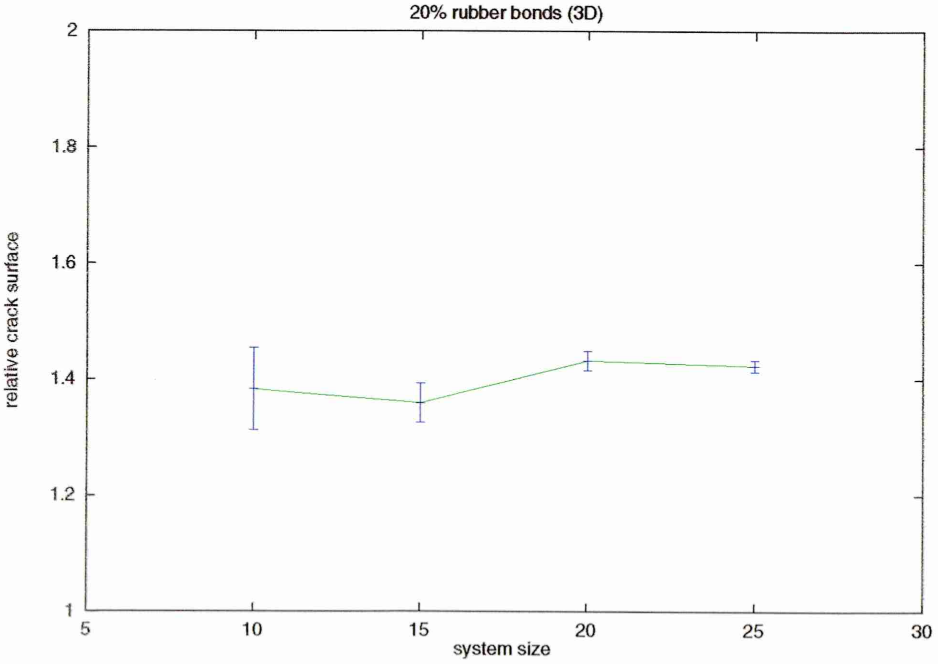

Figure 6.20: System size dependence of the relative crack surface in 3D sytems

to be better behaved than that of 2D systems (*cf* Fig. 6.20), but still a significant dispersion is observed here as well.

For both figures, each data point has been averaged over at least 5 systems. The relatively large error bars found for each system size can be explained by the fact that, for a given system, contrary to the damage, the crack surface does not depend only on the rubber loading Φ, but also on the spatial distribution of the different kinds of bonds in the system. Therefore the crack path, which tries to find its way connecting the rubber bonds, can be very different for different systems which are identical in terms of their size and rubber loading. Much larger data sets would be required to fully characterise the dependence of crack surface on system size.

6.3.2 Rubber loading effects

The relative crack surface results shown in Fig 6.21 and Fig 6.22 exhibit a quite good correlation with the damage ones as presented in Fig 6.8 and Fig 6.13 respectively. The same four regions can be distinguished. The crack complexity data seem then to be consistent with the damage data; the more damaged a system is the more complex the main crack appears to be. Nevertheless, it can be observed that the crack complexity data show larger sample to sample fluctuations, the errors bars are considerably larger than those of the damage data.

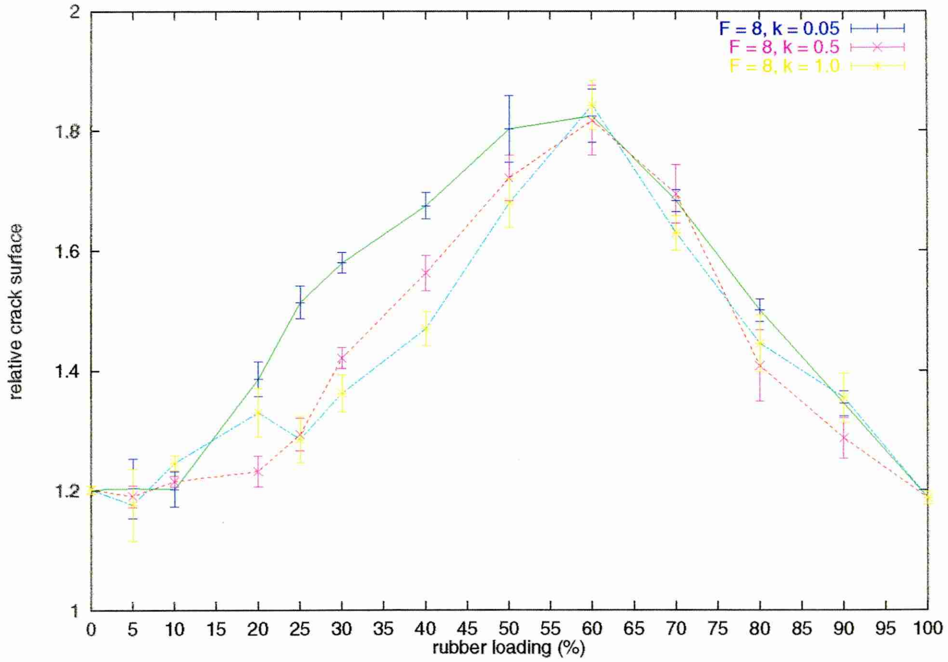

Figure 6.21: Relative crack length in 3D systems for $F_r = 8$ and different k_r

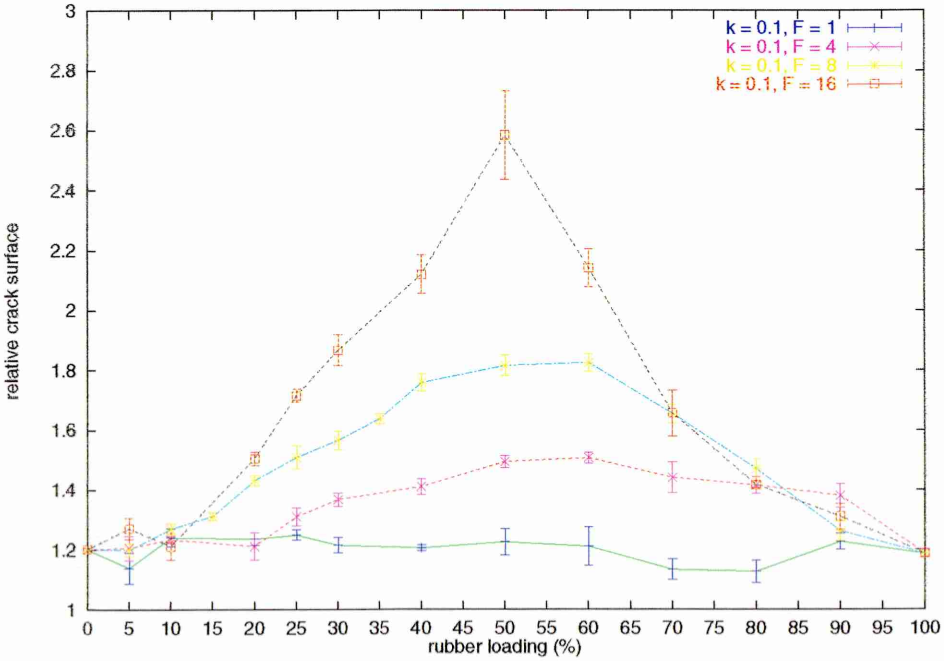

Figure 6.22: Relative crack length in 3D systems for $k_r = 0.1$ and different F_r

6.4 Effects of clustering of rubber particles

6.4.1 Introduction

The previous damage results relate to systems with randomly distributed rubber bonds. In real rubber modified materials, the distribution of rubber particles is unlikely to be entierely random; particles tend to aggregate due to the interaction between them and hence form clusters. In order to reproduce such situations, simulations have been carried out with inhomogeneous rubber distribution in 2D systems. The chosen rubber distribution is a 2D normal distribution around a "hot spot" (a site of higher rubber concentration). The systems hold two diametrically opposed hot spots as shown in Fig 6.23. The probability p of a bond to be rubber at a distance r from a hot spot is :

$$p \propto e^{-\frac{r^2}{w^2}}$$

where w is the width of the normal distribution. Therefore, with two hot spots, the probability p of a bond to be rubber at a distance r_1 from the first hot spot and r_2 from the second is :

$$p \propto e^{-\frac{r_1^2}{w^2}} + e^{-\frac{r_2^2}{w^2}}$$

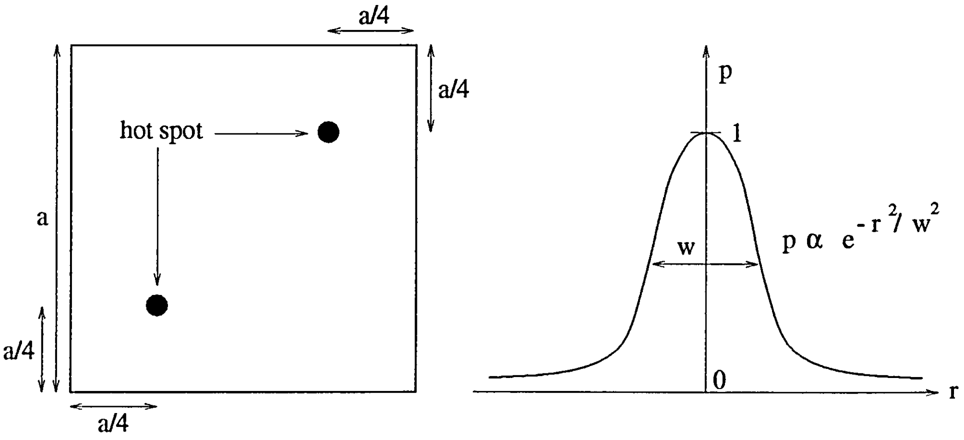

Figure 6.23: System involving two hot spots (left) and rubber bond distribution around an isolated hot spot (right)

6.4.2 Results

Fig 6.24 presents the effect of the distribution width on the damage for 70 × 70 systems with $k_r = 0.1$ and $F_r = 8$; each data point has been averaged over at least 4 simulation results. It clearly appears that the more homogeneous the rubber distribution is, the more damage the system can sustain before failing. When the width is broad enough, the same trend as for a homegeneous distribution is observed : embrittlement for low rubber concentrations, rubber toughening and toughening saturation as the rubber proportion is increased. But when the rubber distribution becomes very concentrated around the hot spots ($w \leq 30$), the toughening phenomenon seems to disappear quickly. For highly concentrated distributions there is no toughening any more but one just can observe a material weakening for all rubber concentrations.

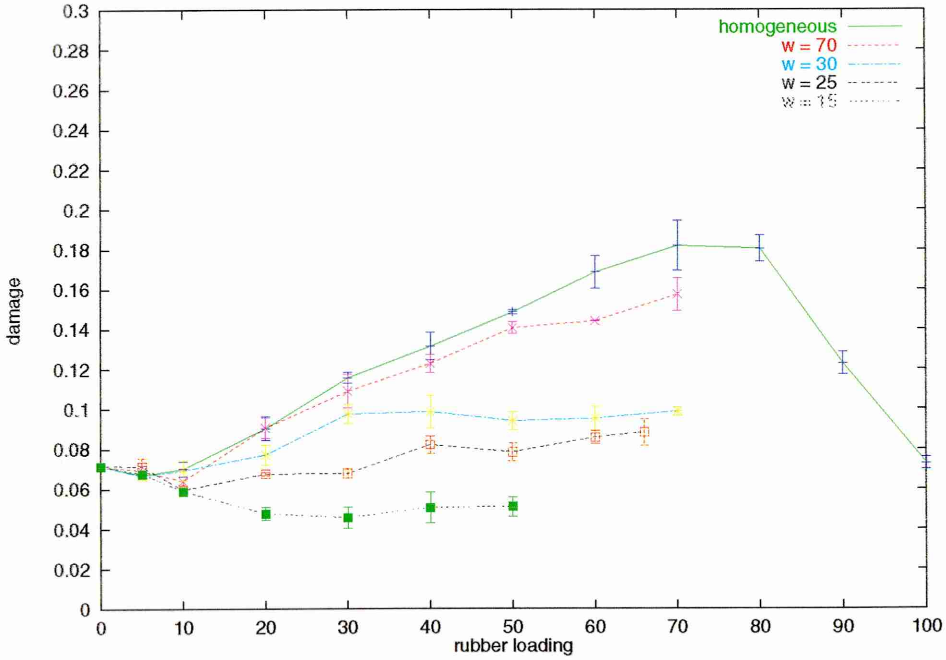

Figure 6.24: Damage in 2 hot spot systems for different distribution widths

Fig 6.25 presents the damage in 2 systems containing 20% of rubber bonds ($k_r = 0.1$, $F_r = 8$) with different rubber distributions. When rubber bonds are well-distributed ($w = 70$), the damage is also well-distributed (view *a.1*) and the main crack has to find its way through rubber-populated regions (view *a.2*). When the rubber distribution is less homogeneous ($w = 15$), the damage appears to be more localised (view *b.1*) to rubber-free regions. Polymer bonds within the rubber clusters are protected and only few of them break. On the other hand, the almost rubber-free regions, which can be considered as low rubber loading sub-systems, experience rapid crack propagation, and, eventually, their cracks joins to form a main crack (view *b.2*). It is therefore concluded that any aggregation or clustering of the rubber particles would decrease the material toughness.

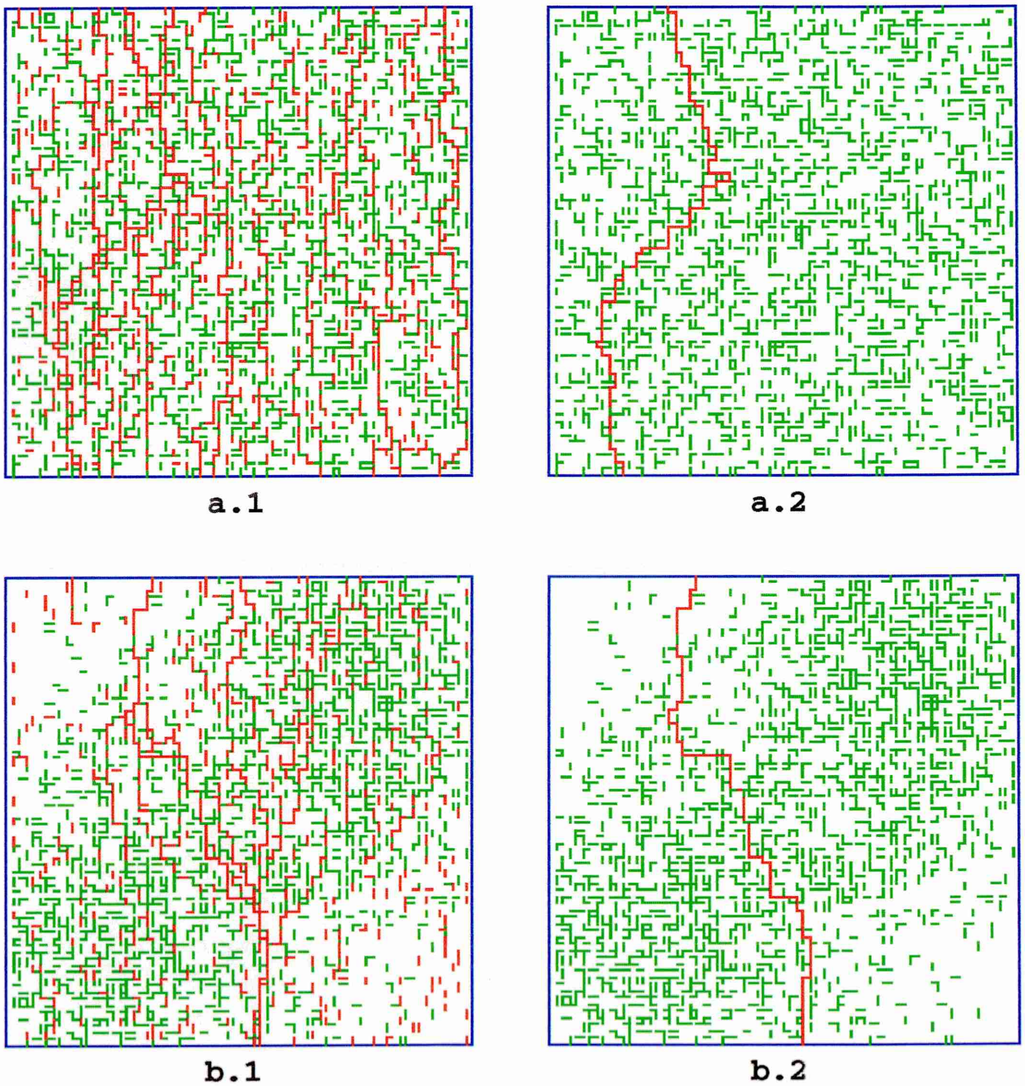

a.1 **a.2**

b.1 **b.2**

Figure 6.25: Damage in 2 hot spot 70 × 70 systems (broken polymer bonds are in red, all the rubber bonds are represented, in green) : a.1) $w = 70$, full damage; a.2) $w = 70$, main crack; b.1) $w = 15$, full damage; b.2) $w = 15$, main crack.

6.5 Relation to real materials

6.5.1 Introduction

We now compare the damage results given by this model to the relevant experimental data on real rubber-toughened materials. It must be repeated here that the damage parameter d we have adopted in this work (relative number of broken bonds), as an indicator of the material's toughness, is a crude measure of the energy dissipated during the failure process. Nevertheless, since the impact-toughness of a material is directly related to its ability to absorb the impact energy, the variation of this parameter's magnitude gives a good indication of the trend of the material's impact-resistance. Experimentally, this materials property is measured in different manners : notched Izod impact strength or toughness, strain at break, fracture energy , Charpy impact energy, etc. In this work we have presented the rubber concentration Φ in terms of volume (or number) fraction; in the experimental work, this parameter is frequently presented in terms of weight fraction (wt %).

Experimental data are presented in section 2.4. We focus here on the rubber loading effects on damage, which are illustrated by the following figures : 2.8,2.9, 2.10 and 2.11. At first sight, these experimental results seem to exhibit similar regions to those in the current study.

6.5.2 Damage regions

The model results have permitted the identification of a specific region (**A**) for low rubber loadings which does not present important rubber-toughening and which, for low values of the rubber elastic coefficient k_r, even exhibits an embrittlement effect. Experimental data do not clearly reveal such a weakening effect, but, generally show poor or no toughening for the lowest rubber concentrations. It should be noted that the experimental data, refered to here, do not concentrate on very low rubber concentrations ($\Phi < 5\%$) or on rubber elasticity variation. Nonetheless, this weakening phenomenon has been observed in acrylic-based systems [80], although it is still a matter of discussion.

The rubber-toughening region **B** is clearly observable from the experimental data and, as for the model results, it is characterised by a sharp toughness increase at its onset, in all the presented figures, and a leveling off tendency towards its end, when data are available (Fig 2.10 and 2.11).

When data are available, it appears clearly that the material's toughness tends to saturate after a certain rubber concentration, as shown by the model results (region C).

This weakening region, identified by the model results might, as we have previously pointed out, be a model artefact. Nevertheless, this sharp decrease in the material toughness with increase in rubber concentration at very high fractions is suported by experimental data for PMMA blends (Fig 2.10).

6.5.3 Conclusion

The overall evolution of the damage results and the rubber loading effects, as predicted by our model, are consistent with the available experimental data for a range of polymeric systems. There are, unfortunately, no available experimental results investigating the effects on the material's toughness of the change of rubber component's mechanical characteristics (k_r or F_r) to compare with the relevant model results.

Chapter 7

Stress results

In this chapter we present the results of the stress distribution obtained mainly from 3D simulations. We studied a $20 \times 20 \times 20$ system for different values of the parameters Φ, k_r and F_r. This system size has been chosen because it does not present finite size effects. The results are divided into three sections : the way in which the system's *maximum stress* evolves during the damage history (from undamaged system to material failure); the *global results*, which concern the evolution of stress related parameters of the system (such as the stress distribution, the average stress, the stress standard deviation, the material's overall elastic modulus, etc.); and the results which concern certain *significant bonds* (such as the most stressed bond, its nature and direction, etc.).

7.1 Maximum stress evolution

The results presented in this section concern the evolution of the stress sustained by the most stressed bond in the lattice at each step in the breaking process. The general trend of the maximum stress evolution is shown in Fig 7.1 for $\Phi = 40\%$, $k_r = 0.1$ and $F_r = 8$, as an example.

The stress goes through four regimes as the main crack develops :

A : Steady increase, non noisy regime

B : Noisy regime

C : New steady increase, non noisy regime

D : Failure regime

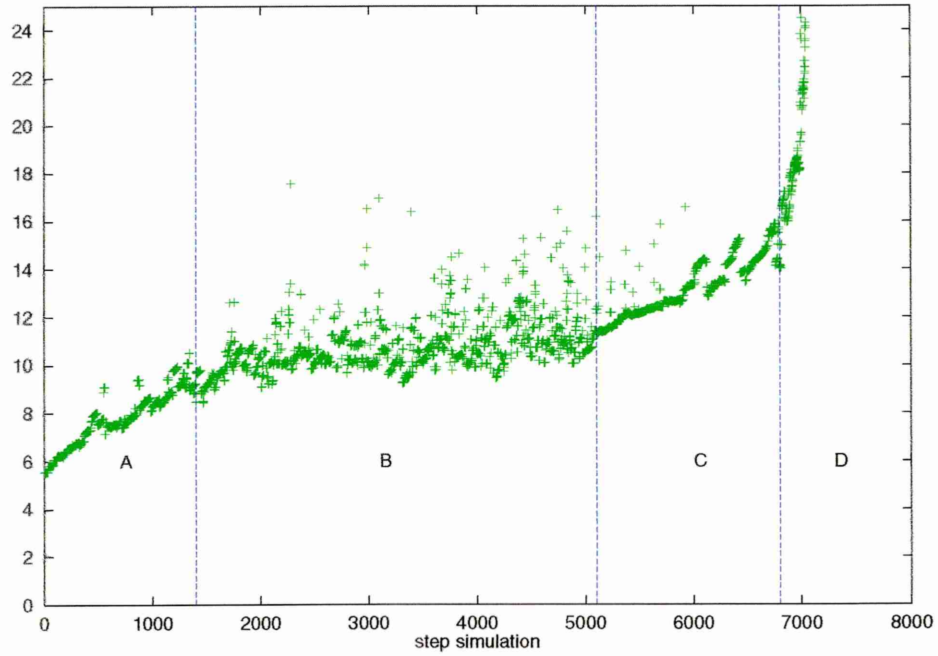

Figure 7.1: General trend of the maximum stress in $20 \times 20 \times 20$ systems ($\Phi = 40\%$)

At the early stage of the breaking process, when the damage is still low, the stress builds up steadily within the system. This regime (**A**) is characterised by a linear stress increase.

As the damage increases, the stress evolution suddenly becomes more chaotic. In this regime, the location of the maximum stress bond jumps erratically from one point to another throughout the whole system. The overall evolution of the maximum stress seems to level off through out this noisy regime (**B**), though.

The system then enters a new stage where the stress builds up steadily again (regime **C**). The maximum stress evolution appears to become less noisy again as in regime **A**.

When the remaining bonds are no longer capable of sustaining the applied stress, the system enters a failure regime (**D**). This is a short, catastrophic regime during which the damage is very localised and the maximum stress soars up to its highest value.

7.1.1 Rubber loading effects

The effects of the rubber loading Φ on the maximum stress evolution is shown in Fig 7.2 ($k_r = 0.1$, $F_r = 8$). These results represent the typical trends observed in all the simulations performed. The four different stress regimes identified earlier are altered by changing the rubber concentration. For very low Φ, regime **C** is very short or not apparent at all, but becomes more significant as the rubber loading is increased. It becomes dominant for very high values of Φ. On the other hand, regime **A**, the other smooth stress regime, sees its length decreases with increased rubber concentration. It evolves from a dominant role for low Φ values to a minor one for high rubber concentrations. The noisy regime **B** is short for low rubber loading values and steadily grows in length as the rubber concentration is increased. This growth seems to stabilise as Φ reaches $40\% - 50\%$. From this point it starts to shrink as Φ is increased further, eventually becoming negligible again for very high Φ values. This evolution is illustrated in Fig 7.3. It must be pointed out that this figure presents only a rough trend as the onset and the end of regime **B** are often blured with the limits of the side regimes **A** and **C**; regime **B**'s limits are therefore difficult to identify precisely.

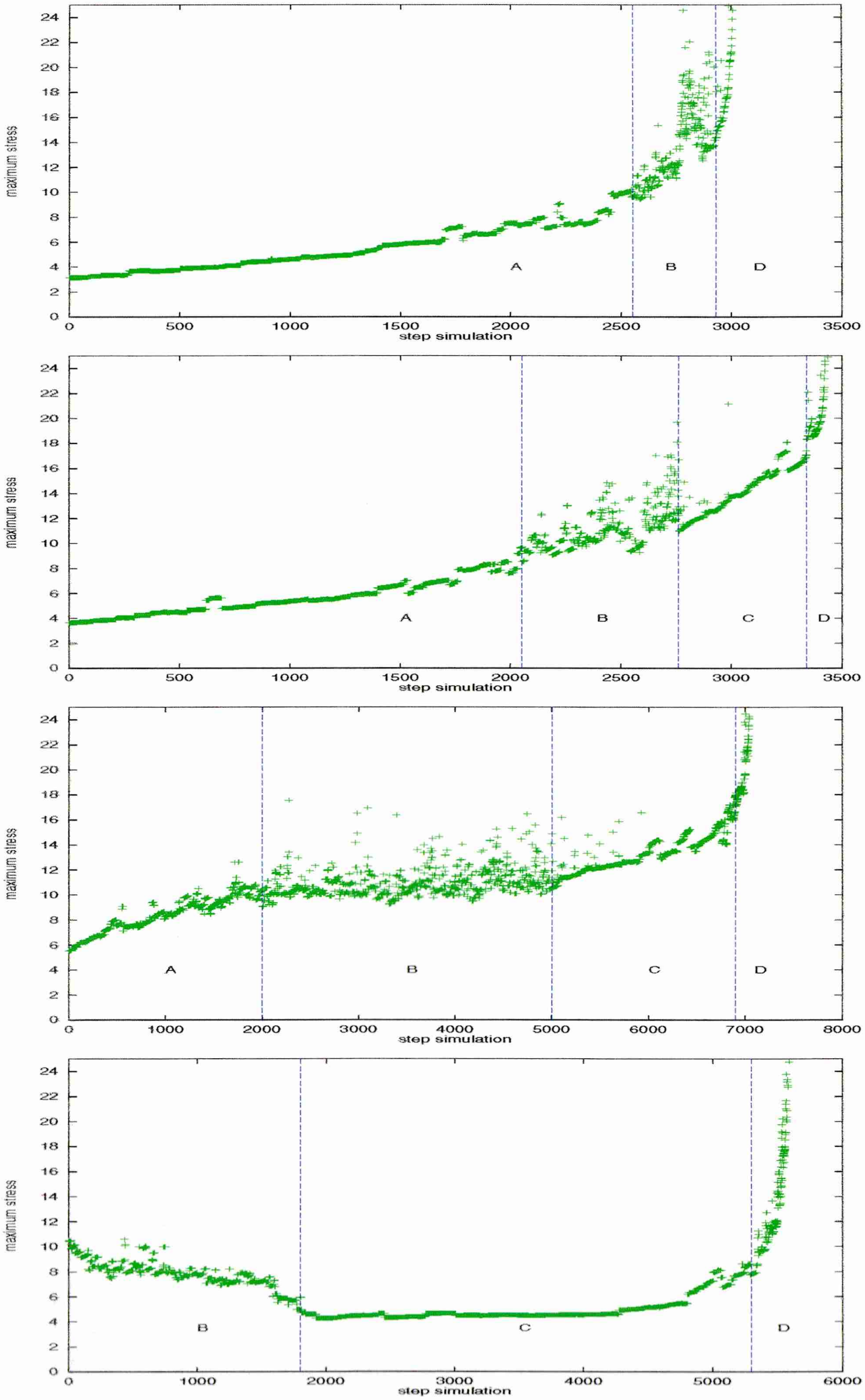

Figure 7.2: Rubber loading Φ effects on the maximum stress evolution. From top to bottom : $\Phi = 10\%, 20\%, 40\%, 80\%$ ($k_r = 0.1$, $F_r = 8$)

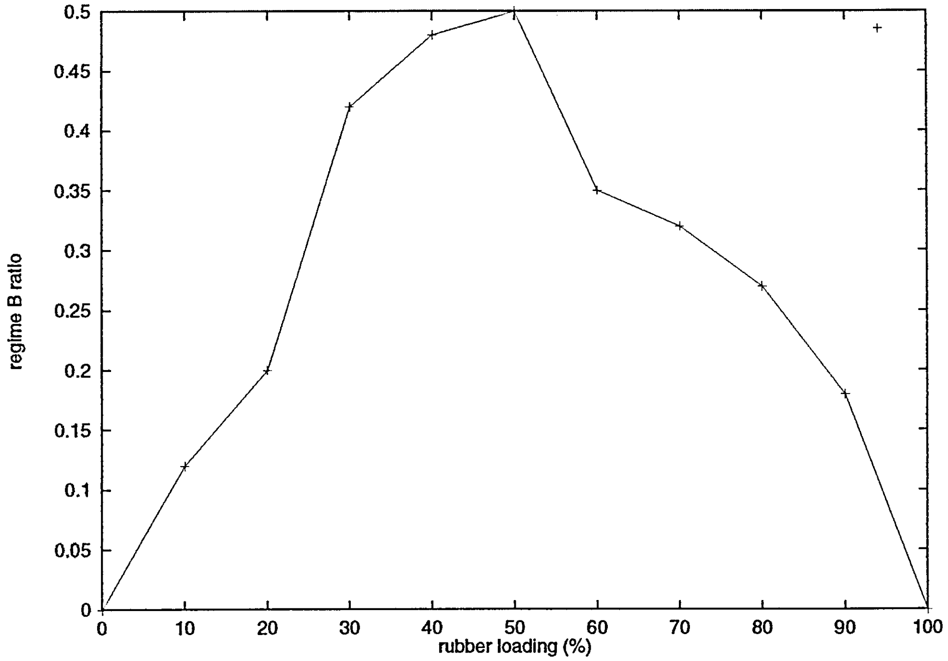

Figure 7.3: Variation with the rubber loading of the relative length of the noisy regime **B**

Varying k_r

Fig 7.4 shows the effects of the rubber coefficient k_r on the maximum stress evolution. As k_r is increased, on can notice an extension of regime **A** with a shortening of regime **B**. Regime **C** seems quite insensitive to changing k_r. Low values of k_r seem to favour the erratic stress behaviour of the system as observed in regime **B**.

Varying F_r

Fig 7.5 shows the effects of the rubber force threshold F_r on the maximum stress evolution. Regimes **A** and **B** do not seem to change much with varying F_r. The only noticable difference is the expanding of regime **C** as F_r is increased.

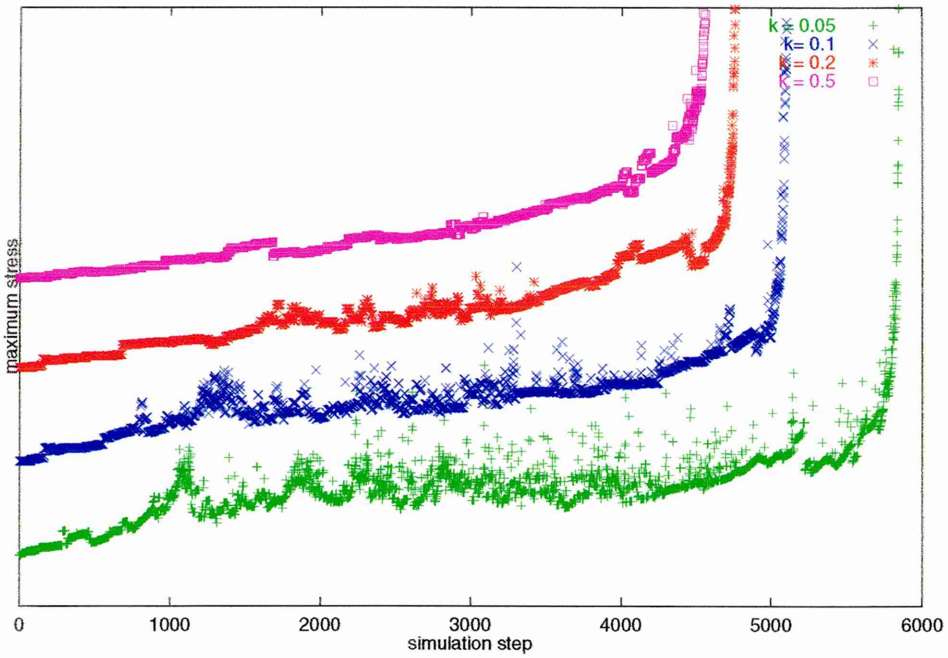

Figure 7.4: k_r-dependence of the maximum stress evolution ($\Phi = 30\%, F_r = 8$). Successive curves are shifted along ordinate axis for comparison purpose

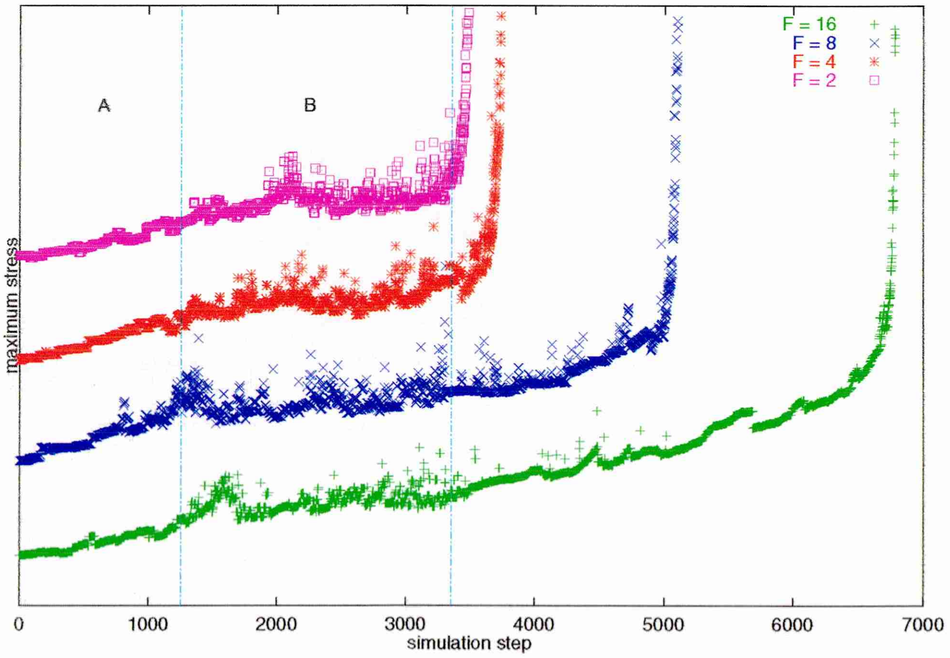

Figure 7.5: F_r-dependence of the maximum stress evolution ($\Phi = 30\%, k_r = 0.1$). Successive curves are shifted along ordinate axis for comparison purpose

7.2 Global results

7.2.1 Stress distribution

The stress distribution in a 20 × 20 × 20 system has been studied at various rubber loadings for both bond natures, rubber and polymer. The results presented in this section have been obtained with rubber parameters $k_r = 0.1$ and $F_r = 8$. Once again, this values are used to examplify the general trends.

Low rubber loadings

Fig 7.6 presents the evolution of the polymer bonds' stress distribution during the breaking process for a rubber loading of $\Phi = 10\%$. ($k_r = 0.1$, $F_r = 8$). The stress histogram tends to change from a very narrow distribution to a more widespread one as the damage progresses. In comparison, as shown in Fig 7.7, the rubber distribution does not change much throughout the simulation. In this case, the distribution remains fairly well-concentrated around a relatively constant average value.

Moderate rubber loadings

Increasing the rubber loading does not drastically change the trend of the evolution of the polymer stress distribution, as can be observed in Fig 7.8 for a rubber loading of $\Phi = 40\%$. Although the distribution is wider for this higher rubber concentration, its time evolution does not exhibit any significant pattern variation. For the rubber bonds, however, the observed stress distribution shows a very different evolution pattern from that observed for lower rubber loadings. From Fig 7.9, one can observe a splitting of the stress distribution into two distinct peaks as the breaking process proceeds on (visible at step #3000). As the simulation is carried further, the second

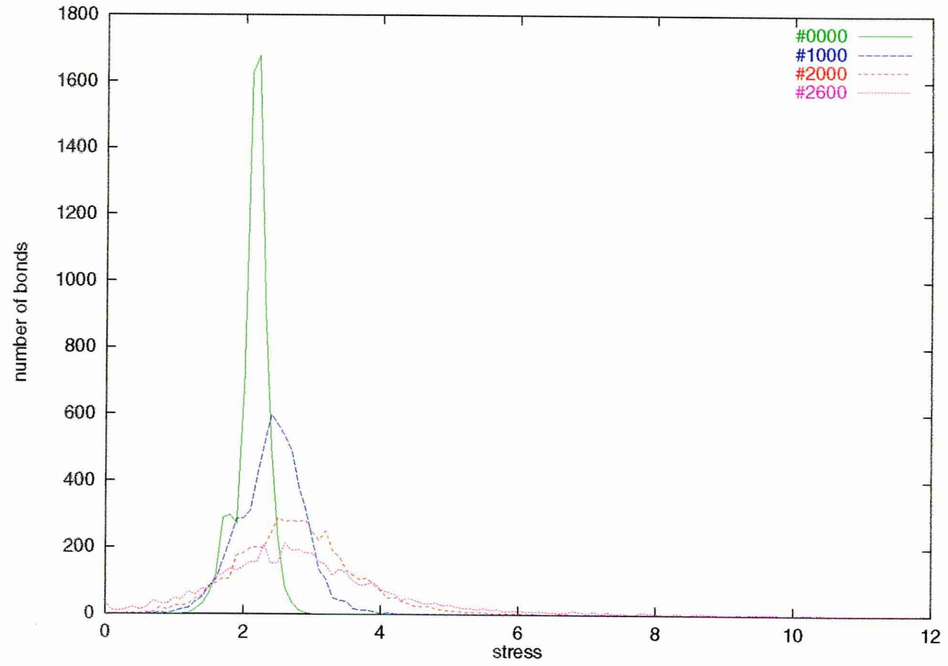

Figure 7.6: Evolution of the stress distribution of polymer bonds at different simulation steps. $20 \times 20 \times 20$ system with $\Phi = 10\%$, $k_r = 0.1$, $F_r = 8$

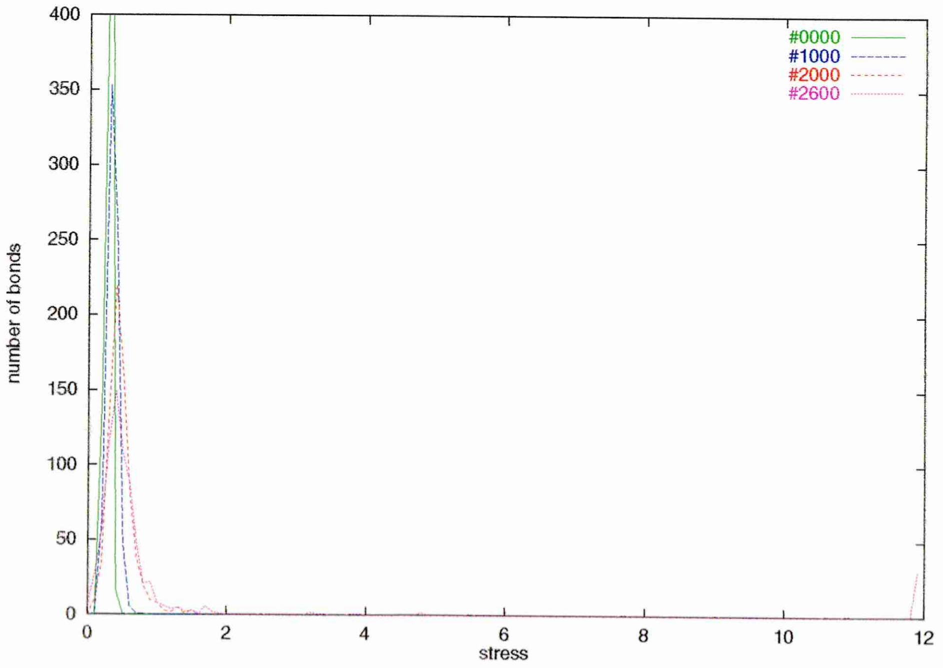

Figure 7.7: Evolution of the stress distribution of rubber bonds at different simulation steps. $20 \times 20 \times 20$ system with $\Phi = 10\%$)

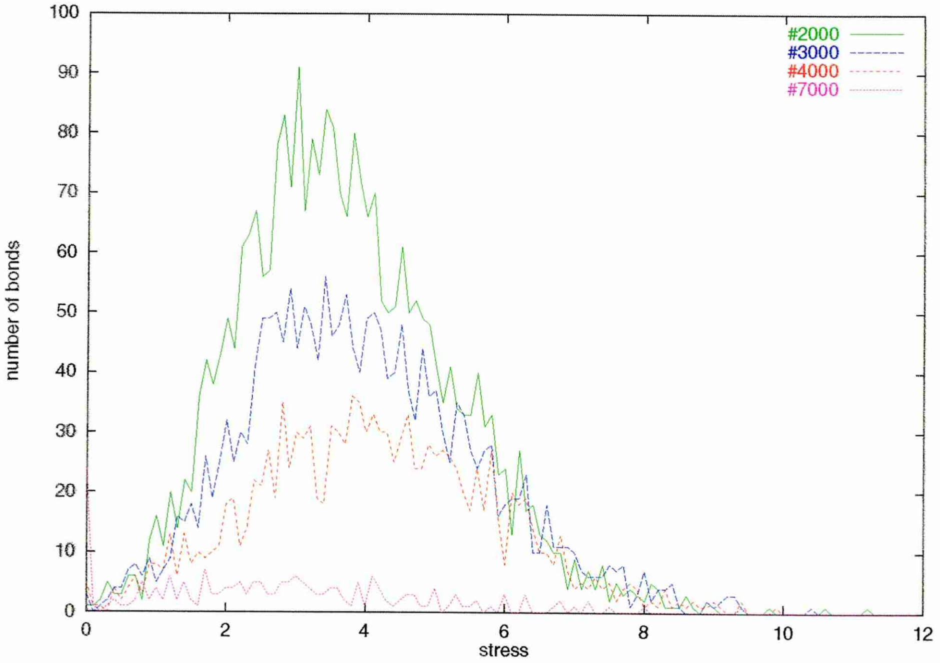

Figure 7.8: Evolution of the stress distribution of polymer bonds at different simulation steps. 20 × 20 × 20 system with $\Phi = 40\%$)

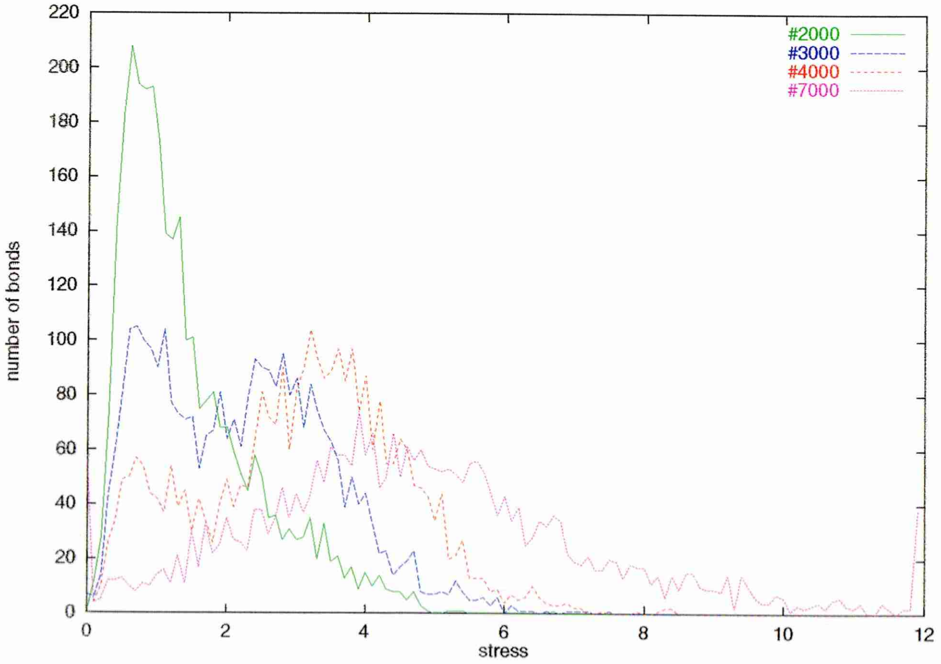

Figure 7.9: Evolution of the stress distribution of rubber bonds at different simulation steps. 20 × 20 × 20 system with $\Phi = 40\%$)

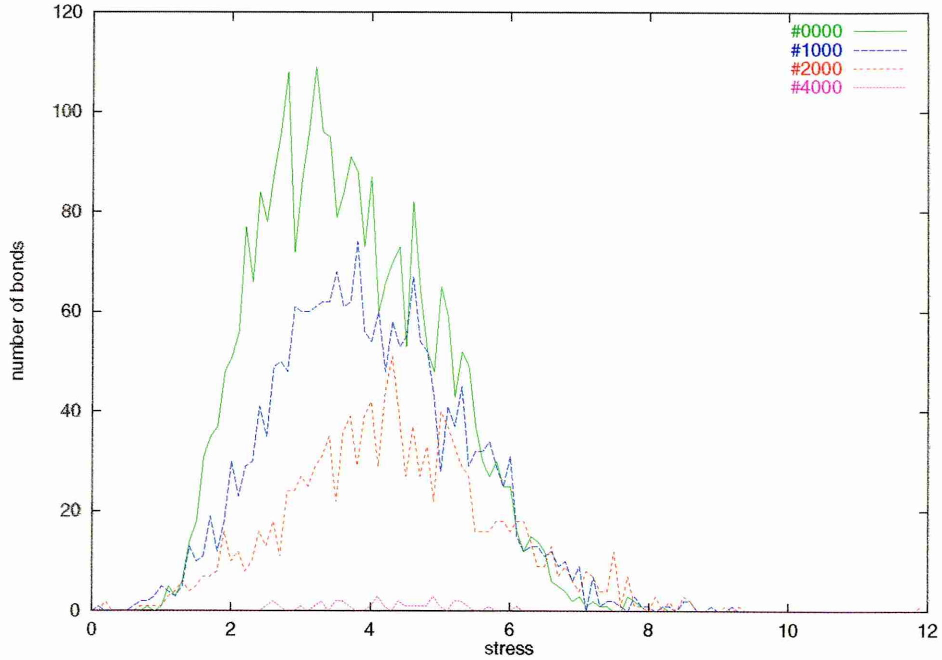

Figure 7.10: Evolution of the stress distribution of polymer bonds at different simulation steps. 20 × 20 × 20 system with $\Phi = 60\%$)

peak dominates, the initial one tending to disappear completely as the simulation approaches the material failure limit (step #7000). One can also notice that, at this point, a significant number of rubber bonds have become highly stressed, as shown by the long shoulder on the righthand side of the stress distribution curve.

High rubber loadings

For high rubber loading values ($\Phi > 50\%$), the evolution of the stress distribution, as illustrated in Fig 7.10 for $\Phi = 60\%$, does not change much from those of lower loadings. Here again, the main difference lies in the evolution of the stress in the rubber bonds. Fig 7.11 shows the shifting of the rubber stress distribution towards higher stress values and its broadening, as more bonds break in the simulation. The distribution splitting observed for moderate rubber concentrations is no longer observable, however.

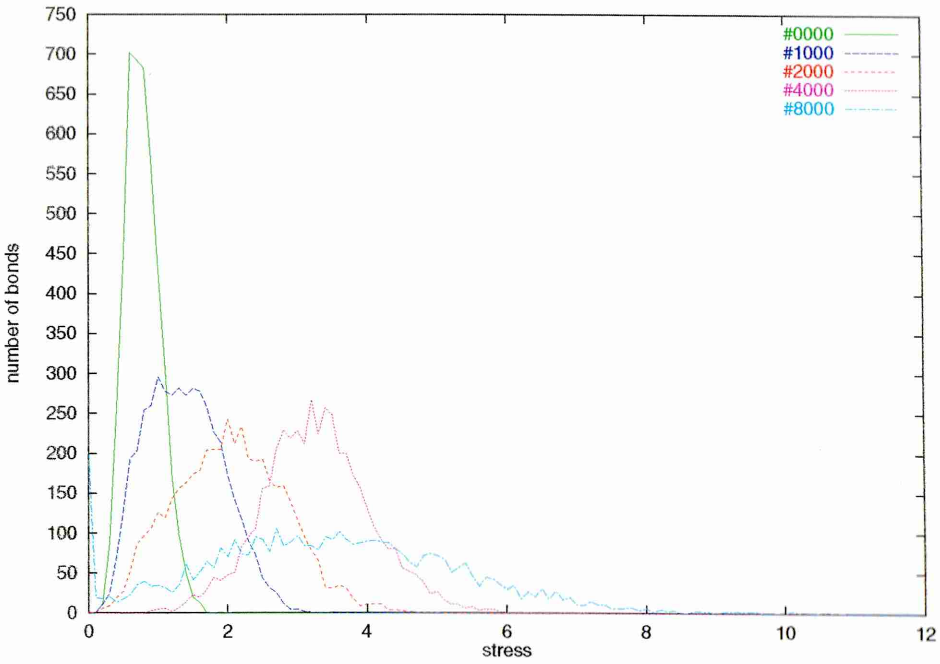

Figure 7.11: Evolution of the stress distribution of rubber bonds at different simulation steps. $20 \times 20 \times 20$ system with $\Phi = 60\%$)

Initial stress distribution of the bond populations

Fig 7.12 shows the initial stress distribution of the polymer bonds prior to any damage at various rubber loading values. The narrow and neat peak which is observable at low rubber loading ($\Phi \leq 10\%$) becomes wider as the loading increases. The distribution keeps its symmetry while developing a right side and left side shoulder. One can also notice a slight gradual shifting of the average stress value towards the higher values. On the other hand, the influence of the rubber concentration on the initial stress distribution within the rubber bond population seems to be negligible. The distribution curves shown in Fig 7.13 are all very similar. A slight increase in the average stress value is noticeable only for the highest rubber loading value ($\Phi = 60\%$) as the system becomes inverted (*ie* stiffer polymer bonds in a continuous rubber phase).

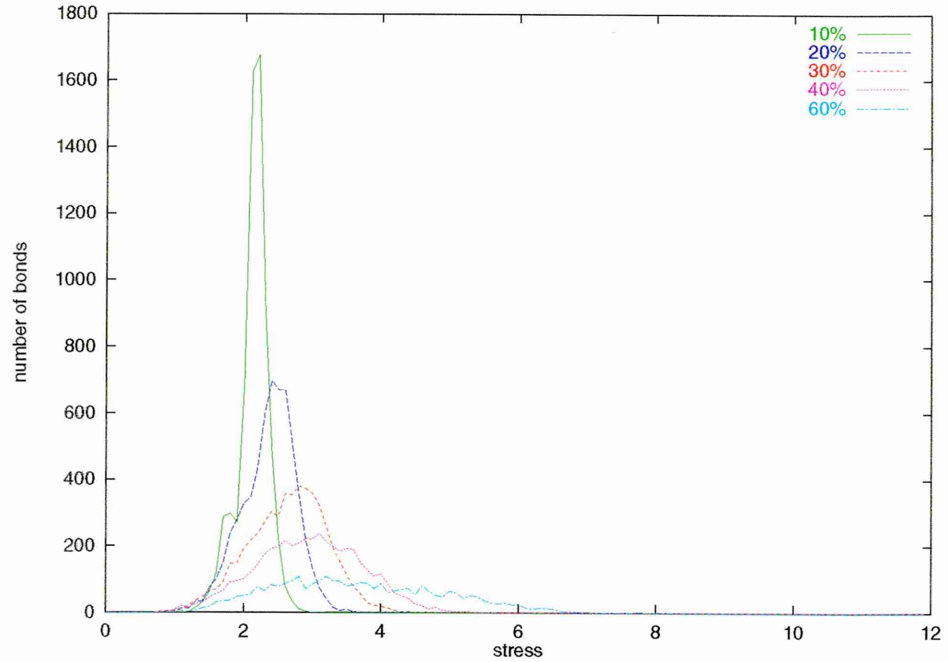

Figure 7.12: Initial stress distribution of polymer bonds at various rubber loadings in a 20 × 20 × 20 system

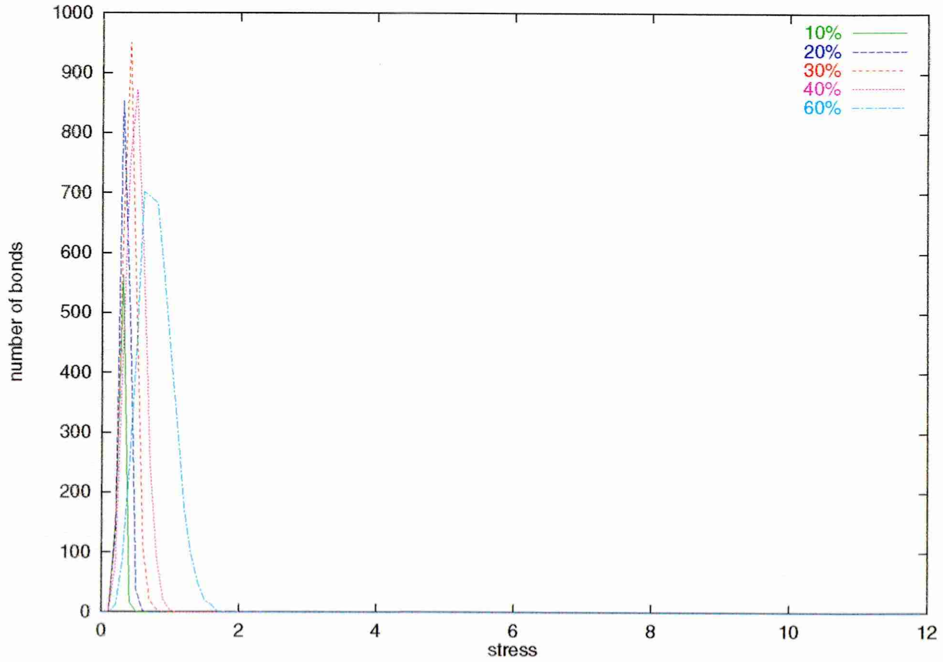

Figure 7.13: Initial stress distribution of rubber bonds at various rubber loadings in a 20 × 20 × 20 system

Discussion

As seen from Fig 7.6, Fig 7.8 and Fig 7.10, the stress distribution of the polymer bond population follows roughly the same evolution pattern for all rubber loadings. Such uniform stress behaviour might be the result of similar bond breaking development. Indeed, for any rubber loading value, the bond breaking process is dominated by the breaking of the polymer bonds, the rubber bonds involved in the broken bond count only coming towards the end of the simulations (this point will be shown later in section 7.3.2).

A possible explanation for the splitting in the rubber stress distribution observed for moderate rubber loadings could be the separation of the rubber population into two sets, each playing a different role in the material toughening. The evolution of these two rubber bond sets or populations is schematically illustrated in Fig 7.14. The first population of rubber bonds, which is present from the beginning of the simulations (stage **a**) can be interpreted as the rubber bonds surrounded by a relatively undamaged polymer matrix (bulk rubber bonds). This bond population tends to diminish as the damage progresses because, as certain of the rubber bonds become surrounded by more broken matrix bonds and microcrazes form around them, their role in the system changes to one of pinning these microcrazes (recall Fig 6.6). This results in an increase in their sustained stress and the appearance of a growing second peak in the stress distribution (stage **b**).

This explanation is consistent with the absence of such a stress splitting for low rubber loading systems, which show solely the presence of the first bulk rubber bond population. Indeed, these systems, which exhibit lower crack growth resistance and are characterised by a more linear fracture geometry (as seen in chapter 6, are not as craze-dominated as higher rubber loading systems. The rubber bond population involved in pinning the microcracks is, therefore, less important or almost negligible. This absence of rubber-pinning in low rubber loading systems might be explained by the important inter-particle (or rubber bond) distance in such systems; therefore, the stress the rubber bonds experience during pinning is greater than for higher rubber loadings, and they break.

When the damage approaches the material failure point in moderate rubber loading systems, the bulk rubber bond population has almost totally disappeared; most of the bulk rubber bonds have become craze-pinning bonds (stage **c**). The right side shoulder of this new stress distribution curve, which denotes the presence of a small, but non negligible, highly stressed rubber bond population, might account for the rubber bonds which have seen their pinning crazes grow (and maybe interconnect with others to evolve into rubber-bridged cracks).

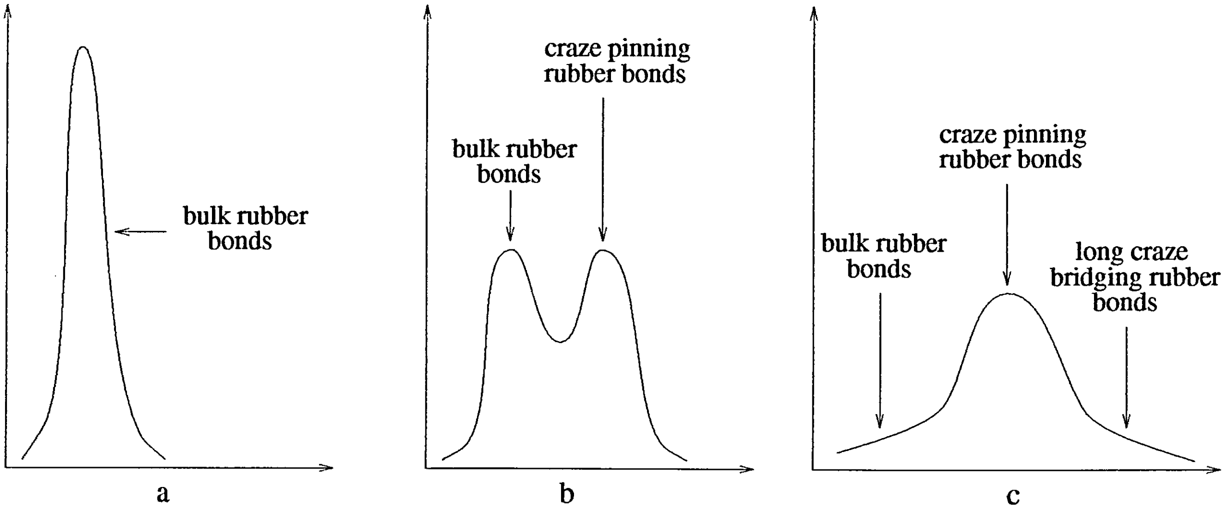

Figure 7.14: Schematic evolution of the stress distribution of the rubber bonds for moderate rubber loadings. Stage (a) : bulk rubber bonds predominant, stage (b) : appearance of the craze pinning rubber bond population, stage (c) : extinction of the bulk rubber bond population and appearance of a long craze bridging rubber bond population

The evolution of the stress distribution for high rubber loading systems does not exhibit a splitting of rubber bond populations. In these systems, the rubber bonds outnumber the polymer ones, therefore, as the polymer bond population is more prone to initial damage (*cf* section 7.3.2), the rubber bonds find themselves quickly surrounded by craze damage. The initial bulk rubber bond population is, therefore, bound to evolve quickly into craze-pinning bonds. As in moderate rubber loading system, this craze pinning population sees an increasing shift towards a longer craze situation as the damage approaches the material's failure limit.

Concerning the initial stress distribution among the polymer bond population, we see a relative increase in the importance of the two side shouders as the rubber loading Φ is increased. For small Φ, the majority of the polymer bonds are surrounded by other polymer bonds (bulk polymer bonds), a few of them are neighbouring a rubber bond, and these rubber-neighbouring bonds fall into two classes as illustrated in Fig 7.15 : the ones which are aligned with their rubber neighbour (colinear bonds or C-bonds) and the ones which are parallel to their rubber neighbour bond's sides (neighbouring bonds or N-bonds). The stresses sustained by theses two bond classes are different from those of the bulk bonds. The C-bond stress must be lower than the bulk-bond stress and the N-bond stress must be greater than the bulk-bond stress. The high stress distribution peak accounts, then, for the bulk bonds and the two side shoulders should account for the C-bonds (left) and the N-bonds (right) as illustrated in Fig 7.16. The relative importance of the C- and N- bonds increases as the number of rubber bonds increases and for high Φ the polymer bulk bond population disappears totally as every polymer bond is bound to be in the immediate vicinity of one or more rubber bonds. This situation is seen in real systems involving spherical rubber particles. The stress in the neighbourhood of the spherical particle is high around equator, but low near the poles.

7.2.2 Average and standard deviation of stress distributions

The evolution of the average stress $\overline{\sigma}$ and the stress standard deviation σ_σ have been studied for both bond types (polymer and rubber).

The results shown in Fig 7.17 ($\overline{\sigma}$) and Fig 7.18 (σ_σ) for $\Phi = 30\%$, $k_r = 0.1$ and $F_r = 8$ (these values have been chosen because they examplify the general trends)

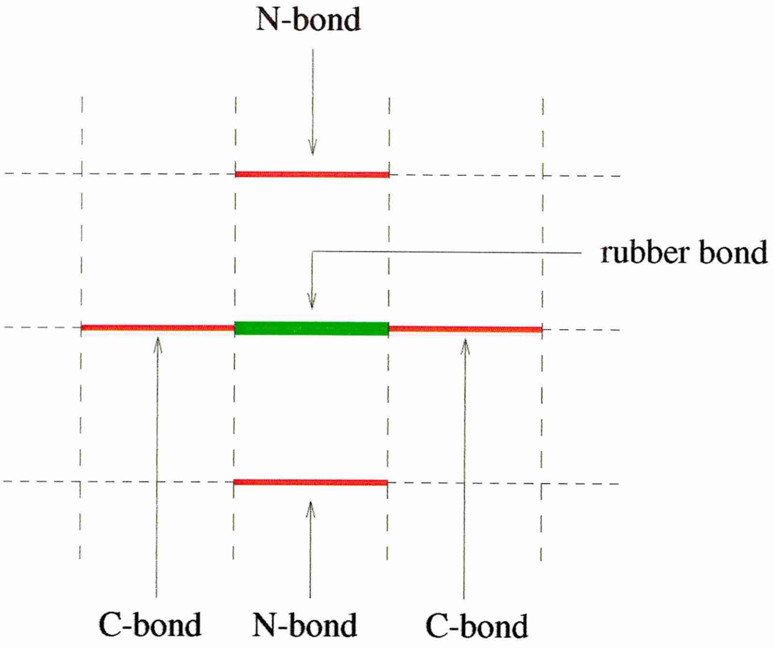

Figure 7.15: The two classes of the rubber-neighbouring polymer bonds in $2D$ systems

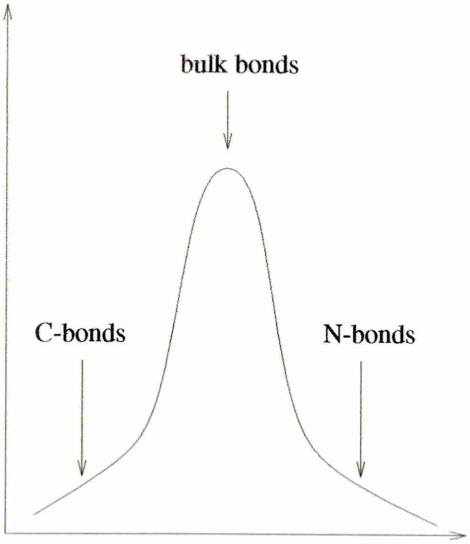

Figure 7.16: Schematic initial stress distribution of the different polymer bond populations.

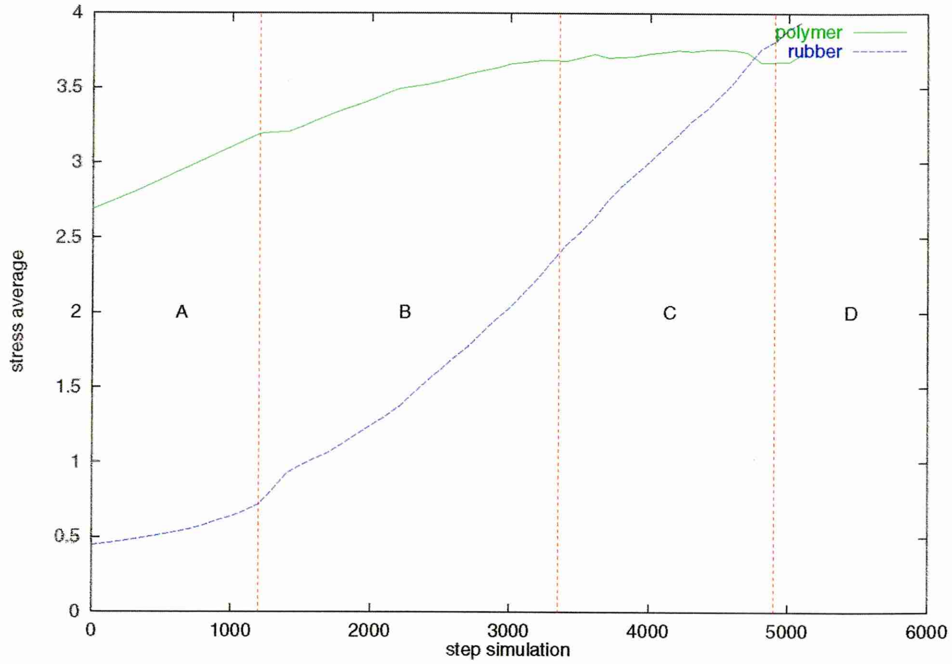

Figure 7.17: Average stress $\overline{\sigma}$ of polymer and rubber bonds in a $20 \times 20 \times 20$ system ($\Phi = 30\%$)

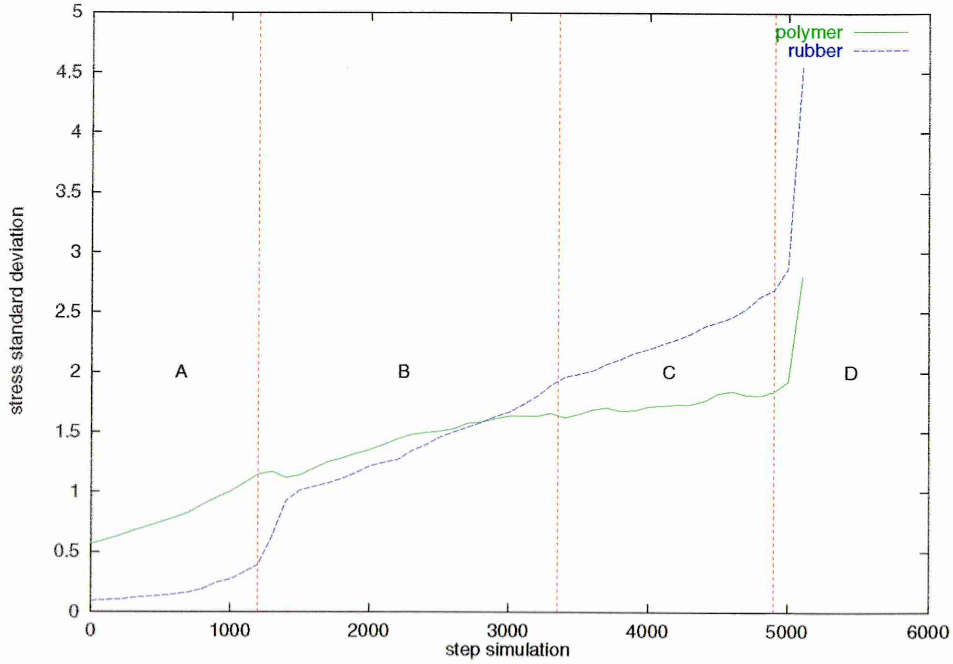

Figure 7.18: Stress standard deviation σ_{σ} of polymer and rubber bonds in a $20 \times 20 \times 20$ system ($\Phi = 30\%$)

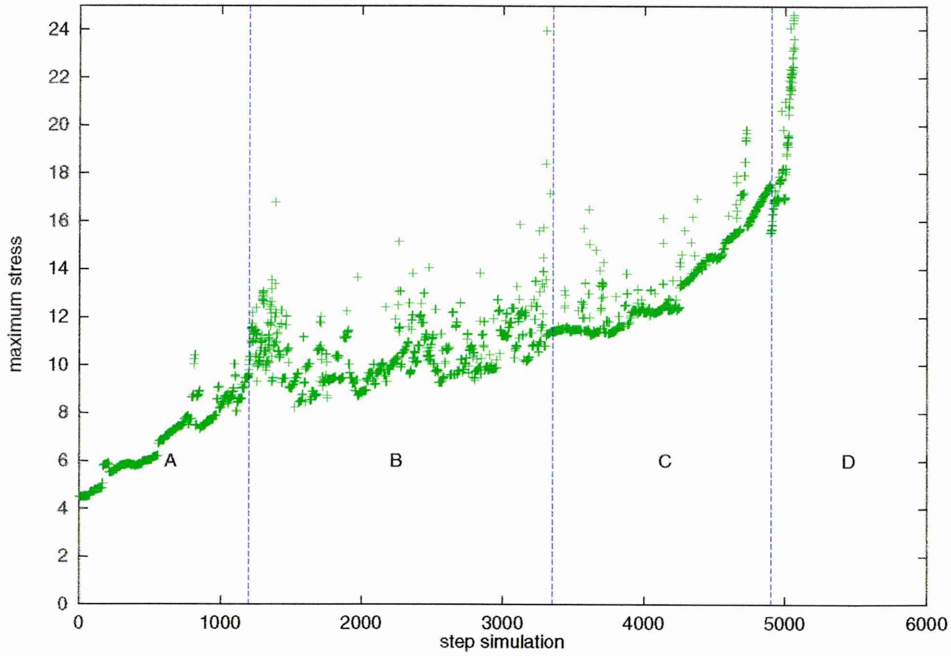

Figure 7.19: Maximum stress in $20 \times 20 \times 20$ system ($\Phi = 30\%$)

indicate a significant increase in $\overline{\sigma}$ and σ_σ for the rubber bonds at the onset of the noisy regime **B**, as shown in Fig 7.19. Before this, the stress in the rubber bonds seems to be moderate ($\overline{\sigma}$ is small) and well-distributed over all the bonds (σ_σ is small). After this jump in σ_σ, there is a wide distribution of stress values among the rubber bonds.

Concerning the polymer bonds, their average stress $\overline{\sigma}$ seems to build up steadily during regime **A**, starts to level out during the noisy regime **B** and does not grow any further during regime **C**. The same comments can be made for the evolution of the polymer standard deviation σ_σ : the stress dispersion grows steadily during regime **A**, levels out during regime **B**, and stabilises during regime **C**. The last failure regime **D** is characterised by a sharp increase in σ_σ for both polymer and rubber bonds.

From the evolution of the stress average $\overline{\sigma}$ for both bond natures as shown in Fig 7.17, one can notice that, for this set of simulation parameters, the system gradually evolves from a polymer stressed situation to a rubber stressed one throughout regimes **B** and **C** ($\overline{\sigma}$ of polymer bonds stabilises whereas $\overline{\sigma}$ of rubber bonds increases rapidly).

Discussion

The increase in the stress distribution average and standard deviation for the rubber bonds could be explained as being the result of a sudden lack of certain polymer bonds (due to their failure). Indeed, at the first stage of the breaking process, the most stressed bonds are the polymer bonds adjacent to rubber bonds (N-bonds). In regime **A**, therefore, these polymer bonds must break faster than any others. Eventually, when a significant fraction of these neighbouring polymer bonds are broken (formation of pre-crazes; we call pre-craze the small localised damage from which a craze migh likely develop), the rubber bonds become more stressed. From this point, with certain rubber bonds surrounded by damaged regions, the breaking process enters regime **B** in which these pre-crazed regions develop into bigger crazes.

Evolution of $\overline{\sigma}$ with Φ (polymer)

In Fig 7.20, we present the evolution of $\overline{\sigma}$ for polymer bonds at a series of different rubber loadings Φ. For moderate loading ($\Phi \leq 40\%$), we can see the stress stabilisation mentioned previously; for higher loading ($\Phi \geq 40\%$), this stabilisation is apparent but the average stress drops sharply after its maximum is reached. This sudden drop might be due to the loss of all polymer x-bonds (lattice bonds in direction of the external applied force) which are the most likely to sustain a high stress. Tab. 7.21 reports the simulation step N_F and the polymer damage d_F at which this fall occurs (d_F is the proportion of broken polymer bonds, $d_F = \frac{N_F}{N_p}$, with $N_p = (1 - \Phi)\, N$ the total number of polymer bond in the system and N the overall number of bonds in the system). The value of d_F is almost constant for all Φ and

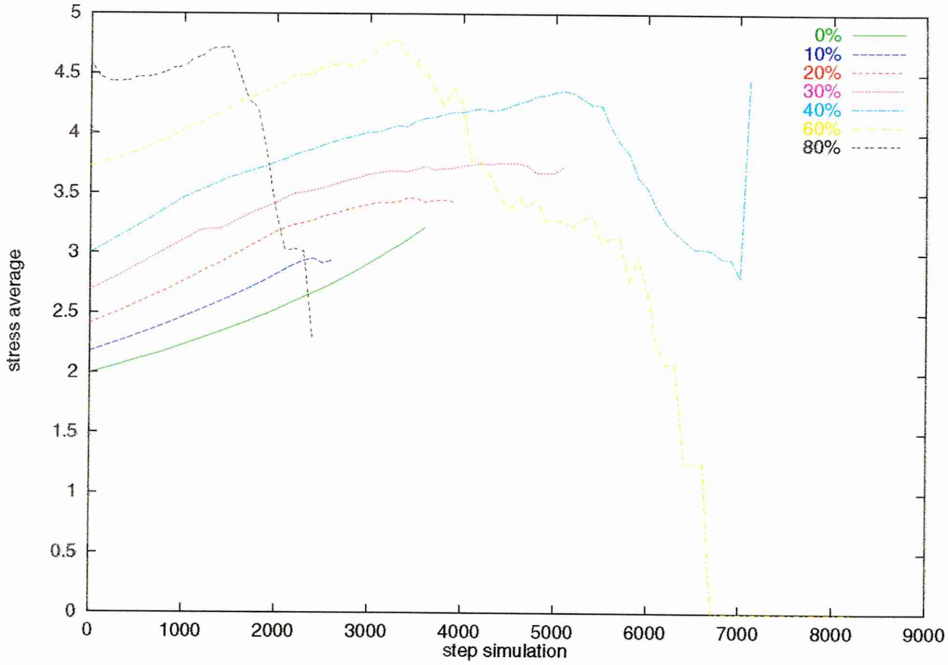

Figure 7.20: Stress average $\overline{\sigma}$ of polymer bonds in a $20 \times 20 \times 20$ system for different rubber loadings Φ

its value ($d_F \approx 1/3$) is consistent with the suggestion that all the polymer x-bonds (which amounts for $1/3$ N_p) are broken when $\overline{\sigma}$ exhibits this sudden drop.

Φ	40%	50%	60%	70%	80%	90%
N_F	5100	4100	3300	2300	1600	750
N_p	14400	12000	9600	7200	4800	2400
d_F	**0.35**	**0.34**	**0.34**	**0.32**	**0.33**	**0.31**

Figure 7.21: Polymer damage d_F for rubber loadings $\Phi \geq 40\%$

Evolution of σ_σ with Φ (rubber)

Fig 7.22 shows the evolution of σ_σ for rubber bonds at a series of rubber loadings Φ. The general evolution of σ_σ seem to follow the same trend for all values of Φ. At the beginning of the breaking process, the stress dispersion is quite small and starts to increase significantly only when the system enters the noisy regime **B** (for high rubber loading ($\Phi \geq 60\%$), this increase is not noticeable because, in

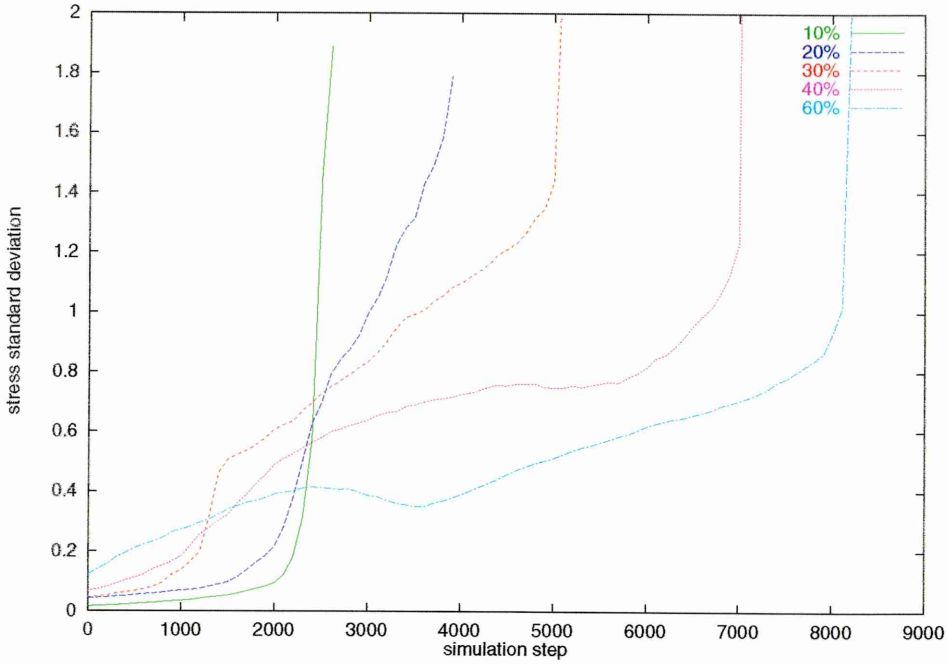

Figure 7.22: Stress standard deviation σ_σ of rubber bonds in a $20 \times 20 \times 20$ system for different rubber loadings Φ

this case, regime **A** is very short and the system enters regime **B** almost as soon as the breaking process has started) subsequently the rubber stress situation tends to stabilise for the biggest Φ's before it undergoes another important increase when the system enters the failure regime **D**. For the smallest Φ's, although the gradient of the stress dispersion curve decreases slightly after entering regime **B**, there is no evidence of any stabilisation.

Evolution of $\overline{\sigma}$ with Φ (rubber)

Fig 7.23 shows the evolution of $\overline{\sigma}$ for rubber bonds at a series of rubber loadings. During regime **A** and the transition to regime **B**, this evolution follows the trend of σ_σ : smooth increase up to the onset of the noisy regime **B**, the stress average steadily increasing as certain bonds become increasingly stressed. When the stress dispersion sees a sharp elevation, $\overline{\sigma}$ follows, acknowledging the sudden stress increase in certain bonds. An interesting change occurs in the middle section of the simulations for

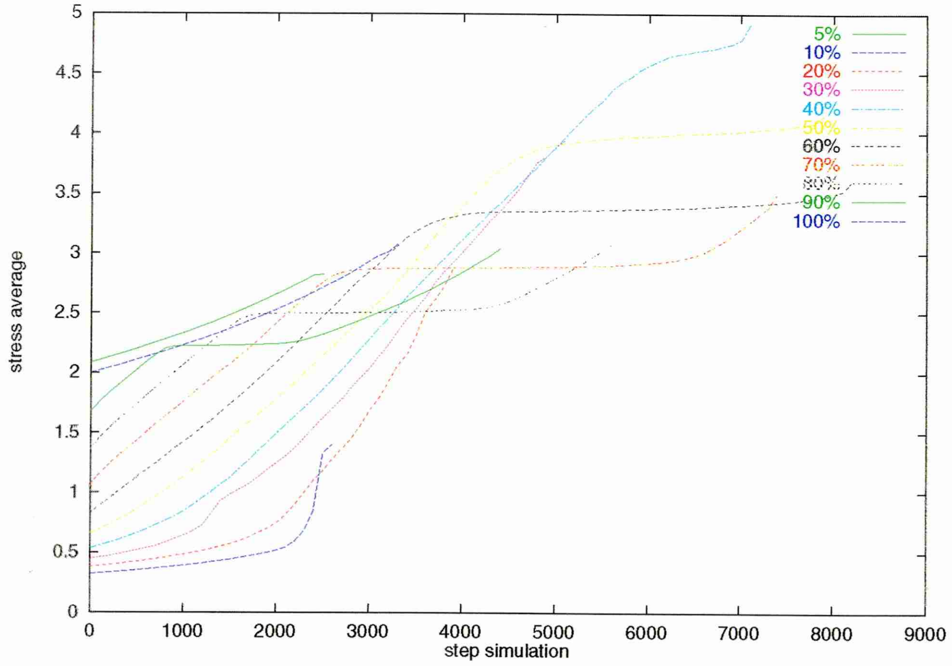

Figure 7.23: Stress average $\overline{\sigma}$ of rubber bonds in a $20 \times 20 \times 20$ system for different rubber loadings Φ

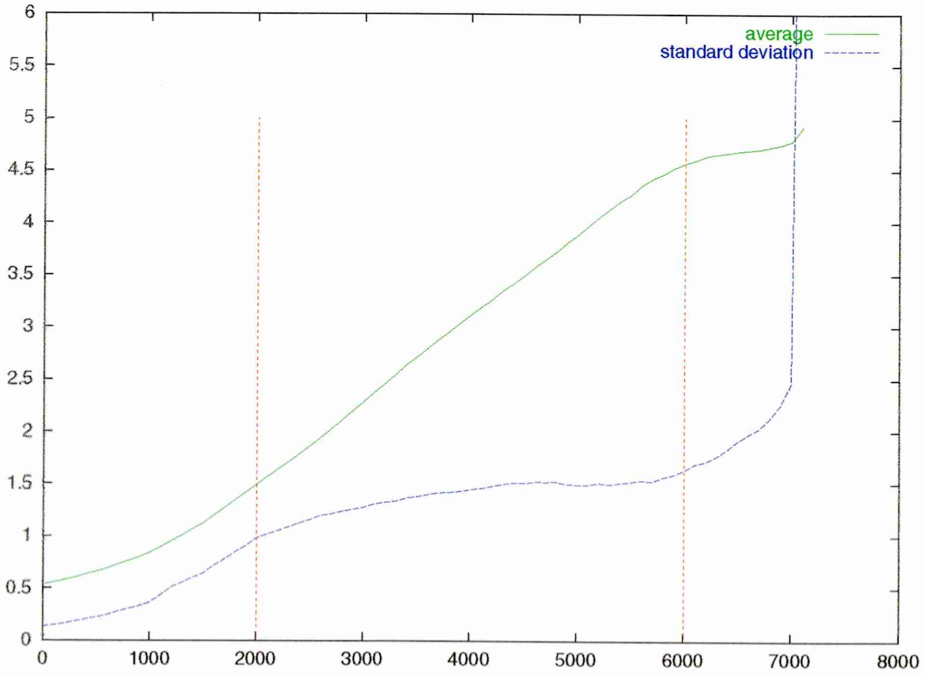

Figure 7.24: Comparative evolution of $\overline{\sigma}$ and σ_{σ} of rubber bonds in a $20 \times 20 \times 20$ system for $\Phi = 40\%$ (vertical lines indicate the changes of the trend)

high rubber loading systems ($\Phi \geq 40\%$), $\overline{\sigma}$ carries on growing whereas σ_σ tends to stabilise. This trend reverses later when $\overline{\sigma}$ stabilises and σ_σ suddenly increases (*cf* Fig 7.24 for $\Phi = 40\%$). It seems that, in the first change, the stress increase in the rubber bonds is well-balanced throughout the system, whereas, in the second change, only certain rubber bonds undergo a stress increase while the others undergo a stress decrease in order to balance the system's stress average.

Discussion

A possible interpretation of the stabilisation phase of σ_σ for rubber bonds, observable at regime **B**'s onset (*cf* Fig 7.22) could be the fact that, for high rubber loadings, some pre-crazes evolve quickly into crazes connecting rubber particles. The greater the value of Φ, the smaller the rubber inter-particle distance, therefore the quicker the crazes stemming from the vicinity of rubber bonds are able to connect each other. When sufficient crazes have joined, and are pinned by unbroken rubber bonds, the system reaches a state where the rubber bonds can be differentiated into two classes, those involved in pinning the crazes, and the rest, the former being more stressed than the latter (this has been shown in the previous section, recall Fig 7.14). The craze unzipping (or opening) process is responsible for the high rubber stress dispersion. For high rubber loadings, this process reaches a stabilisation phase; due to the small rubber inter-particle distance, a lot of crazes join. In comparison, for low rubber loadings, this unzipping process does not have enough time to stabilise; just a few crazes join and these develop into major cracks before the others have the opportunity to connect. Indeed, the stress at a crack tip is increased with the crack length a :

$$\sigma(a) \propto \sqrt{a}$$

Decreasing the inter-particle distance, then, decreases the stress sustained by the pinning (or bridging) particles. Futhermore, bridging reduces the stress at crack tips and make it independant of the crack lenght, giving cracks of various sizes equal chances for growth.

The last increase in σ_σ for the rubber bonds, which corresponds to the failure regime **D**, is due to the big stress difference existing between the last unbroken and highly stressed rubber bonds still bridging the main crack and the other rubber bonds of the system whose stresses remain virtually constant at rather low values.

7.2.3 Material overall elastic coefficient

The evolution of the material's overall elastic coefficient K has been measured throughout the whole breaking process. Because the overall material is modelled as a set of purely elastic bonds (whatever their configuration), the overall elastic coefficient can be defined as the external applied force F divided by the material's average elongation :

$$K = \frac{F}{\frac{1}{N}\sum_{i=1}^{N} \Delta x_i}$$

where N is the number of x-bonds in the lattice and Δx_i is the elongation of the ith x-bond.

The results are presented in Fig 7.25 for a system with $\Phi = 40\%$ ($k_r = 0.1$ and $F_r = 8$). We can see the evolution of K in terms of the four regimes observed from the maximum stress data (regimes **A**,**B**,**C**,**D**).

During regime **A**, the overall elastic coefficient decreases linearly. At each step, one polymer bond is removed from the lattice, its contribution to the overall coefficient is almost the same as that for all of the other bonds which break during this regime. During regime **A**, the system can be seen as predominantly polymeric, the polymer bonds are numerous and their role in the material elasticity is dominant.

When the system enters the noisy regime **B**, the decrease in K stops being linear. Throughout this regime, each polymer bond removal has a different relative contri-

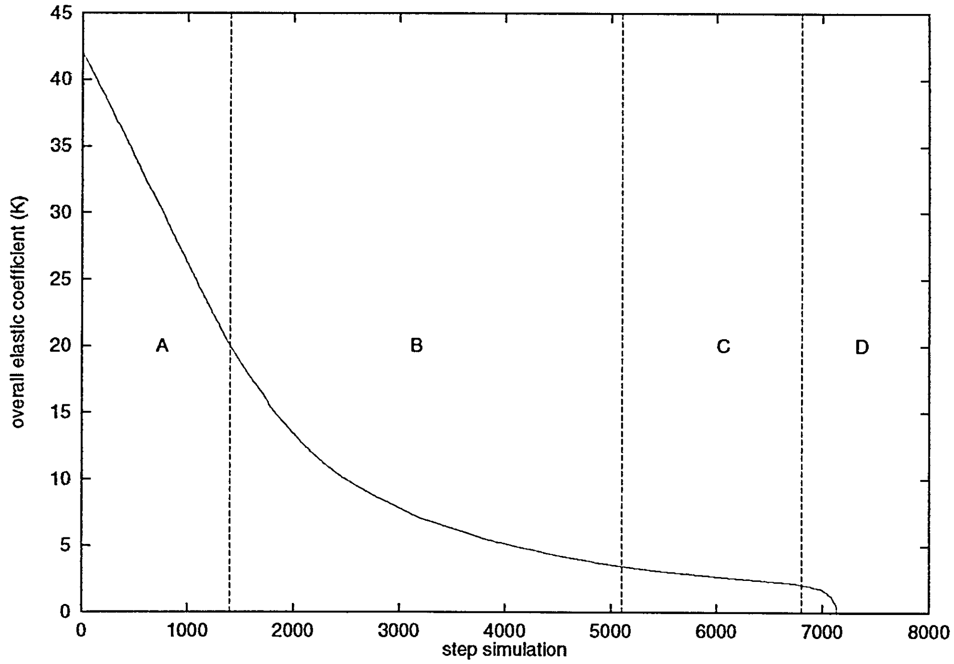

Figure 7.25: Evolution of overall elastic coefficient K of a $20 \times 20 \times 20$ with $\Phi = 40\%$

bution to the material's overall elasticity. An interpretation of this could be that the damage is no longer as randomly distributed as it is during regime **A**, instead, certain pre-crazed zones develop (into crazes) but others do not.

After this non-linear decrease, K goes back to a linear form, with a lower slope, at regime **C**. For this regime, as for regime **A**, the damage is well-distributed, and each bond breakage has the same elastic consequence. In this regime, the system can be seen as being "rubbery"; a lot of polymer bonds have been broken and, thus, the rubber bonds' elastic role becomes increasingly important. The bonds broken in this regime are not of major significance to the system's overall elasticity. Therefore, the intermediate regime **B** can be seen as representing a transition from a polymer-dominated system to a rubber-dominated one.

Towards the very end of the simulation, K drops suddenly to zero (material breakdown). This fall corresponds to the failure regime **D** where the main crack is only bridged by a few remaining rubber bonds. During this regime, the system is purely "rubbery" and is dominated by a small number of highly stressed parallel rubber bonds.

Rubber loading effects

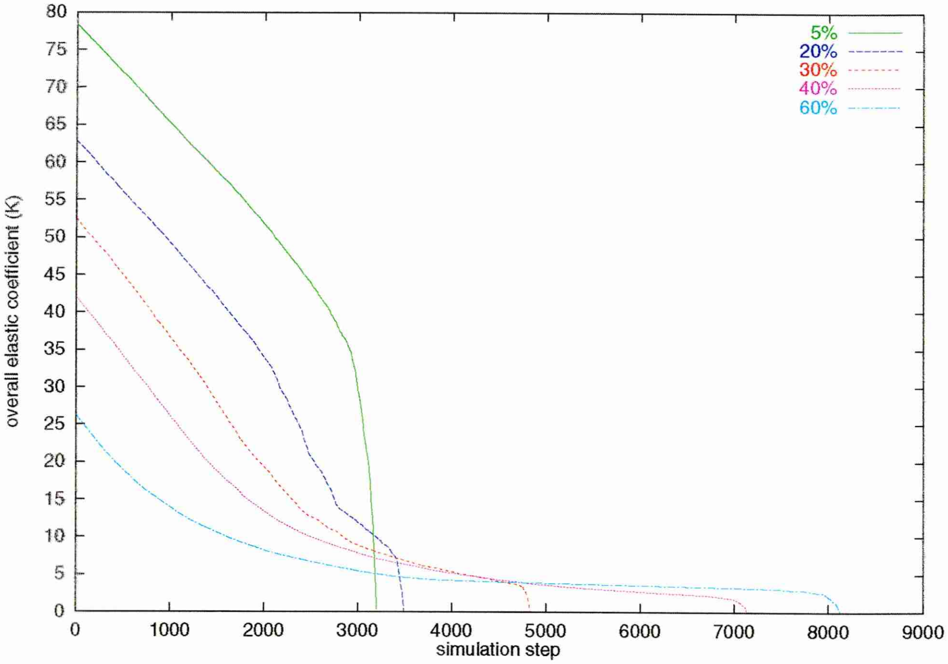

Figure 7.26: Evolution of overall elastic coefficient K of a $20 \times 20 \times 20$ for different rubber loadings Φ

Fig 7.26 presents the rubber loading Φ effects on the evolution of K. For all loadings where regime **A** can be observed ($\Phi < 60\%$), K displays the same linear decrease, the slope of which is independent of Φ. This is consistent with the assertion that the bonds breaking during this regime have the same elastic role for all rubber loadings. For $\Phi = 5\%$, as regimes **B** and **C** are very short, the evolution of K does not exhibit any change until the system enters regime **D**.

7.2.4 Broken bonds evolution

Not all polymer bonds have the same fate in the breaking process history. Those parallel to the applied external force (x-bonds) sustain a higher stress than the perpendicular ones (y- and z- bonds), and we have seen that the polymer bonds surrounding the rubber ones play an initial role in the craze formation.

We define the relative breaking rate at a given simutation step t for one type of bond as :

$$r(t) = \frac{N_{broken}(t)}{N_{initial}}$$

where $N_{broken}(t)$ is the number of broken bonds of this type at step t and N_{inital} is the initial number of bonds of this type. The values of r range between 0 (no damaged bonds) and 1 (all the bonds of this type are broken).

The evolution of the relative breaking rate (r) of different types of polymer bonds is presented in Fig 7.27 and Fig 7.28 for rubber loadings $\Phi = 20\%$ and 40% respectively. Four polymer bond types are presented :

- x-bonds in the immediate vicinity of a rubber x-bond (x-N-bonds),
- y- or z- bonds in the immediate vicinity of a rubber y- or $z-$ bond (perpendicular N-bonds),
- other x-bonds,
- other perpendicular bonds.

It appears that the N-bonds break relatively more frequently than the other direction-related bonds. This is even more evident for the x-bonds, for which the relative breaking rate goes up to more than three times the breaking rate of the other polymer x-bonds when $\Phi = 40\%$. The N-bonds' tendancy to break at a faster rate than the other bonds is illustrated in Fig 7.27 for a $\Phi = 20\%$ system. As shown in Fig 7.29 (which presents the evolution of the different polymer bond populations with Φ), at this rubber loading the N-bond population amounts the same as that of the other polymer bonds (approximatively 40% are N-bonds, 40% are other polymer bonds and 20% are rubber bonds). In this equilibrated situation one can notice

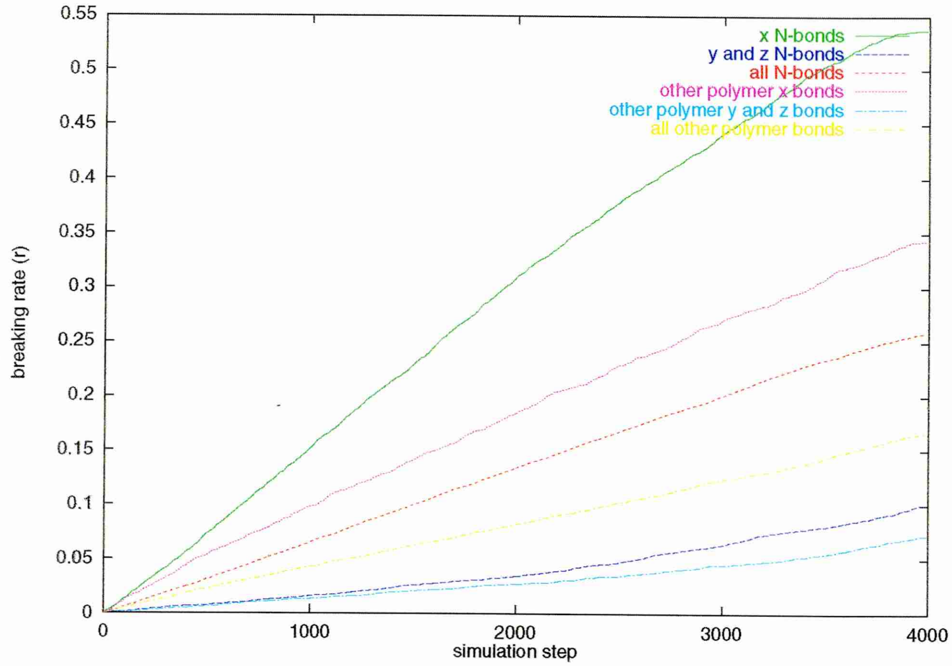

Figure 7.27: Breaking rates of different types of polymer bonds in a 20 × 20 × 20 system with rubber loading $\Phi = 20\%$

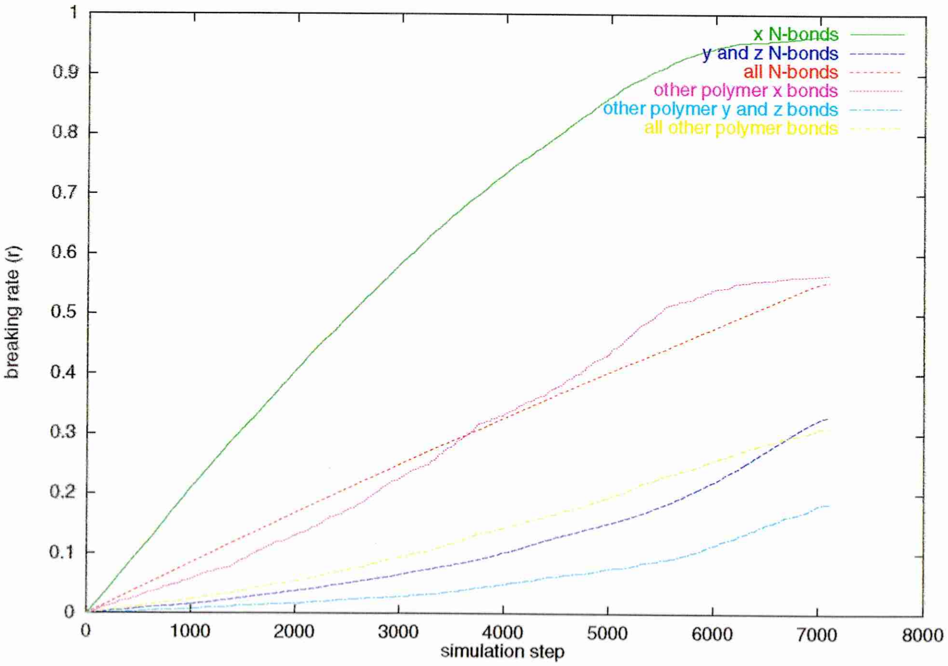

Figure 7.28: Breaking rates of different types of polymer bonds in a 20 × 20 × 20 system with rubber loading $\Phi = 40\%$

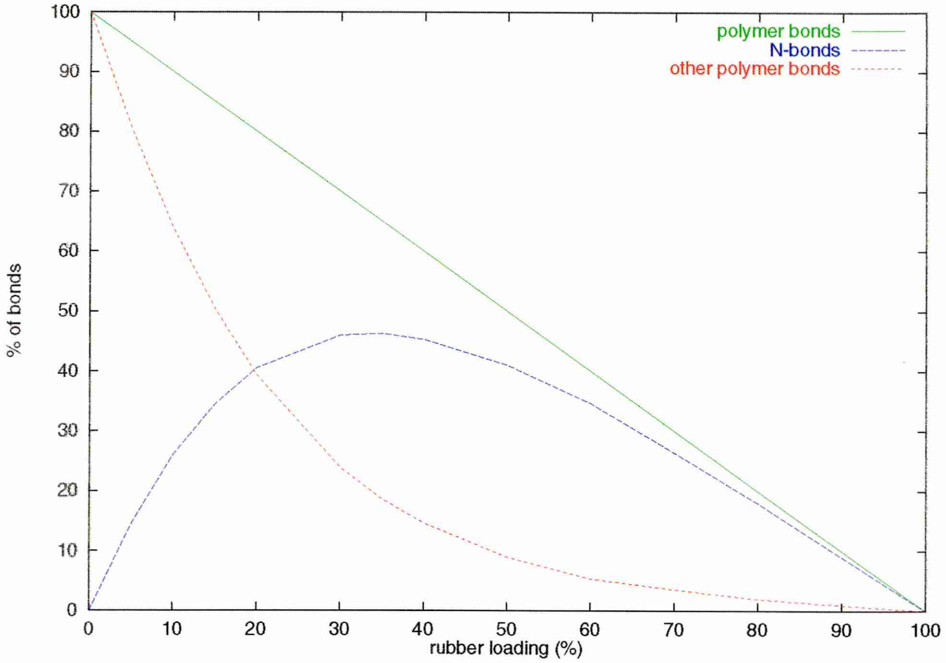

Figure 7.29: N-bond and other polymer bond population in an undamaged 3D system

from Fig. 7.27 that the x-N-bonds' breaking rate is nearly twice that of the other polymer x-bonds up to the middle of the simulation (step #2000). At the end of the simulation, the N-bond damage is still conspicuously dominant.

The evolution of the relative breaking rate seems to be linear, in the early stages, for all classes of polymer bond. Subsequently, non-linear behaviour develops : the perpendicular bond breaking rate tends to increase and that of the x-bonds tends to decrease. For high loading systems ($\Phi \geq 40\%$), the x-bond breaking rate even saturates towards the end of the simulation when almost all of the x- N-bonds have broken (*cf* Fig 7.28 for $\Phi = 40\%$).

It can be observed that the start of the non-linear evolution of r corresponds to the onset of the noisy regime **B** for loadings at which regimes **A** and **B** can be clearly distinguished. However, this correspondance is difficult to establish for low loadings (for $\Phi \leq 10\%$ regime **B** is very short and the linear evolution goes on throughout the breaking process) or high loadings (for $\Phi \geq 60\%$, where regime **A** is very short, the linear evolution tends to carry on until a sharp saturation).

Discussion

This early linear behaviour can be attributed to a steady stress evolution in the system, the damage being distributed evenly throughout the lattice. This trend changes when the system enters the noisy regime **B**, when pre-crazes unzip to form crazes. This craze unzipping process must involve the breaking of perpendicular bonds at an increased rate in order to interconnect neighbouring crazes.

An alternative explanation is that after a significant proportion of polymer x-bonds have broken, some members of the perpendicular polymer bond population, which, at this stage has suffered little damage, find themselves located in highly deformed regions. This subset of perpendicular bonds then undergoes a stress increase and becomes more likely to break than before. This is more conspicuous for high rubber loading systems for which, the polymer bond percentage being smaller, a high proportion of polymer x-bonds break in the early stages (for $\Phi = 60\%$, almost all of them get broken by the middle of the simulation). The bond breaking process then becomes dominated by the perpendicular polymer bonds. It can be noted that, for these highly rubber loaded systems, the onset of the x-bond breaking rate saturation occurs when almost all the x-N-bonds are broken ($r \longrightarrow 1$) and that it corresponds to the transition from regime **B** to regime **C**.

7.3 Significant bond results

We now consider specific bonds in the system in order to survey their evolution during the breaking process. We look first at the most stressed bonds before going on to data for the broken bonds. In both cases, we concentrate on the evolution of their nature (rubber or polymer) and their direction (x- or perpendicular).

7.3.1 Most stressed bond nature and bond direction

Bond nature

Fig 7.30 shows the evolution of the most stressed bond nature in correspondence with the maximum stress evolution for systems with rubber loadings of $\Phi = 20\%, 40\%, 50\%$. The maximum stress is sustained solely by polymer bonds up to a point in the simulation when the higher stress switches gradually to rubber bonds. One can notice that the onset of this switch from a polymer-stressed system to a rubber-stressed one occurs roughly at the transition from the noisy stress regime **B** to regime **C**. Regimes **A** and **B** are therefore characterised by a situation where the maximum stress resides on a polymer bond whereas regimes **C** and **D** correspond to a situation where the rubber bonds sustain the system's highest stress.

Bond direction

The evolution of the direction of the most stressed bond is presented in Fig 7.31 in correspondence with the evolution of the maximum stress for systems with rubber loadings of $\Phi = 10\%, 20\%, 30\%$. In the first part of the simulation, the maximum stress is carried by bonds oriented in the stretching direction (x-bonds), then this regularity is suddenly broken and the remaining part of the simulation sees a better distribution of the direction of the maximum stress, with, though, a domination of the x-bonds. This transition from a x-stressed system to a more ramdomly-stressed one corresponds coarsely with the onset of the noisy regime **B**.

7.3.2 Broken bond nature

Fig 7.32 shows the evolution of the broken bond nature in correspondence with the maximum stress evolution for systems with rubber loadings of $\Phi = 10\%, 30\%, 50\%$.

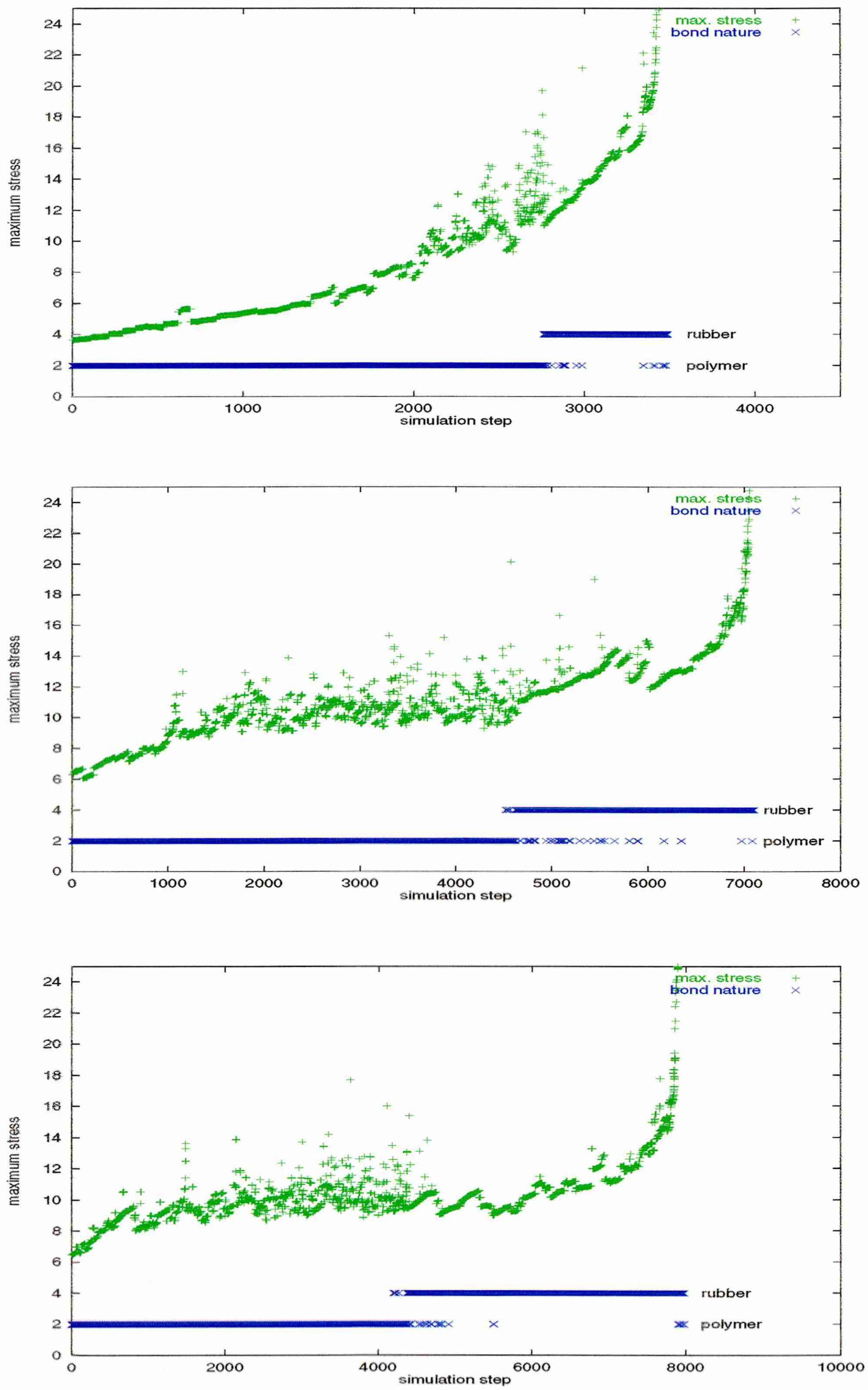

Figure 7.30: Evolution of most stress bond nature in correspondence with the evolution of the maximum stress for a $20 \times 20 \times 20$ system with rubber loadings, from top to bottom, $\Phi = 20\%, 40\%, 50\%$

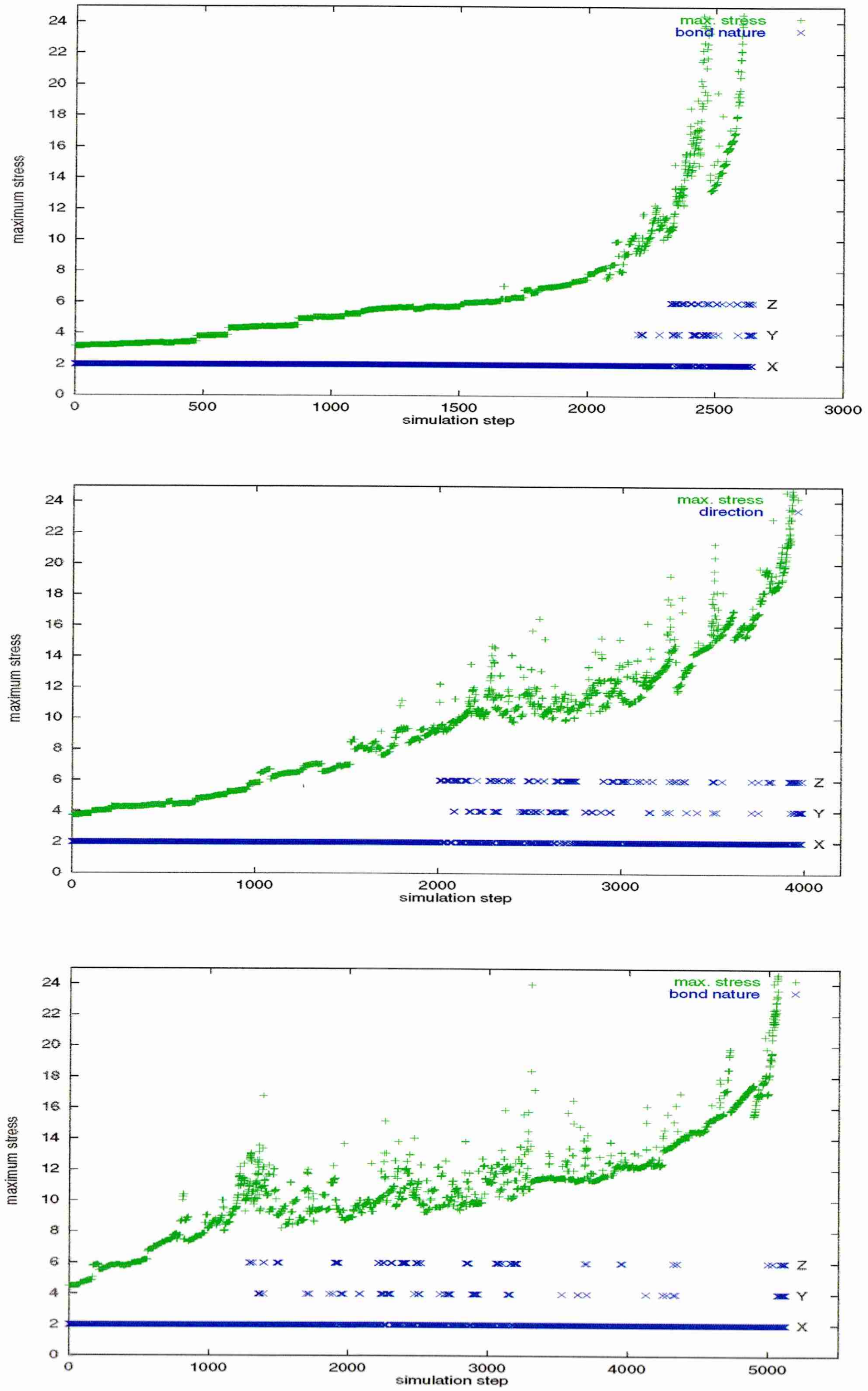

Figure 7.31: Evolution of most stress bond direction in correspondence with the evolution of the maximum stress for 20 × 20 × 20 systems with rubber loadings, from top to bottom, $\Phi = 10\%, 20\%, 30\%$

The damage is concentrated on the polymer bond population. During most of the simulation rubber bonds are hardly broken. The rubber bond population starts to experience damage only at the very end of the simulation. This rubber bond breaking regime seems to coincide with stress regime **D**.

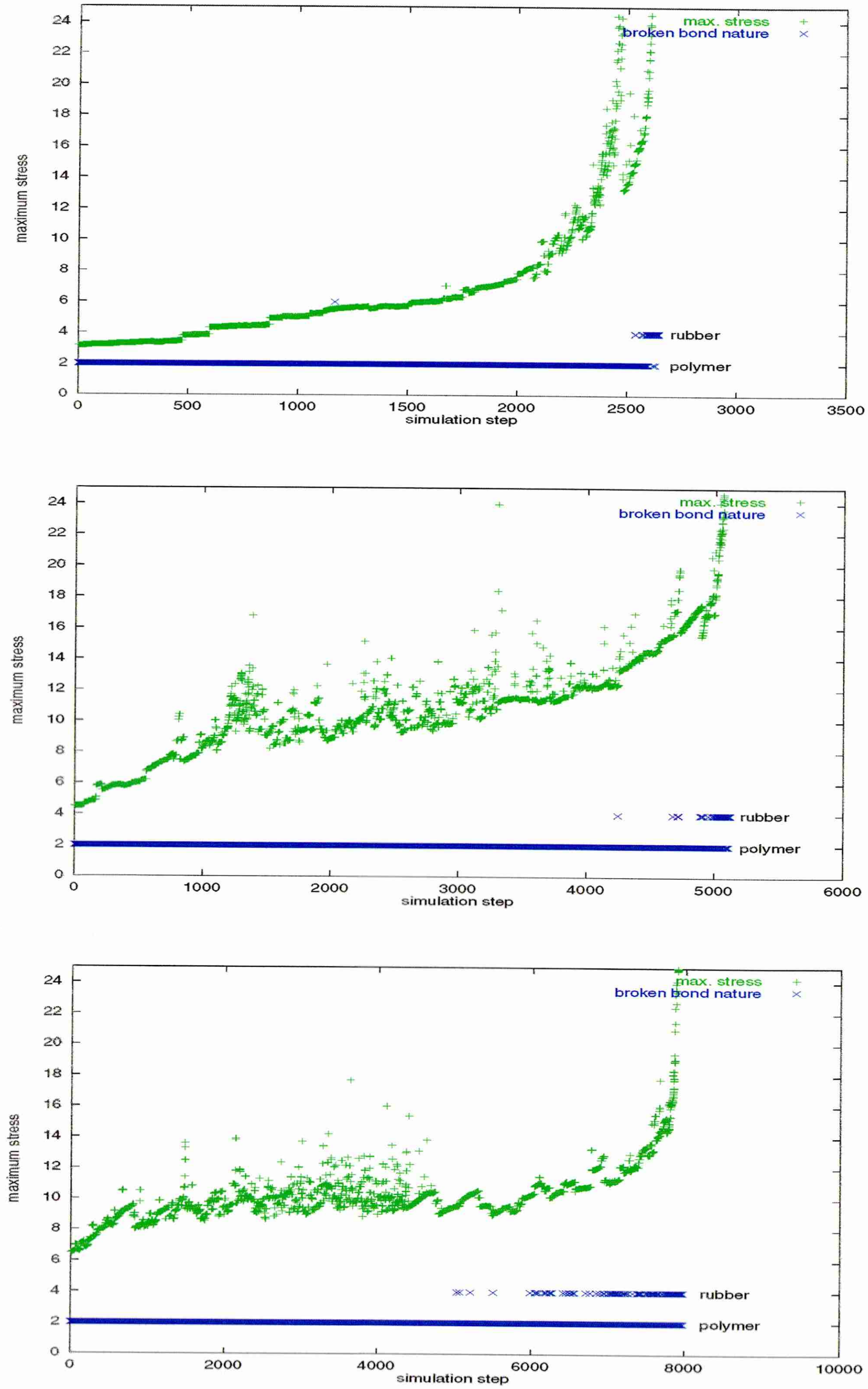

Figure 7.32: Evolution of broken bond nature in correspondence with the evolution of the maximum stress for 20 × 20 × 20 systems with rubber loadings, from top to bottom, $\Phi = 10\%, 30\%, 50\%$

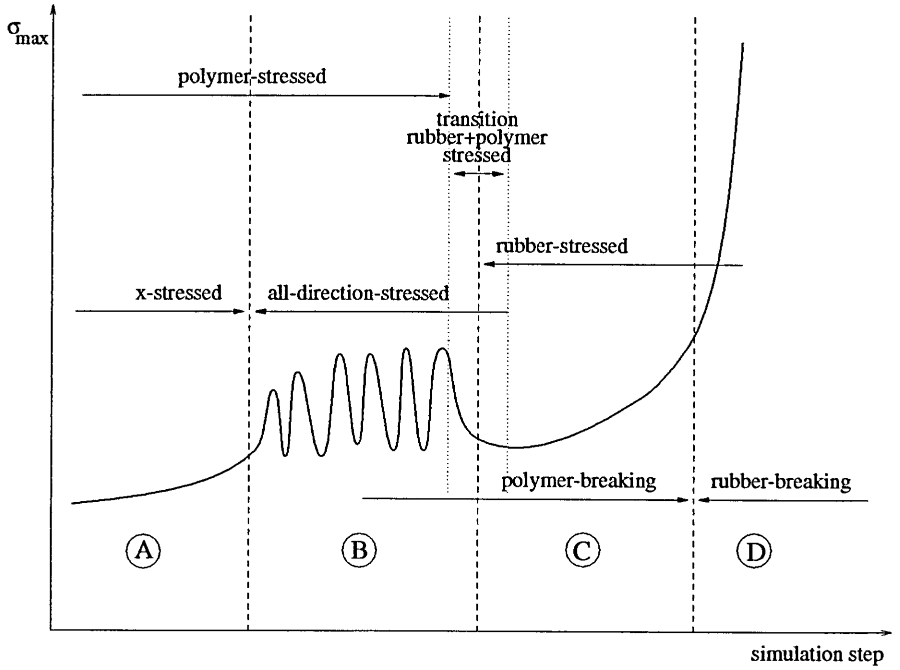

Figure 7.33: Schematic evolution of maximum stress

7.3.3 Significant bond conclusion

The different significant bond results are summarised schematically in Fig. 7.33 against the maximum stress evolution regimes. The four stress regimes are characterised by :

regime A : only polymer x-bonds experience maximum stress,

regime B : the onset of this regime corresponds to a change in the most stressed direction.

regime C : the onset of this regime corresponds to the maximum stress transition to only rubber bonds (with a transition period during which the maximum stress is experienced by both bond natures),

regime D : this regime corresponds to the switch from polymer breaking to rubber breaking.

7.4 Stress conclusions

The stress data which have been obtained from the various computer simulations fall into a range of categories :

- The **maximum stress evolution** : From these results, it had been shown that the maximum stress in any system evolves through four different regimes labelled **A**,**B**,**C** and **D**.
- The **stress distribution** has been looked at for low, moderate and high rubber concentration systems. The stress distributions of the two bond populations (rubber and polymer) have also been studied for undamaged systems at different rubber loadings.
- The evolution of the **stress average** and the **stress standard deviation**.
- The **material overall elastic coefficient** has been looked at in relation to the four stress regimes.
- The **broken bond evolution** has demonstrated that classes of bond must be differentiated in the breaking process.
- The **most stressed bond** and the **broken bond** studies have given interesting information on identifying the different bonds' roles in the evolution of the system's stress.

Some of these results, when mapped on to those of the maximum stress evolution, help the understanding of the four stress regimes. This, in turn, sheds some light on the breaking process history. The following observations can be made concerning the four stress regimes :

Regime A

When a force is applied to an undamaged system, prior to any bond breaking, the polymer bonds fall into three distinct classes : the bulk bonds, the C-bonds and the N-bonds. During the initial breaking process, the N-bonds break faster than any others. This damage, occuring around the rubber bonds, is well-distributed throughout the system and leads to the formation of pre-craze regions (small damaged matrix regions likely to develop into crazes). Regime **A** accounts for this initial homogeneously distributed damage phase. The maximum stress in the system must be located on a N-bonds or in the vicinity of a single broken bond. Every breaking bond step, one polymer bond is removed from the system and its elastic contribution to the material overall elasticity is virtually the same as those of the previously broken bonds. The maximum stress, therefore, builds up slowly and regularly. When the rubber concentration Φ is increased, even though the N-bond population grows (up to a level where the rubber bonds begin to form clusters), regime **A**'s span disminishes. The rubber inter-particle distance decreases and the smaller this distance is, the quicker the pre-craze regions can extend and interconnect. This, therefore, leads the system to a different phase during which crazes develop. The same span decrease is observed when k_r is decreased. In pure polymeric systems ($\Phi = 0$ or $k_r = 1$), regime **A** almost spans up to the onset of the final catastrophic regime **D**, regime **B** is very short and regime **C** cannot be observed.

Regime **A** seems then to characterise a homogeneous breaking process, where the pre-catastrophic damage is well-distributed and the stress steadily builds up until the system enters either (a) a craze opening phase, when the system is heterogeneous enough, or (b) the fast and final failure phase, for more homogeneous systems.

This interpretation is consistent with the following results :

- The regime span shrinks when the rubber loading Φ is augmented or the rubber coefficient k_r is diminished. It does not change when the rubber force threshold is modified.

- The stress average $\overline{\sigma}$ and the stress standard deviation σ_σ for both rubber and polymer bonds slowly increase, suggesting a smooth stress increase among all the bonds of the system, from a well-distributed stress situation to an increasingly inhomogeneous one.
- The material overall elastic coefficient K exhibits a linear decrease throughout this regime.
- The relative bond breaking rate r is constant for all the polymer bond classes.
- The maximum stress is sustained by polymer x-bonds.

Regime B

At the end of regime **A**, the damage, mainly in the form of pre-craze regions surrounding rubber bonds, is still fairly well-distributed in the system. Carrying the bond breaking process further leads to a sudden change in terms of stress. Certain rubber bonds experience a sharp stress increase whereas the polymer bond population sees its average stress levelling out. Polymer bonds still break, but their contribution to the material's overall elasticity has changed. This change has two forms : for low rubber loadings, the breaking of these polymer bonds leads to a faster decrease of the overall elastic coefficient, whereas, for high rubber loadings, this decrease is slowed down. The elasticity change in low rubber loading systems could be a result of certain of the pre-craze regions developing into crazes and interconnecting. The breaking of the polymer bonds at the craze tips has, indeed, a more important effect on the overall elasticity than other "bulk" polymer bonds. On the other hand, when the rubber loading is high enough, the rubber inter-particle distance is then so small that the pre-craze regions interconnect immediately; therefore, when entering regime **B**, the systems already contain rubber-pinned crazes.

During regime **B**, the maximum stress starts to be sustained by the perpendicular (y- and z-) bonds. As the crazes extend, the craze plane surfaces grow as well and the perpendicular bonds in the region between craze tips begin to see their sustained stress increase. These bonds must then break in order to interconnect craze planes (*cf* Fig 7.34).

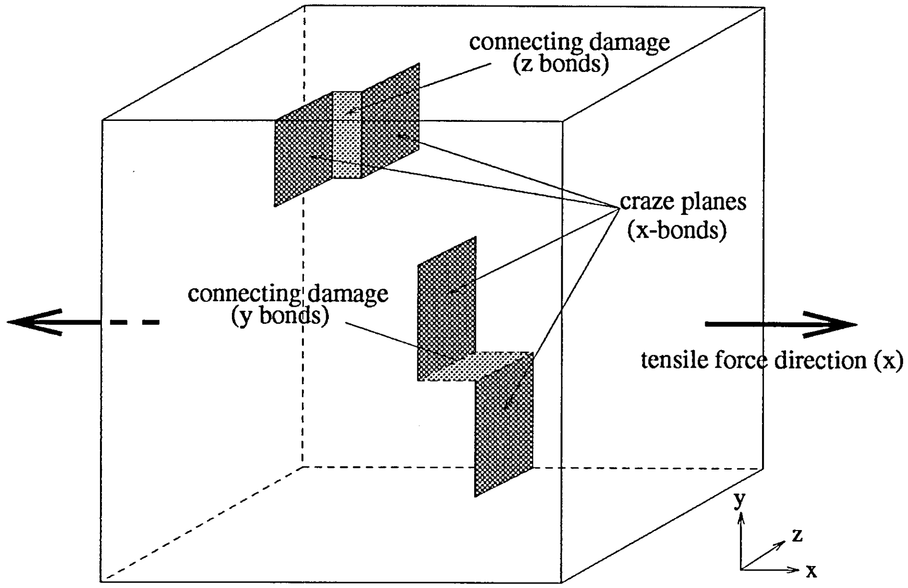

Figure 7.34: Schematic representation of craze planes connection

Regime **B** is, then, the regime during which more localised damage occurs : pre-crazes extend and join to form crazes (craze planes in 3D), which in turn connect with those on neighbouring planes.

This interpretation is consistent with the following results :

- The regime span follows a similar trend to the failure damage when the rubber loading Φ is increased. It shrinks down to being negligible when k_r is increased and, as for regime **A**, it is not sensitive to variations of F_r.
- The stress average $\overline{\sigma}$ and the stress standard deviation σ_σ of the rubber bonds exhibit a sudden increase at the onset of this regime and their evolution rate is then faster. Rubber bonds experience a sudden, inhomogeneously distributed

stress increase. The evolution of the stress of the polymer bond population tends to level out.

- The decrease of the material overall elastic coefficient K slows down.
- The relative bond breaking rate r of the polymer x-bond decreases as the breaking rate of the polymer perpendicular bond (y and z) increases.
- The maximum stress is now sustained by polymer bonds of any direction.

Regime C

This regime is characterised by a switch to a rubber-stressed situation which suggests that the rubber bonds role is changing. During regime **A**, the rubber bonds act like stress concentrators and therefore like damage attractors. During regime **B** crazes extend from certain rubber bonds to others. The situation at the onset of regime **C** is a set of joined or long rubber-pinned crazes, some of which may be long enough to form a rubber-pinned full fracture. From this point, the function of the rubber bonds is to bridge these macro damages. The maximum stress is then localised now on these crack-bridging rubber bonds. Their bridging efficiency depends, on one hand, on their force threshold F_r. Indeed, their breaking probability decreases with this threshold increase. On the other hand, the more rubber bonds involved in bridging a crack, the less stress each of them has to sustain, therefore this bridging toughening is more effective at higher rubber loadings.

During this regime the damage occurs in the rest of the material's bulk while the stress builds up in the bridging rubber bonds. Several potential main cracks might be competing during this regime.

Regime **C** can then be seen as a rubber-bridging phase, during which the material failure is delayed by the life duration of the bridging rubber bonds.

This interpretation is backed up by the following results :

- The regime span does not seem to depend on the value of k_r, but it increases with F_r and Φ.
- The stress average $\overline{\sigma}$ and the stress standard deviation σ_σ of the rubber bonds keep increasing whereas these parameters level out for the polymer bonds.
- The decrease of the material overall elastic coefficient K levels out and keeps a small value throughout this regime.
- The onset of this regime is characterised by a switching from a polymer maximum stressed bond situation to a rubber one.

Regime D

When the stress in some of the rubber-bridging bonds of one of the competing main cracks reaches some level, these rubber bonds fail, inducing a sudden stress increase in the others, which, in their turn, fail in an avalanche manner. This crack takes over from its competitors and leads the system to a catastrophic material break down.

This interpretation is consistent with the following results :

- The regime span is very short whatever the values of the different parameters.
- the maximum stress value sees a sudden and sharp rise.
- The stress average $\overline{\sigma}$ and the stress standard deviation σ_σ of the rubber bonds increase suddenly. The evolution of σ_σ is sharper and relatively more important than that of $\overline{\sigma}$, suggesting that just a few rubber bonds experience the violent stress increase.
- The material overall elastic coefficient K slumps down suddenly to zero.
- The onset of this regime is characterised by a rubber breaking situation.

The damage situation for these four stress regimes in illustrated in Fig 7.35.

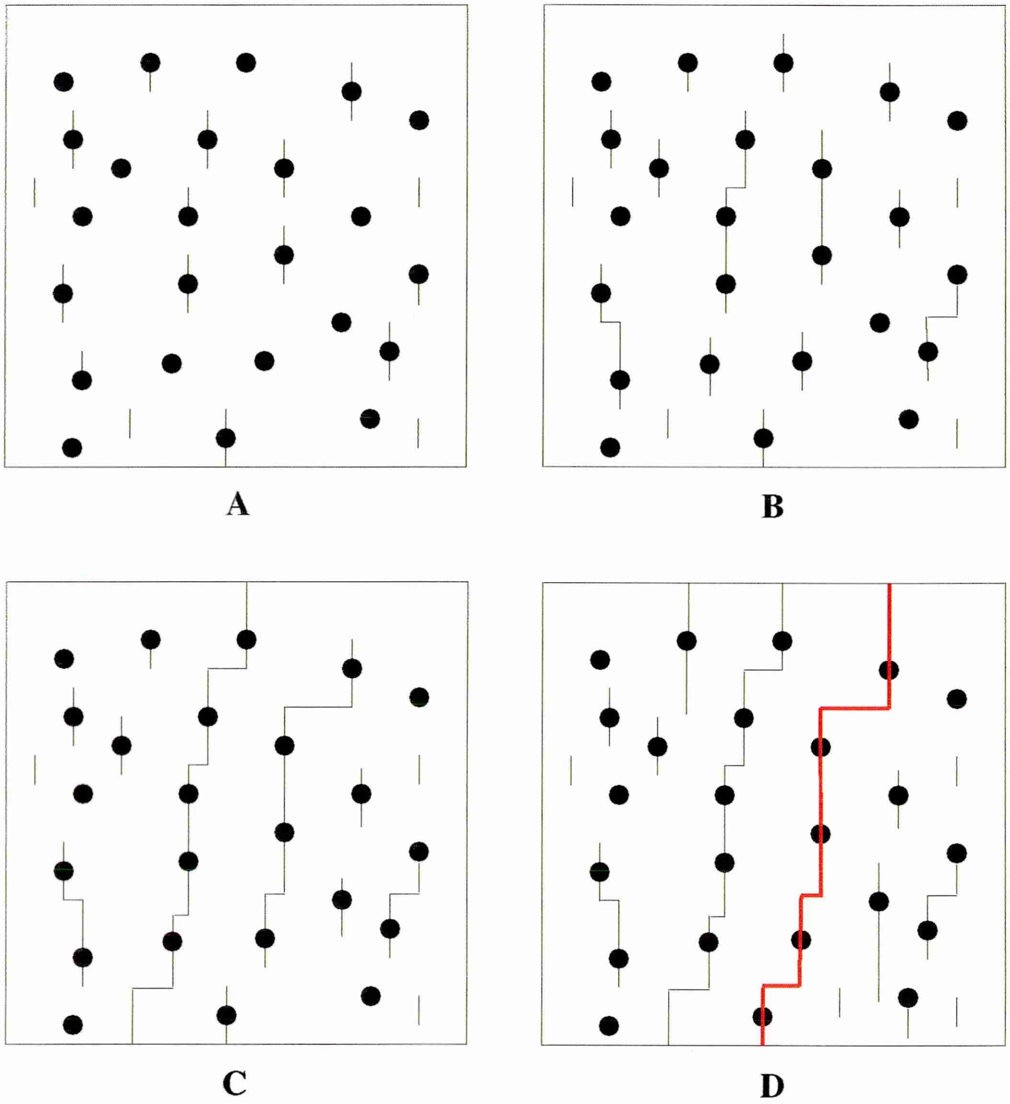

Figure 7.35: Schematic representation of the damage situation during the different stress regimes : A - well-distributed damage and pre-crazes formation, B - craze opening and joining, C - rubber bridging, D - material's failure (main crack in red)

7.5 Relation to real materials

7.5.1 Introduction

The stress results presented in this chapter have allowed us to identify four stress regimes, each of which corresponds to a different stage in the material's failure process. We want here to relate these different stages to what is observed in real rubber-toughened polymers. Recent experimental works [44, 81] have shed light on the damage development in these materials. Fig 7.36 illustrates the damage mechanisms in front of a crack tip in a notched sample of modified PMMA with 20% volume of rubber particles (the applied strain rate was $\approx 10^{-3}\ ms^{-1}$). Since the surroundings of the crack front offer a complete picture of the strain gradient, the whole sequence of deformation mechanisms can be observed, from the unstrained state up to the rupture. We can, therefore, try to relate the different stress regimes, and the corresponding deformation mechanisms exhibited by our model, to those observable in the damaged material.

7.5.2 Regime A

During this regime, we have seen that the damage is well-distributed and that craze nucleation occurs around rubber particles. View *b* from Fig 7.36 shows the damage in a low-strained region of the material and can therefore be related to what happens at an early stage of the breaking process, which corresponds to the model's regime **A**. The upper left region of the picture does not show contrast by the staining agent because of the absence of crazes. When moving closer to the crack tip, small crazes appear, stemming from rubber particles, as illustrated in view *c*. This can be related to the end of regime **A**, when the damage starts to localise at the tips of some pre-crazes, building up the stress in these confined regions, prior to craze-opening.

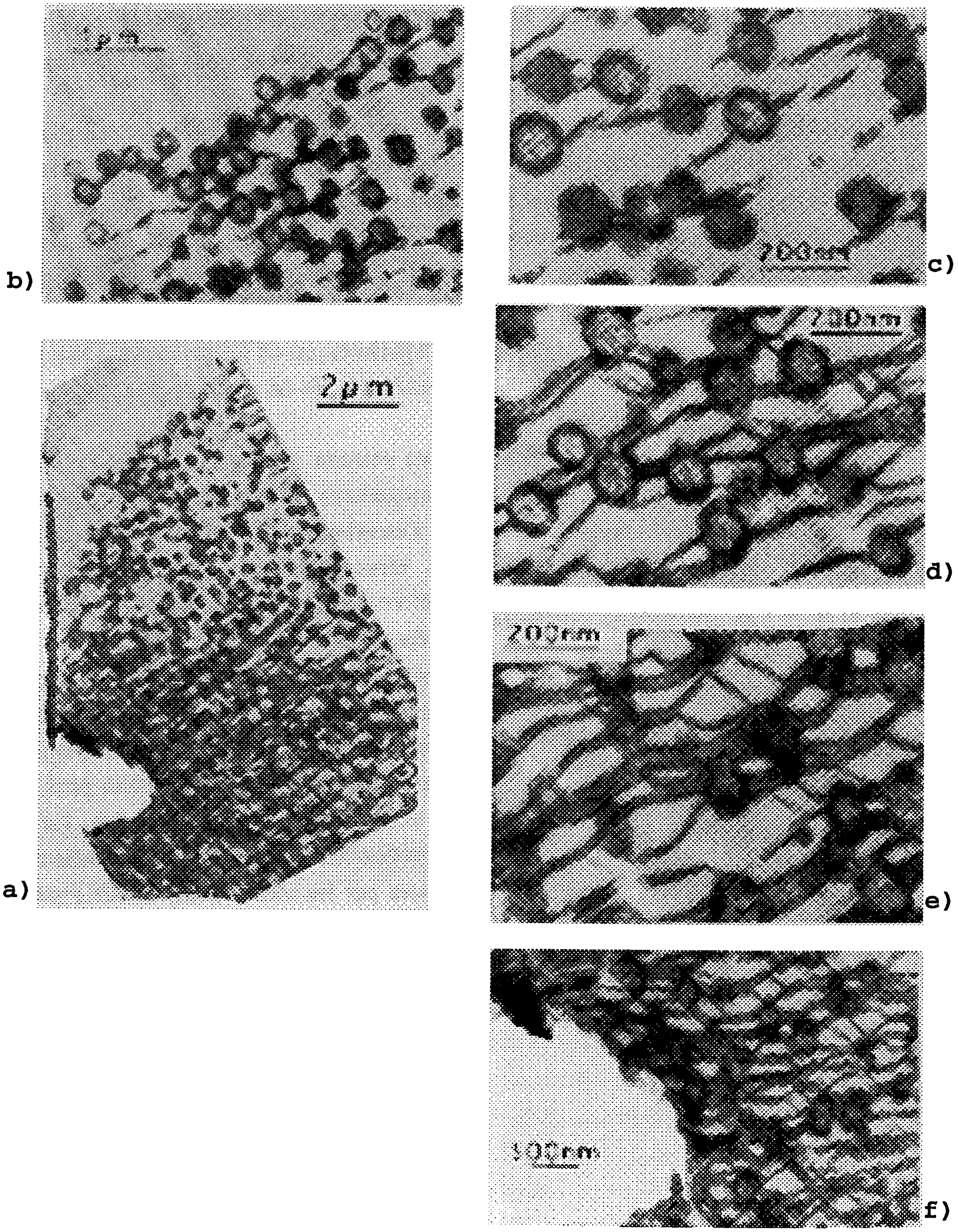

Figure 7.36: Deformation mechanisms in front of a crack tip in a PMMA modified with 20% vol. core-shell particles; a) overall view of the sample, other views (b-f) are from sample regions of decreasing distance to the crack tip (from [44])

7.5.3 Regime B

Regime **B** is characterised by a chaotic evolution on the maximum stress in the system. We have interpreted this as being the result of some crazes opening and joining. View *d*, corresponding to a futher deformation stage, can be related to this regime. Indeed, this view shows that crazes have extended and that a lot of particles are now connected by a craze-network.

7.5.4 Regime C

After some crazes have connected to form long particle-bridged cracks, the model's results have shown that the system enters a relatively steady stress state where the highest stresses are now located on rubber bonds. This rubber-bridging mechanism stabilises the crack growth and allows futher damage to occur. Views *e* and *f* correspond to the high-strained regions of the material and can be related to this regime. They, indeed, show firstly that some rubber particles are now fairly deformed due to the high stress they experience (and their stemming crazes are wider open). They also show that further damage has taken place in the form of parallel or branched crazes. A micrograph illustrating this rubber-bridging mechanism in a PMMA blend is presented in Fig 7.37 [16].

Regime **D** has to be related to material's regions very close to the main crack. It is, unfortunately, difficult to obtain contrasted micrographs of the rupture planes.

7.5.5 Conclusion

The stress results obtained from our model and their interpretation are consistent with the sequence of the deformation mechanisms observed in revelant rubber-toughened polymers. The different stress regimes identified in this chapter can

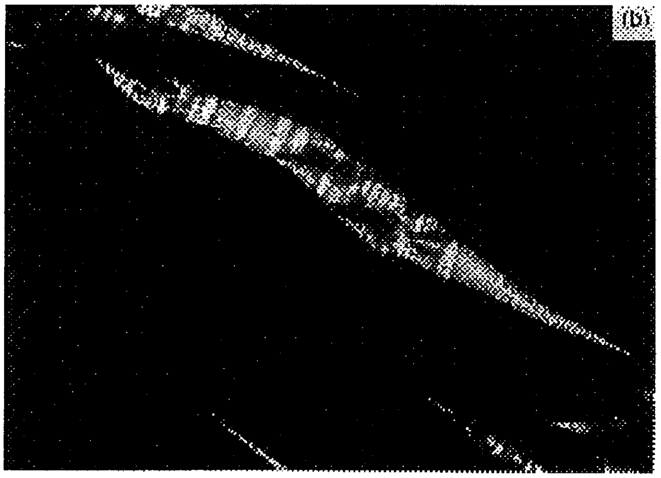

Figure 7.37: Rubber-bridging in a 0.15μm thick solution cast film of PMMA containing two-layer particles (from [16]).

be related to the damage history in the real materials.

Chapter 8

Visualisation

The results presented in this chapter are visual. They concern the pictorial representation of damage and stress in various 2D and 3D systems. The interpretation of these results is straightforward and gives a clear idea of the way cracks growth in different systems.

8.1 Damage in 3D systems

8.1.1 Heterogeneous systems

The damage for $20 \times 20 \times 20$ systems with different rubber concentrations Φ is presented in Figs 8.1, 8.2, 8.3, 8.4 ($k_r = 0.1$, $F_r = 8$ and $\Phi = 0\%, 10\%, 20\%, 40\%$, respectively); the external applied force is $F = 2$. For each rubber concentration, three views illustrate the damage situation at the material failure :

a) the complete damage (all the broken bonds),

b) the broken bonds connected to the main crack,

c) the main crack (broken bonds belonging to).

The pictures for the different rubber concentrations show an increase of the complete damage and of the main crack complexity with Φ, except for $\Phi = 10\%$ which is actually a material weakening concentration. The damage connectivity with the main crack seems to follow the main crack complexity trend; there is a small damage connectivity for straight and planar cracks ($\Phi = 0\%$ and 10%) but for $\Phi = 40\%$, when the crack surface is quite rough, almost all of the broken bonds are connected to the main crack. It can also be observed that, in all the systems, the rubber damage occurs only along the main crack.

These pictures seem to highlight two different toughening mechanisms :

- *Crazing* : the first views (all the broken bonds) show clearly that the damage is distributed throughout the bulk of the material and not just along the main crack.
- *Crack bridging*: the broken rubber bonds are essentially located on the main crack, bridging the two crack surfaces. As shown by animations, they are the last bonds to break.

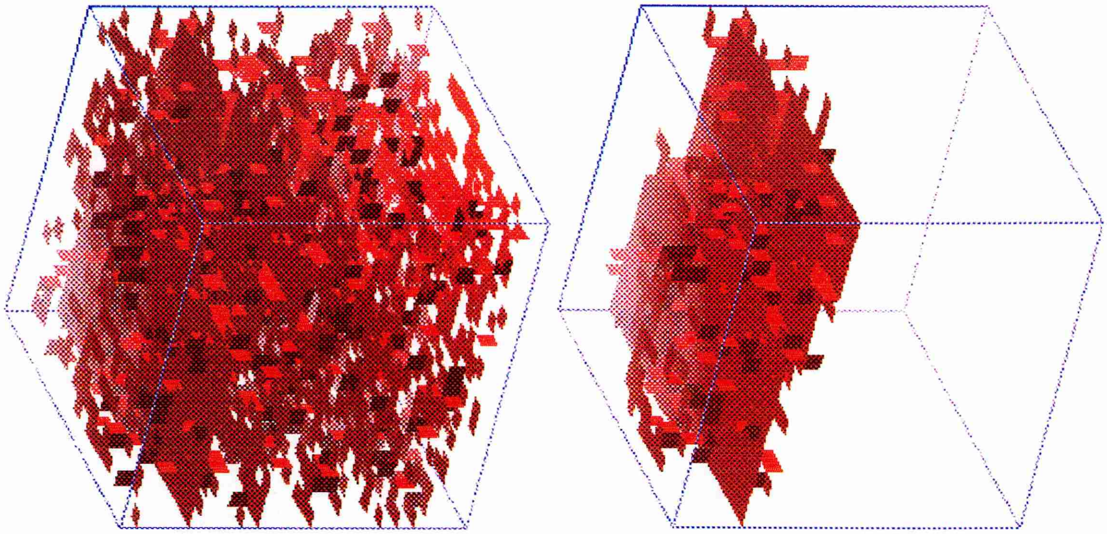

all broken bonds **broken bonds joined to main crack**

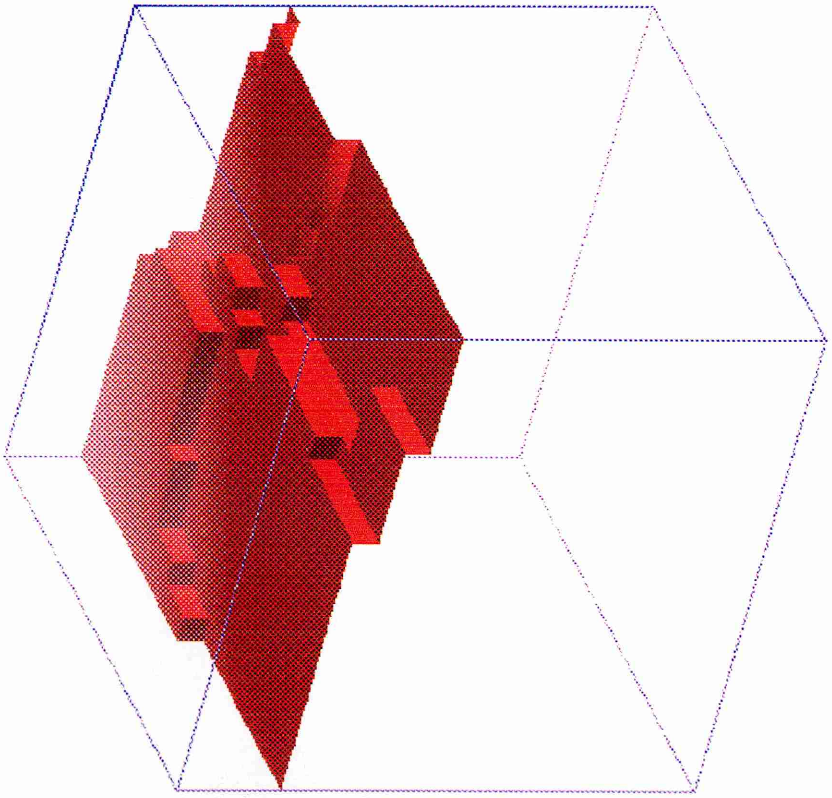

(minimal surface of) main crack

Figure 8.1: Damage in $20 \times 20 \times 20$ system with $\Phi = 0\%$.

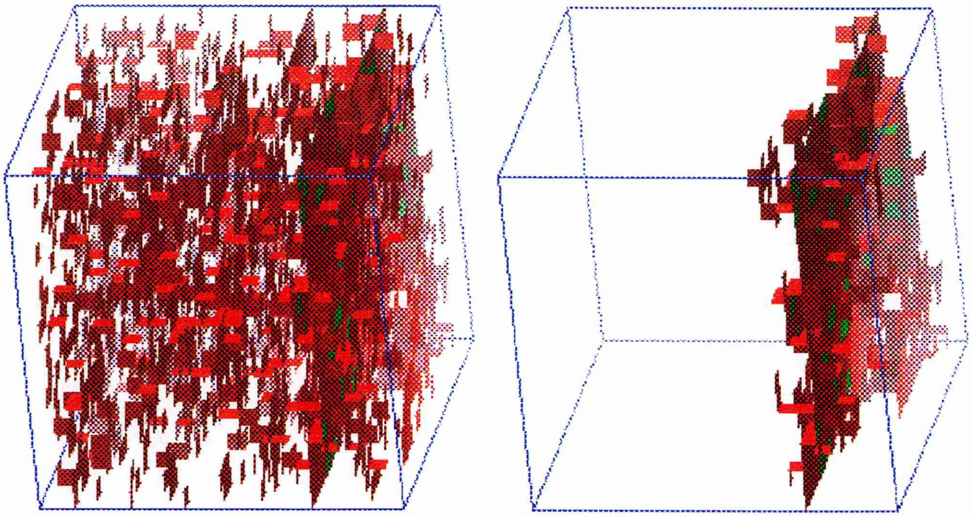

all broken bonds **broken bonds joined to main crack**

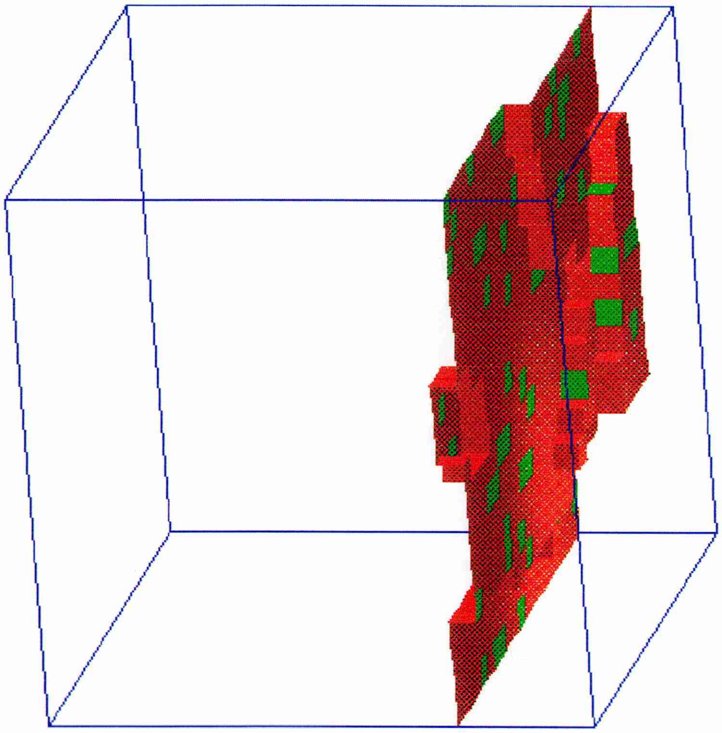

(minimal surface of) main crack

Figure 8.2: Damage in $20 \times 20 \times 20$ system with $\Phi = 10\%$.

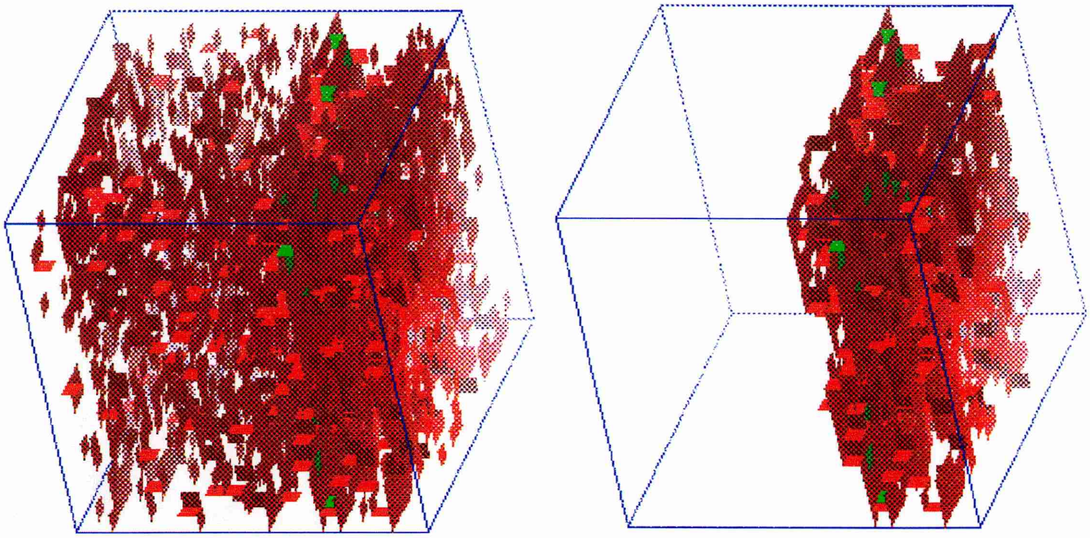

all broken bonds

broken bonds joined to main crack

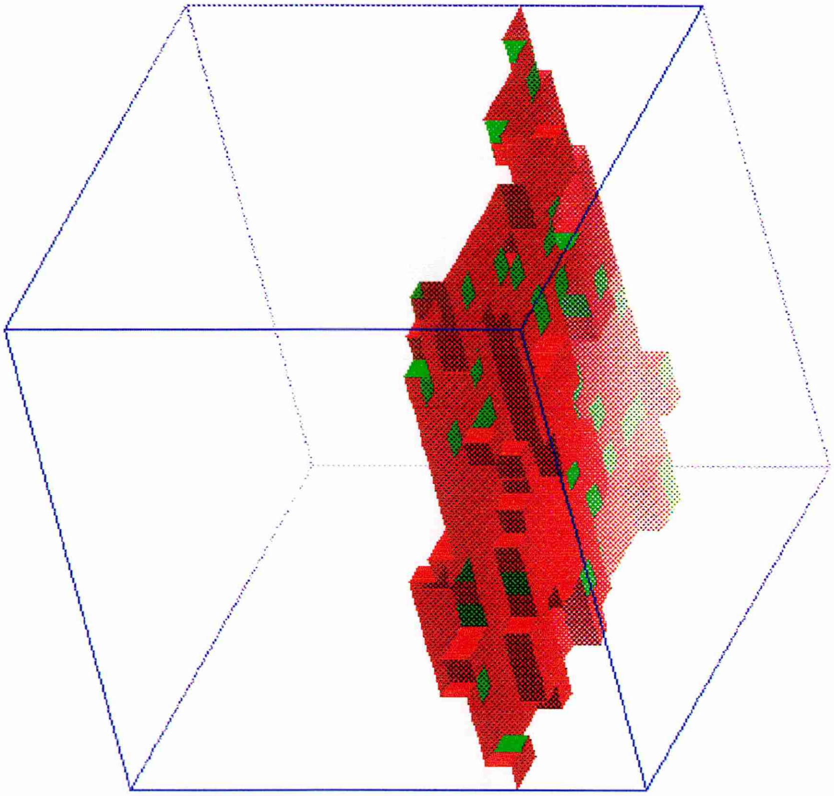

(minimal surface of) main crack

Figure 8.3: Damage in $20 \times 20 \times 20$ system with $\Phi = 20\%$.

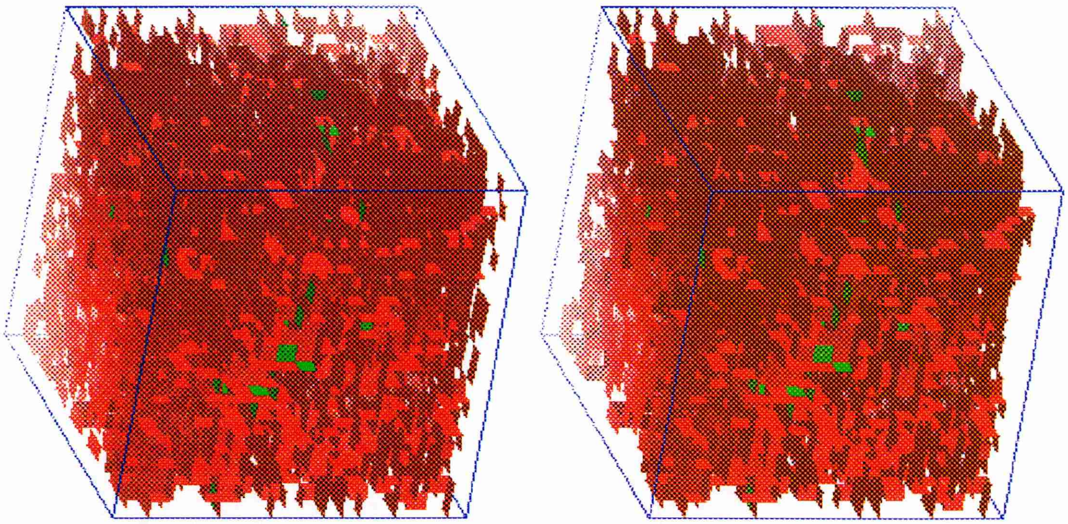

all broken bonds **broken bonds joined to main crack**

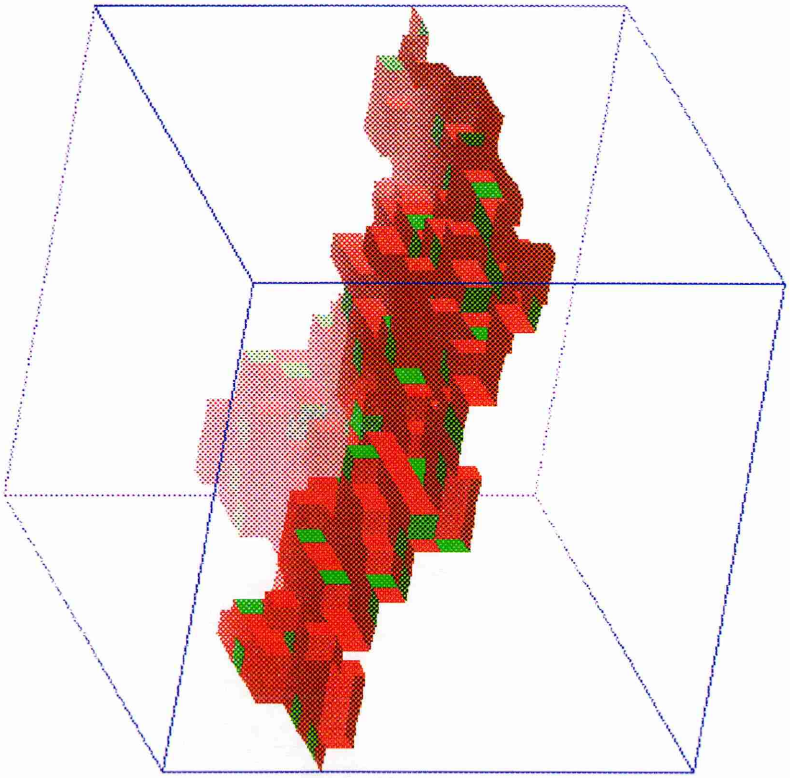

(minimal surface of) main crack

Figure 8.4: Damage in $20 \times 20 \times 20$ system with $\Phi = 40\%$.

8.1.2 Single particle systems

The model used can also be applied to a different type of simulation based on rubber macro-particles, i.e. large volumes of connected rubber bonds. The results illustrated in Fig 8.5 and Fig 8.6 are for single macro-particle simulations. The rubber bonds' mechanical characteristics are $k_r = 0.1$ and $F_r = 8$. The applied force was $F = 2$ in the first and $F = 1$ in the second.

In Fig 8.5 ($F = 2$), view *a* shows the main crack damage situation a few steps before the material's failure. The damage has first formed an equatorial plane, perpendicular to the applied force, around the rubber particle. View *b* shows the complete failure situation, the crack has propagated through the core of the particle. View *c* presents the rubber particle with the equatorial crack.

In Fig 8.6 ($F = 1$), view *a* shows the damage situation some steps before the material's failure. Here again the main crack is formed in the particle's equatorial region. But, as shown in the front (*b*) and rear (*c*) views, the crack then develops in a different way than in the greater force simulation. Indeed, instead of breaking through the rubber particle, the main crack progresses around the spherical shell of the particle; this damage is mainly located in the region of the polymer matrix lying just outside the rubber particle, with a small amount of rubber breaking at the very end of the simulation. View *d* shows the rear view cavity filled with the almost undamaged rubber particle.

From these two representative simulations' results, it appears that, when nearing a rubber particle, the main crack develops in the particle's equatorial polymer region, but then two modes of crack propagation can be differentiated. For larger applied forces, the main crack splits the particle through its core, whereas, for smaller forces, the crack avoids the particle, finding its way around it and causing it to debond from one part of the polymer matrix.

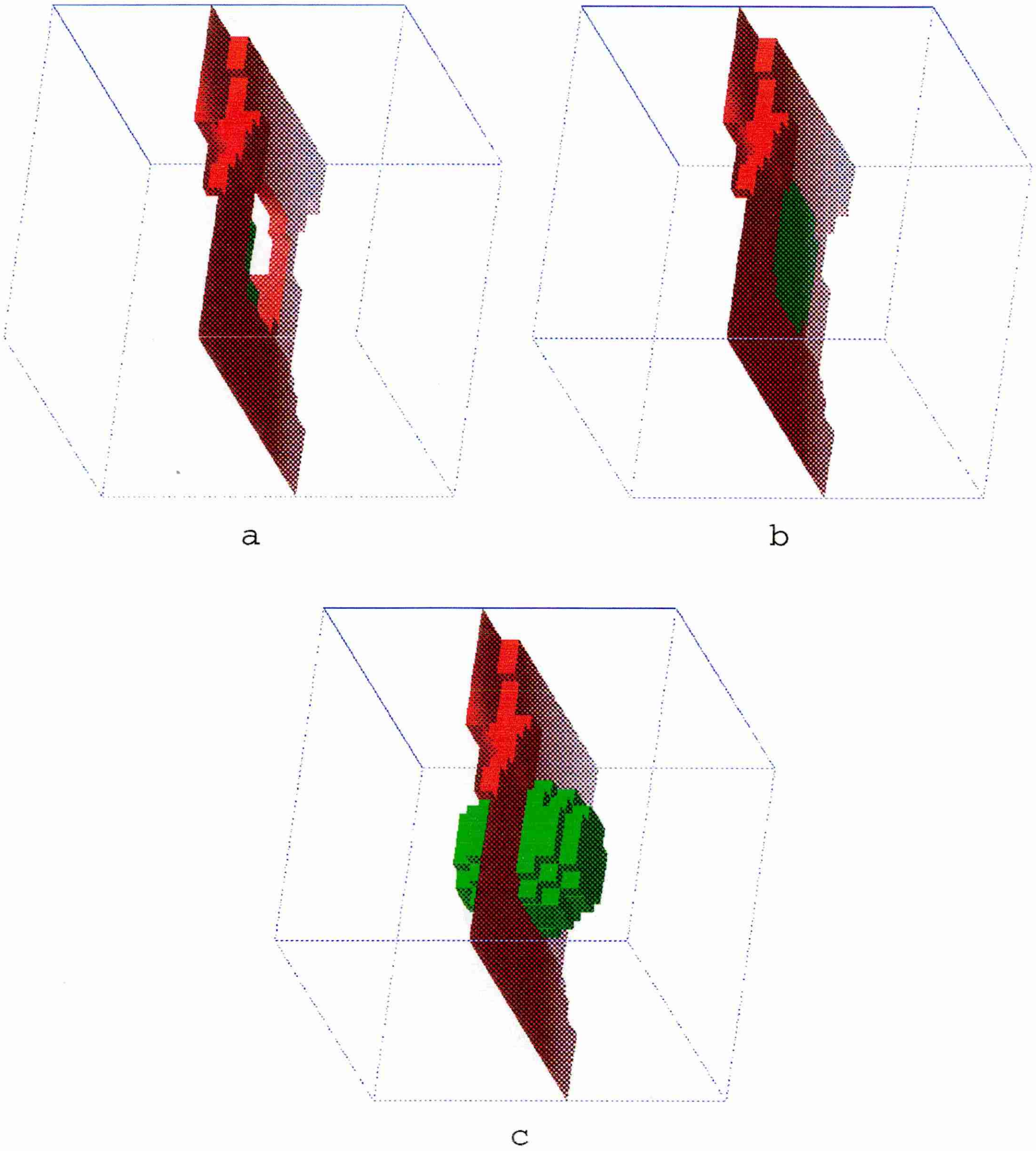

Figure 8.5: Main crack near a single particle in a $20 \times 20 \times 20$ system and applied force $F = 2$. a) few steps before failure, b) at the material's failure point, c) with rubber particle in place.

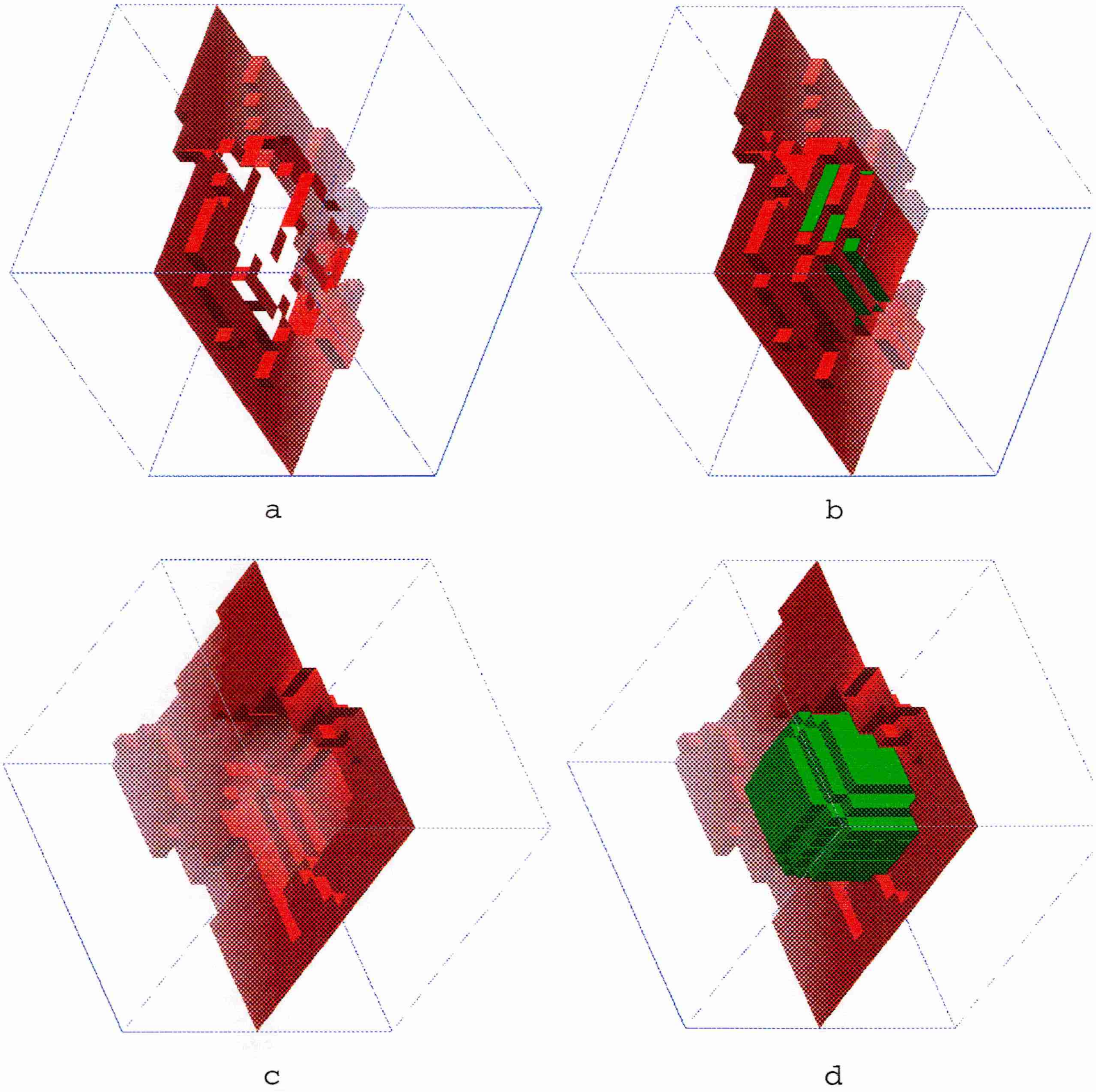

Figure 8.6: Main crack near a single particle in a $20 \times 20 \times 20$ system and applied force $F = 1$. a) few steps before failure, b) front view at the material's failure point, c) rear view at the material's failure point, d) rear view with rubber particle in place.

8.2 2D systems

For $2D$ systems, it is informative to visualise the system-wide stress maps. Only the stress sustained by the x-bonds is displayed. The stress values are colour-coded, red for polymer bonds, green for rubber; the paler the colour, the less stress the bond experiences.

8.2.1 Single particle

We present here the damage and stress maps of simulations of macro-systems containing a single rubber particle of radius 25 embedded in a 100×100 polymer matrix. The rubber bonds' mechanical characteristics are $k_r = 0.1$ and $F_r = 8$. The initial stress situation of such a system is shown in Fig 8.7. The particle's equatorial surrounding region along the y axis (perpendicular to the external applied force) is subjected to the maximum stress, whereas that along the x axis (parallel to the external applied force) is relatively unstressed.

Fig 8.8 and Fig 8.9 shows the damage (left) and stress (right) evolution during the crack growth when an external force (respectively $F = 1.7$ and $F = 1.9$) is applied to the system. The damage is denser in the top and bottom equatorial regions, where the stress is initially the highest (this is even more obvious for $F = 1.9$). Crazes develop (views $a.1$) with a high stress concentration at the craze tips (views $a.2$). When the main craze is totally opened (views $b.1$), the rubber particle pins the two crack surfaces and experiences stress increases whereas the crack-neighbouring polymer regions see a stress relief (views $b.2$). On can also notice the relative stress increase in the left and right equatorial regions, which were previously unstressed. Towards the end of the simulations, the behaviours of the two systems differ. Two modes of material failure can be observed. The lower force system demonstrates particle debonding in which the crack develops around the outer perimeter of the

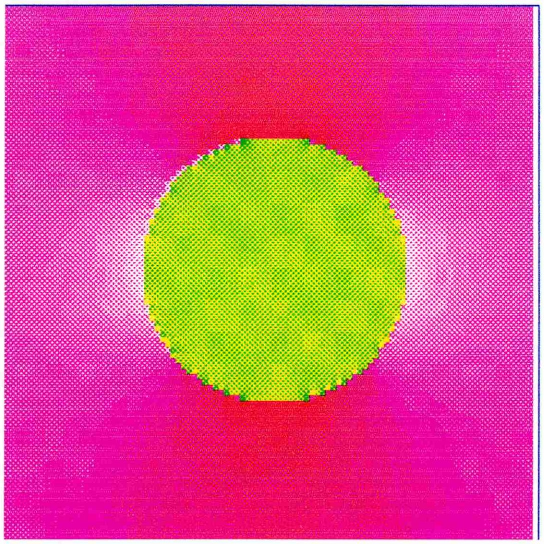

Figure 8.7: Stress field around a single rubber particle in a 100 × 100 system

particle from both top and bottom craze tips (Fig 8.8, view *c*.1). The two tips move towards each other, inducing high stress in the inter-tip zone, and leaving stress-relieved regions behind them (Fig 8.8, view *c*.2). On the other hand, the higher force system illustrates a different rubber failure mode; instead of moving around the particle, the crack develops through its core, splitting the particle in two (Fig 8.9, view *c*.1). The undamaged part of the particle experiences a stress increase from the crack tip forwards (Fig 8.9, view *c*.2).

Fig 8.10 shows the final crack paths for these two simulations.

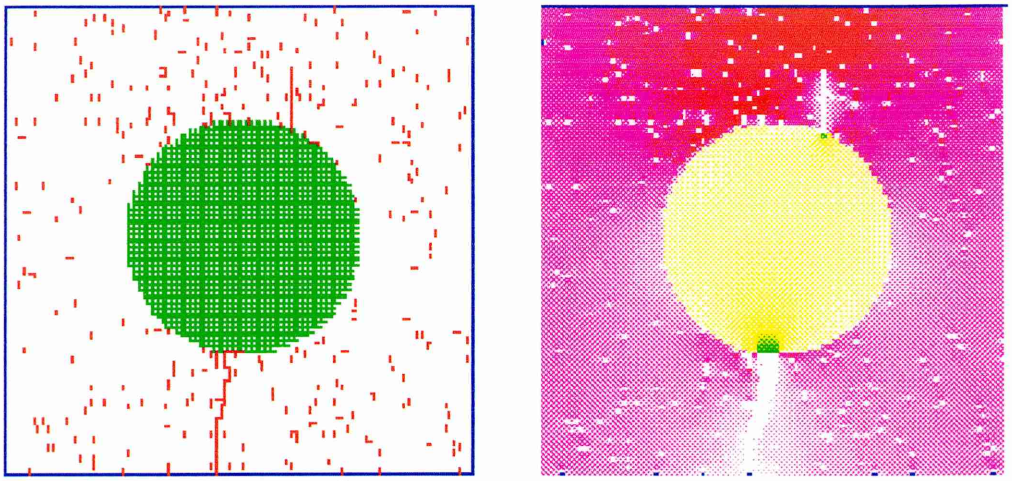

a.1) damage @ #350 a.2) stress @ #350

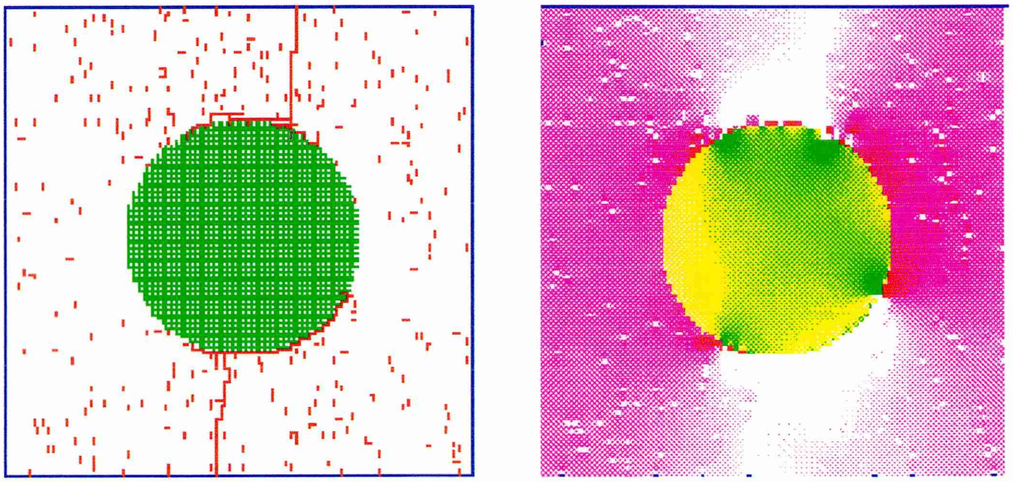

b.1) damage @ #450 b.2) stress @ #450

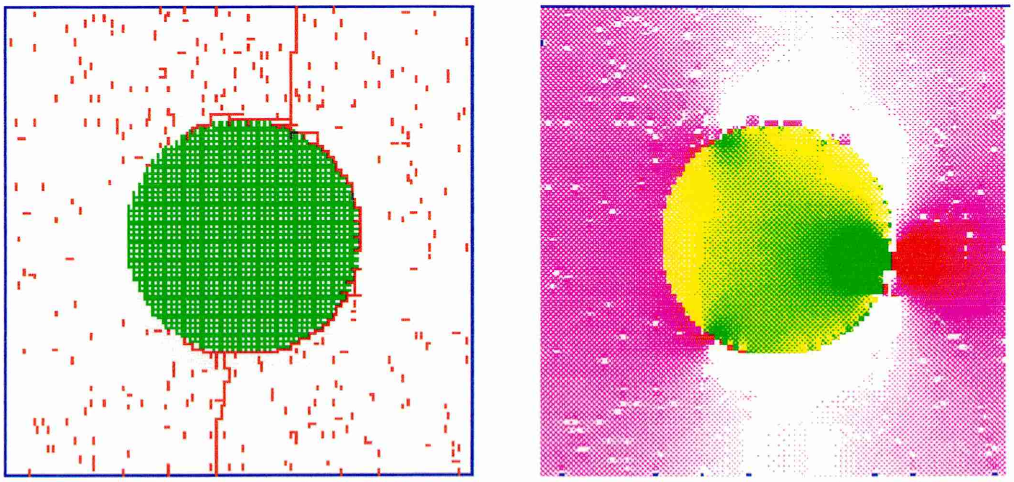

c.1) damage @ #500 c.2) stress @ #500

Figure 8.8: Damage and stress evolution in a single particle 100×100 system and applied force $F = 1.7$

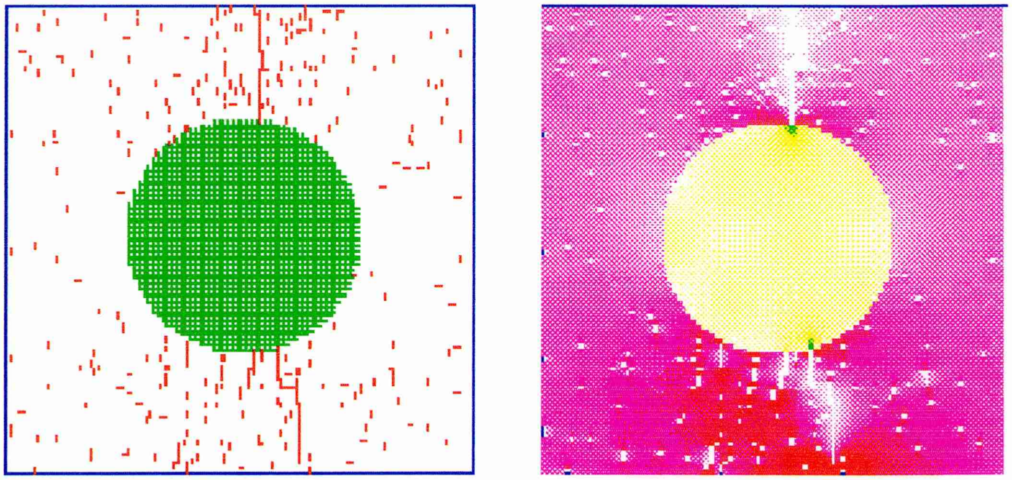

a.1) damage @ #350   a.2) stress @ #350

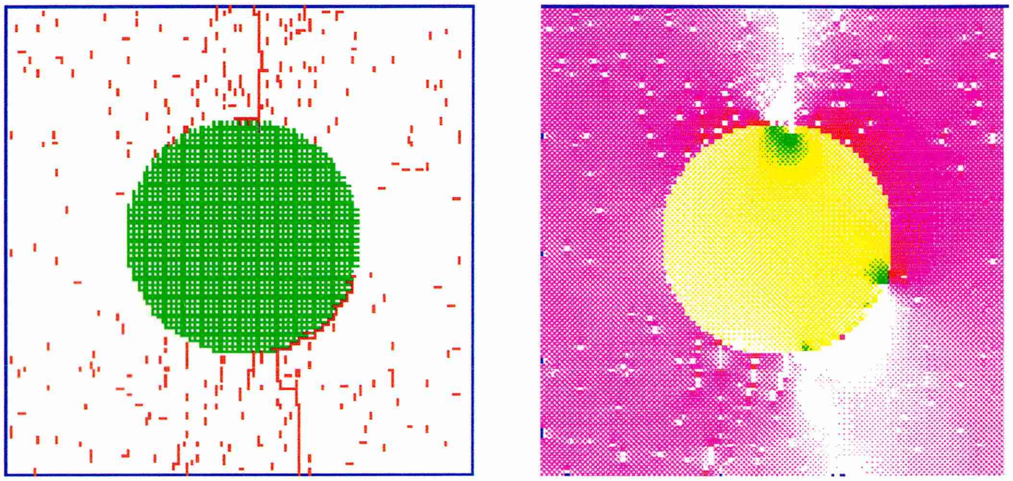

b.1) damage @ #400   b.2) stress @ #400

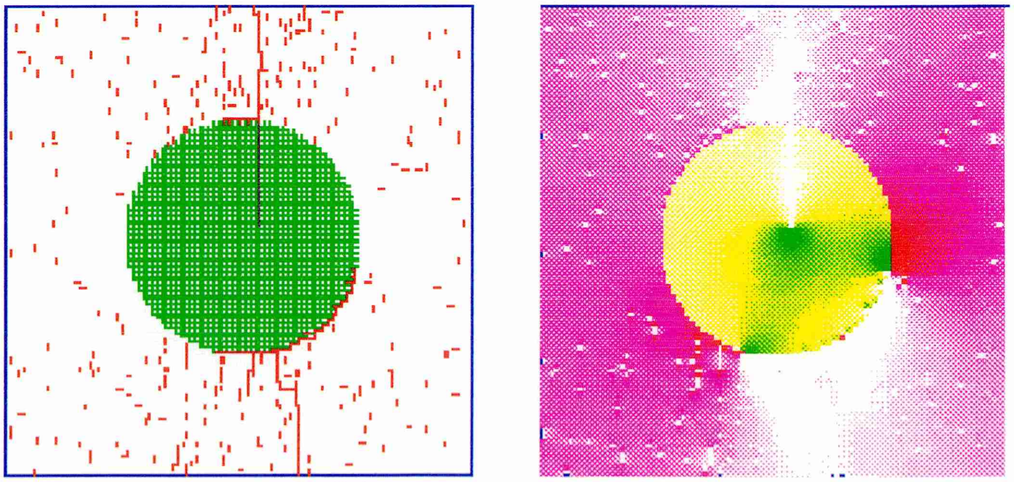

c.1) damage @ #450   c.2) stress @ #450

Figure 8.9: Damage and stress evolution in a single particle 100 × 100 system and applied force $F = 1.9$

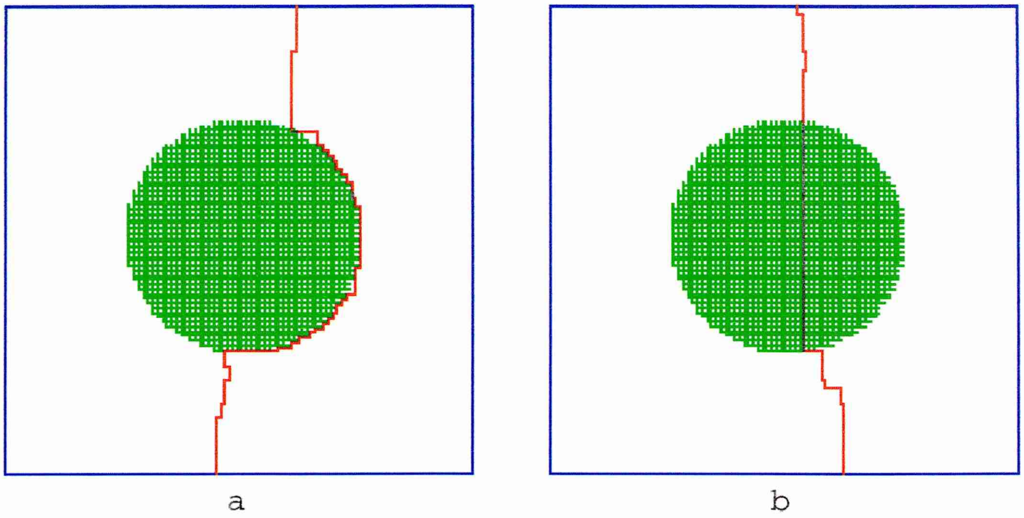

Figure 8.10: Final crack paths for the simulations shown in Fig 8.8 and Fig 8.9 : a) $F = 1.7$, b) $F = 1.7$.

8.2.2 Regularly-placed particles

Fig 8.12 presents the evolution of the damage and the stress in a 110×110 system containing rubber particles arranged on a grid. The rubber bonds' mechanical characteristics are $k_r = 0.1$ and $F_r = 8$, and the applied external force is $F = 2$. At the begining of the simulation, before any damage, the stress situation is as illustrated in Fig 8.11. The stress is equally distributed between the particles and, as in the single particle systems, the particles' equatorial surrounding regions along the y axis (perpendicular to the external applied force) are subjected to the maximum stress, whereas those along the x axis (parallel to the external applied force) are relatively unstressed. At about the material's mid-life (in terms of simulation steps), crazes appear around some rubber particles (Fig 8.12, view $a.1$), inducing high stress spots at their rubber and polymer tips (view $a.2$). View $b.1$ shows the damage situation when some of these crazes have opened and joined particles; one of them has developed into an almost complete rubber-pinned crack. From view $b.2$, one can observe that this pinning results in a stress transfer from the surrounding polymer matrix to the pinning rubber particles, the polymer regions near the craze line are now in

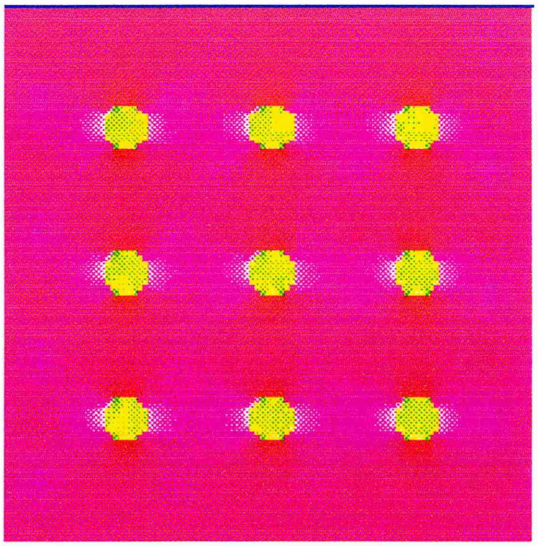

Figure 8.11: Stress map for an undamaged 110×110 system with 9 regularly-placed rubber particles

a very low stress state whereas the previously weakly stressed particles experience a significant stress increase. As the crack progresses (view *c*.1), particles debond and a crack branch develops. The crack-damaged regions become almost stress-free and the stress is concentrated on the very localised undamaged rubber and polymer regions along the crack line (view *c*.2). The final full branched and main cracks are presented in Fig 8.13.

This simulation illustrates clearly the stress transfer which takes place in the material when cracks develop. As cracks grow, the stress is gradually transfered from the initially high-stressed inter-particle polymer regions to the crack tips and then to the initially low-stressed particles along the crack lines.

8.2.3 Randomly-placed particles

Fig 8.14, 8.15 and 8.16 illustrate the evolution of the damage in a 100×100 macro-system containing respectively 20, 37 and 70 randomly-placed rubber particles of radius 3, which represents rubber proportions of about 7%, 14% and 26%. The

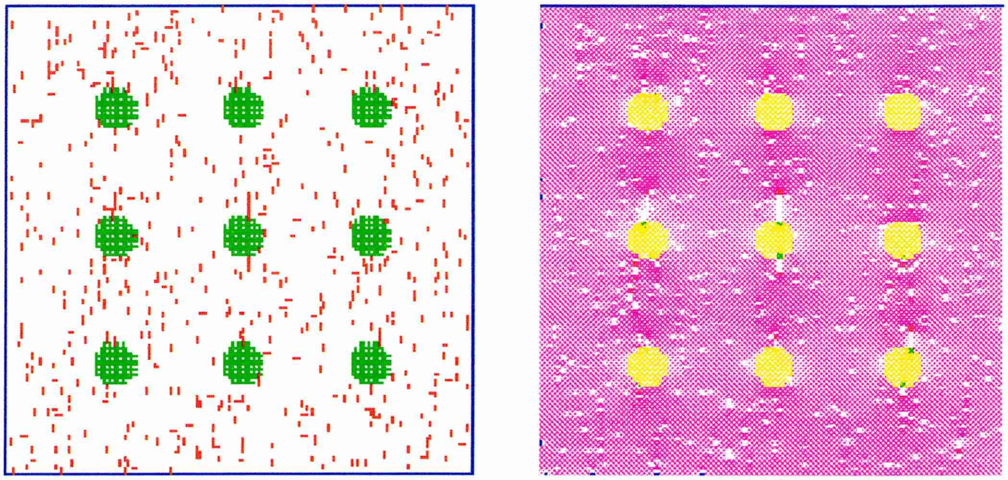

a.1) damage @ #600 a.2) stress @ #600

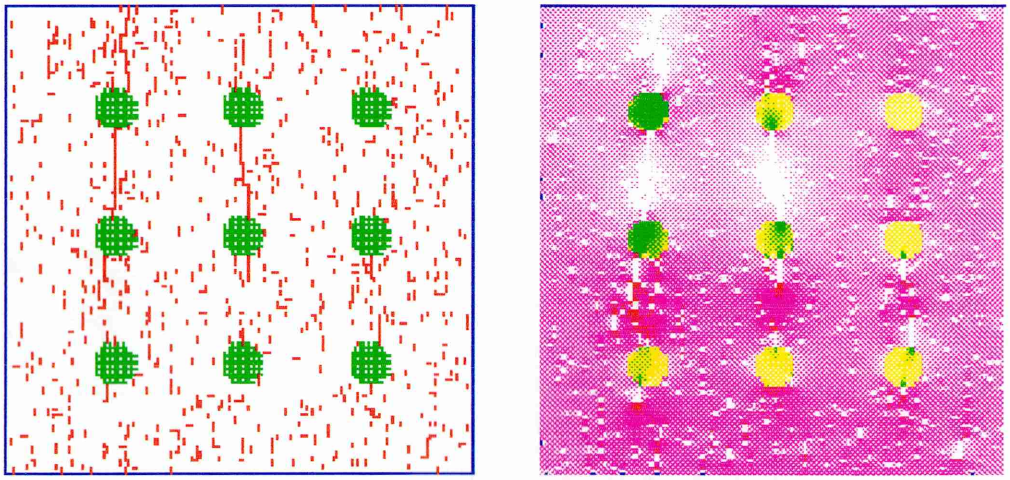

b.1) damage @ #900 b.2) stress @ #900

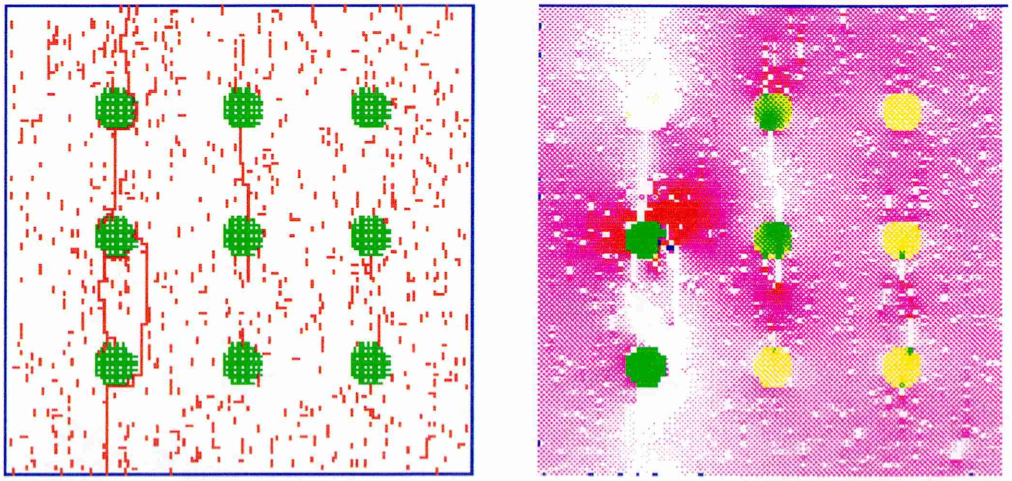

c.1) damage @ #1000 c.2) stress @ #1000

Figure 8.12: Damage and stress evolution in a 110 × 110 system with 9 regularly-placed rubber particles

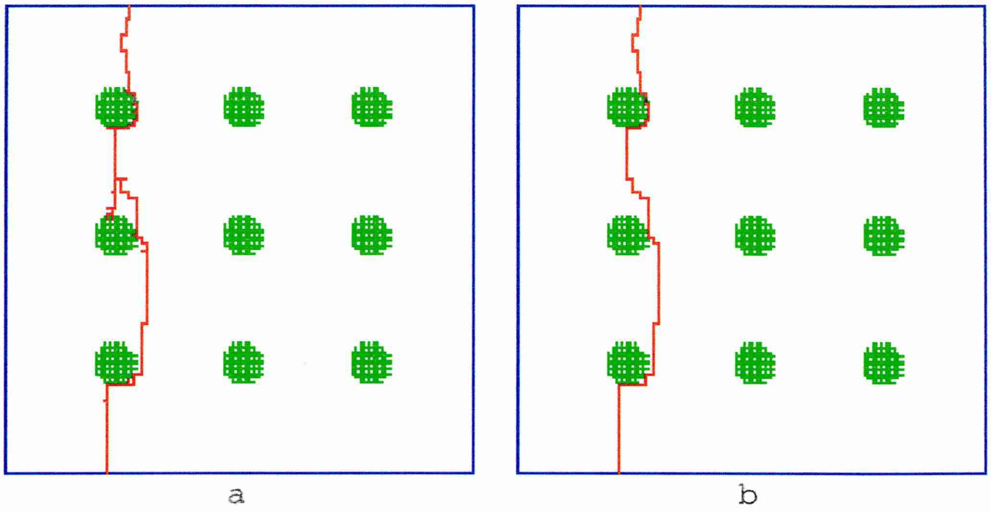

Figure 8.13: Branched (a) and main (b) crack in a 110×110 system with 9 regularly-placed rubber particles

rubber bonds' mechanical characteristics are $k_r = 0.1$ and $F_r = 8$ and the applied external force is $F = 2$.

Views *a* show the damage situation at an early stage of the breaking process. The damage looks well-distributed throughout the bulk, with a higher local damage density in the top and bottom regions of the rubber particles. Where the inter-particle distance is short, some of these regions of local damage have connected to form short rubber-joinning crazes. As a general observation, crazes seem more likely to form and to develop where the particle density is important (short inter-particle distance) than around isolated particles. This tendency for the craze nucleation to be associated with particle clusters has also been observed in real material [16].

Views *b* presents the material when crazes have developed further. The craze growth leads the material to a stage where a series of crazes have connected to form rubber-bridged cracks (Fig 8.14.c, 8.15.b and 8.16.b). From this point, the damage proceeds with some formation of crack branches (Fig 8.15.c), or parallel cracks (Fig 8.16.c). Views *d* and *f* show the different systems at the material's failure point. Two modes of rubber failure can be observed along the main cracks : particle debonding (particles being pulled out from one half of the polymer matrix), and particle splitting (the crack goes through the particle's core). On can also notice another way in which the crack deals with particles : crack reflection. In this, the crack hits the surface of the particle and is reflected back into the matrix. Particle splitting does not occur in the low rubber density (Fig 8.14.f). Views *e* present the main cracks with their branched developments; the more rubber particles in the system, the more branched the main crack seems to be. For higher rubber concentrations, the crack has more options for its development. All of these compete, thus delaying and hindering the creation of a single main crack. On the other hand, the 20 particle system exhibits a single unbranched main crack and takes less time (in terms of number of broken bonds) to fail.

To summarize, these simulations exhibit the importance of the rubber bridging mechanism when it comes to extend the material's life. From the point when this phenomenon occurs, the damage period can be extended through the formation of either crack branches or parallel cracks. In the case of the 70 particle system (Fig 8.16), the number of broken bonds has almost been doubled through these two mechanisms (rubber bridging appears at step #500 and the material fails at step #943). These simulations also highlight the three possible consequences of particle-crack interaction : debonding, splitting and crack reflection.

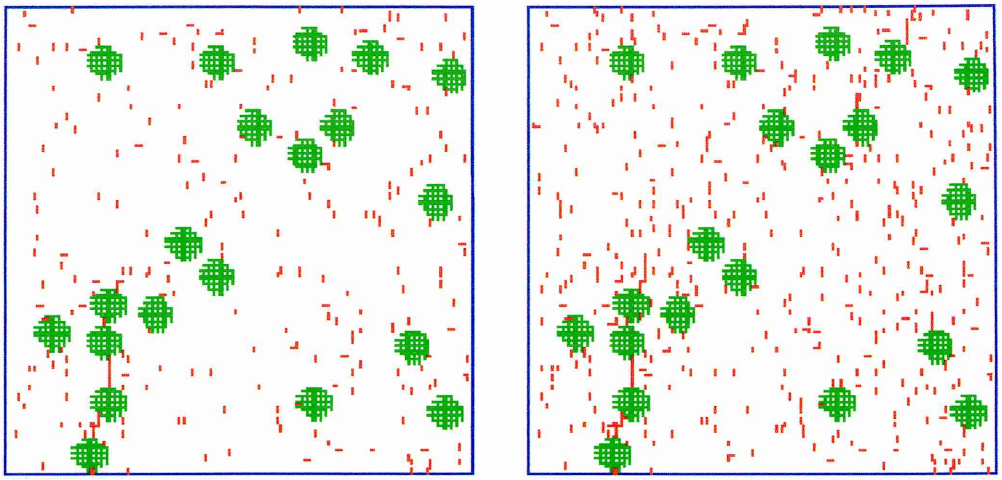

a) step #250 b) step #500

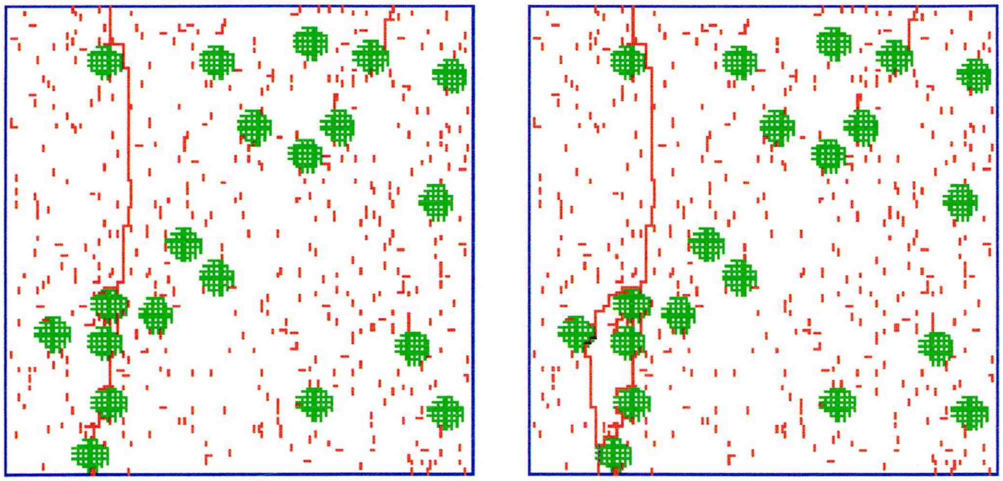

c) step #600 d) step #660

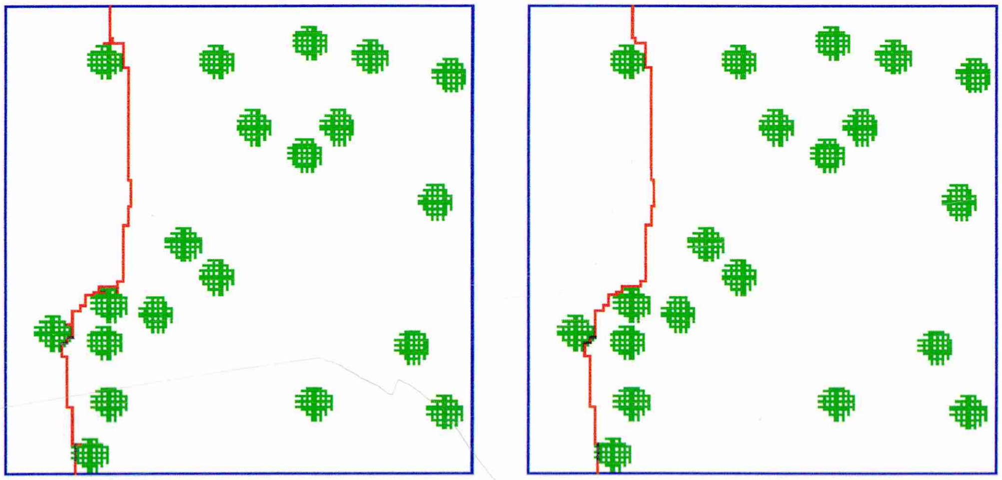

e) branched damage f) main crack

Figure 8.14: Damage evolution in a 100 × 100 system with 20 randomly-placed rubber particles ($\Phi \approx 7\%$)

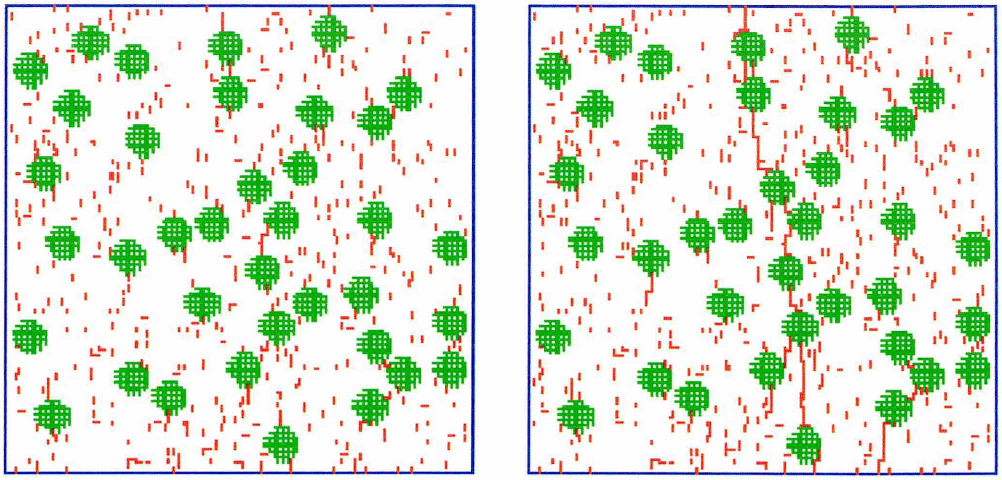

a) step #500 b) step #650

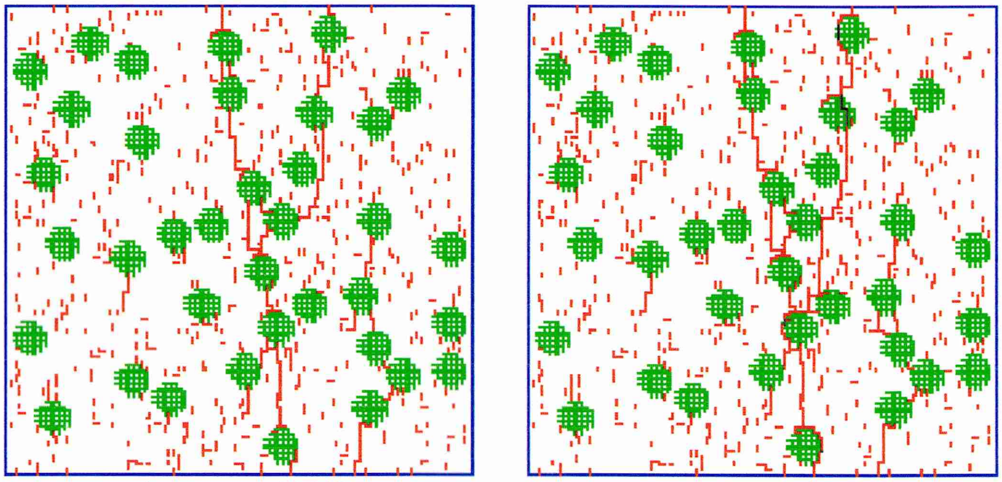

c) step #750 d) step #873

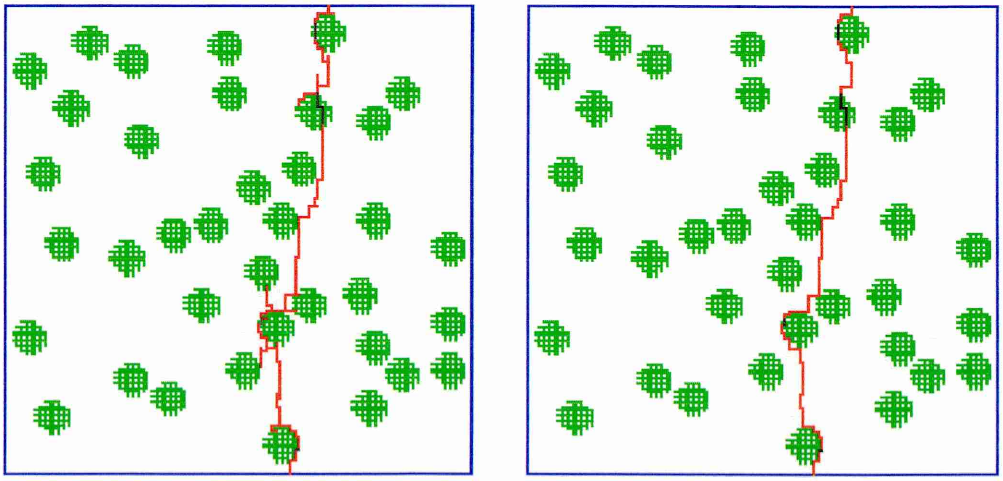

e) branched damage f) main crack

Figure 8.15: Damage evolution in a 100 × 100 system with 37 randomly-placed rubber particles ($\Phi \approx 14\%$)

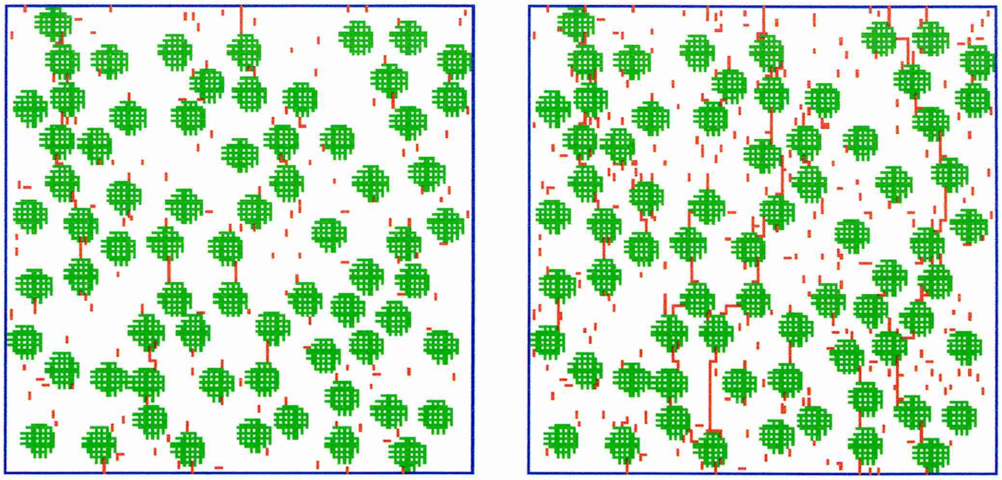

a) step #200 b) step #500

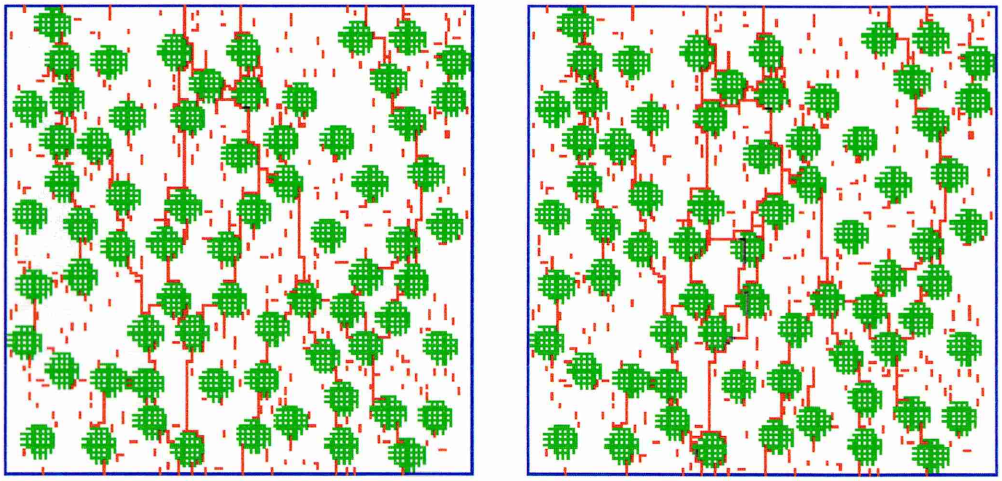

c) step #850 d) step #943

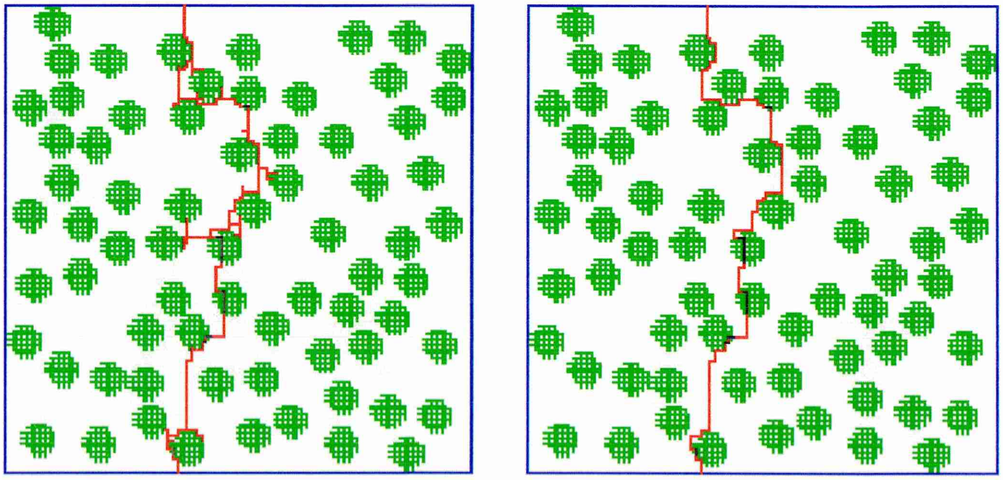

e) branched damage f) main crack

Figure 8.16: Damage evolution in a 100 × 100 system with 70 randomly-placed rubber particles ($\Phi \approx 26\%$)

Chapter 9

Conclusion and further work

9.1 Conclusion

The model developed in this work has proved to be realisable and efficient in modelling the complex mechanisms involved in fracture propagation in brittle composite materials. Its 2D and 3D implementations have shown that the best numerical method to solve the large sparse linear system which arises in this heterogeneous context is the *Conjugate Gradient.* The model-based simulations carried out have given results which have been found to be consistent with related available experimental works on real rubber-toughened polymers. Futhermore, these results have provided information on the stress distribution during the damage development and given insight into the fracture and toughening mechanisms which place in these materials. These results fall in three categories : damage results, stress results and visual results.

9.1.1 Damage

In the model, we have defined the damage d as the total number of bonds broken during the material's failure. Although this parameter is a crude measure of the energy dissipated, it gives a good idea of the trend of the material's toughness. We have studied the variations of this parameter with the rubber loading Φ and have found that the effects of the rubber concentration on the damage can be divided into four distinct regions as illustrated in Fig 9.1. The toughness of the material has been found to increase steadily with rubber loading (region **B**) until reaching a plateau (region **C**). Further addition of rubber does not improve the toughness and, if carried to the limit, the model shows a sharp decrease in toughness (region **D**). This trend is supported by results on real composite polymers. The weakening phenomenon observed for very low rubber fractions (region **A**) is still to be compared with experimental data, which are not available at present.

It has been shown that the span of these four regions is dependent on the components' mechanical properties (elasticity and force threshold). This work has also shown that the material toughness is reduced by clustering of rubber particles; the greatest toughness has been found for homogeneous rubber distributions.

9.1.2 Stress

We have studied the evolution of the maximum stress and related parameters as damage progresses in the modelled material. It appears that the stress develops in four distinct regimes as presented schematically in Fig 9.2 (this figure is similar to Fig 7.35 presented earlier, it is repeated here for convenience). In the early stage of the breaking process, the stress builds up slowly as widespread damage occurs throughout the material and crazes initiate around the rubber bonds (regime **A**). As the damage increases in the system, the stress evolution becomes chaotic (regime **B**), indicating sudden opening and connecting of some crazes. When this craze

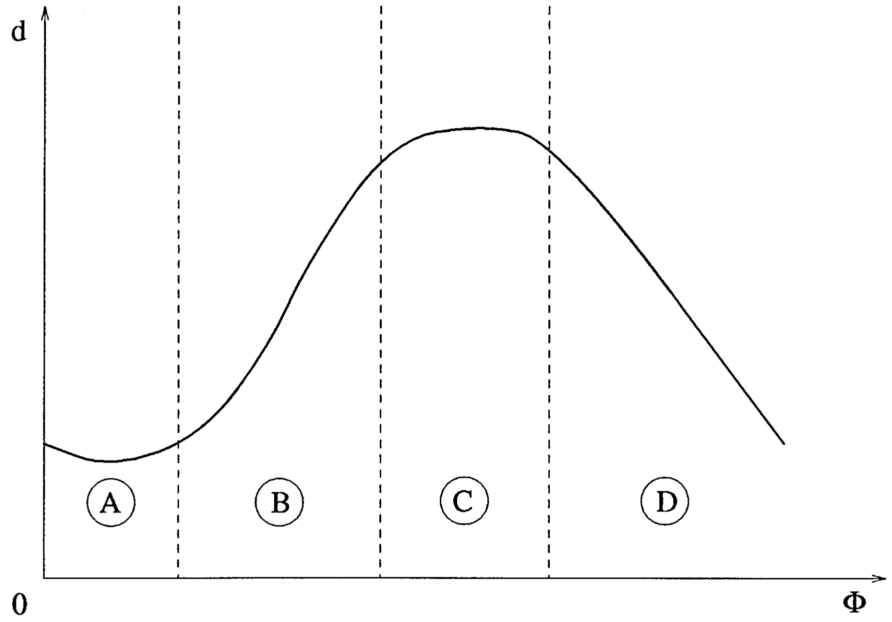

Figure 9.1: Schematic representation of the 4 damage regions.

development phase stabilises, the maximum stress evolution does likewise (regime **C**). The maximum stress shifts from polymer to rubber bonds, implying the rubber-bridging of certain well-developed crazes. During this regime, widespread damage takes place again. When the stress in some crack-bridging rubber bonds reaches the failure threshold, they break, avalanching the stress through the remaining bonds which also break, resulting in the formation of a main crack and the material's breakdown (regime **D**). The relative importance of these four regimes is altered when the rubber loading or the material components' characteristics are changed.

The results have exhibited two major toughnening mechanisms : extensive crazing of the polymer matrix and rubber-bridging of the cracks, related to regime **B** and regime **C**, respectively. It appears that the crazing effect is not dependent on the rubber's force threshold F_r, but is increased by decreasing the value of the rubber's elastic modulus k_r. On the other hand, the rubber-bridging mechanism seems to be improved for high values of F_r, but appears not to be dependent on k_r. The results have also shown the dependence of those two mechanisms on the rubber loading Φ. Rubber-bridging is conspicuously improved for high values of Φ; one can also observe that extensive crazing increases with rubber loading up to a point where it regresses (for $\Phi > 50\%$).

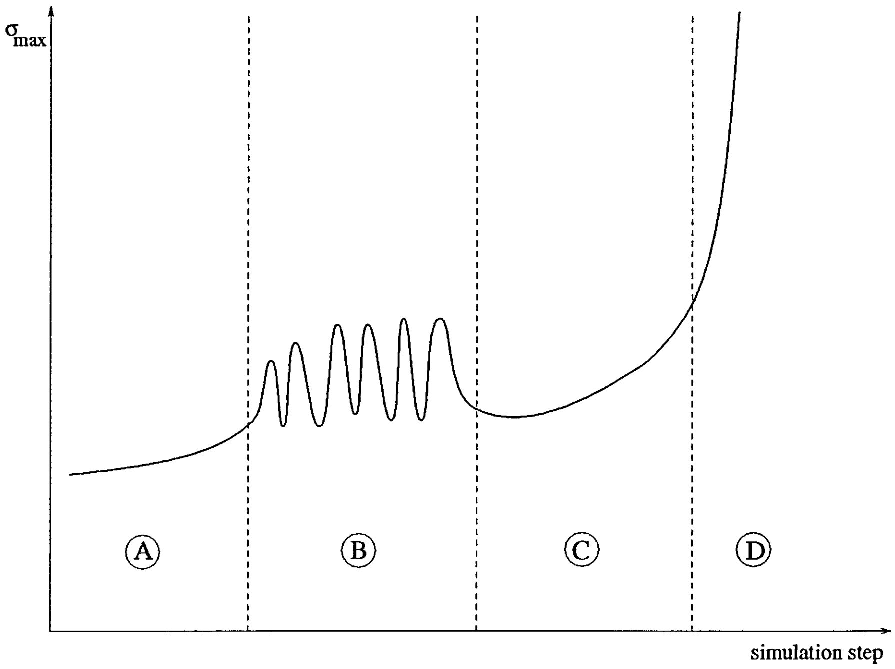

Figure 9.2: Schematic representation of the 4 stress regimes.

9.1.3 Visualisation

The visual results have given a further insight into the damage evolution in the modelled material. They have, in particular, confirmed the importance of crazing and rubber-bridging as toughening mechanisms. They also have exhibited three possible crack-particle interactions : particle debonding, particle splitting and crack deflection.

The results presented in this thesis suggest that the best material toughness improvements can be achieve with low values of the rubber elastic modulus k_r, high values of the rubber force threshold F_r and a moderate rubber concentration Φ, not greater than 50% in most cases.

9.2 Further work

Although the features exhibited by the model went beyond initial expectations, the model still lacks some of the properties of real systems, the most noticeable of which is the treatment of dynamics. The deformation mechanisms in materials under impact conditions are certainly dominated by dynamic considerations, such as, for instance, the crack tip velocity. Futhermore, impact fracture phenomena occur on very short time scales and the system does not usually have enough time to equilibriate while the crack is growing, as is assumed in this static model. Futher improvements should concern the implementation of dynamic aspects of impact crack problems.

We have pointed out that, due to its restriction to purely elastic bonds, this model cannot be used to study polymer composites whose polymer matrix is prone to plastic deformation mechanisms, such as shear yielding (*eg* epoxies, nylons, etc.). To extend the model to this kind of material, one should introduce viscoelastic behaviour at the bond level. However, this would raise the problem of the lattice's suitability to support the very large elongation differences existing between bonds which have passed their yielding point and those which have not.

On the computational side, as the most computationally expensive part of the program is the solving of a huge linear system at every simulation step, one could improve the chosen numerical method's efficiency. The convergence rate of the *Conjugate Gradient* (CG) method can indeed be improved. In the following linear system

$$\mathbf{A}.\mathbf{x} = \mathbf{b}$$

the "closer" the matrix **A** is to the identity matrix, the faster the CG method coverges. This suggests applying it to the *preconditioned* form :

$$\left(\mathbf{M}^{-1}\mathbf{A}\right)\mathbf{x} = \mathbf{M}^{-1}\mathbf{b}$$

The matrix $\mathbf{M}$ is called a *preconditioner.* If it is possible to find a matrix $\mathbf{M}$ "close" to $\mathbf{A}$, then $\mathbf{M}^{-1}\mathbf{A}$ will be "close" to $\mathbf{1}$, allowing the algorithm to converge in fewer steps. Different *Preconditioned Conjugate Gradient* methods (PCG) exist [82], including the *truncated series preconditioning* and the *incomplete-Cholesky conjugate gradient* [83] methods.

Another way to speed up the execution of simulation is to share the overall computational task among a set of different processors. Here, again, the most useful part to rewrite in a parallel form is the solving of the linear system. The degree of parallelism achievable using pure PCG methods is quite poor, but ways can be found to greatly increase the parallelism suitability of PCG [84, 85].

Bibliography

[1] Kinloch, A.J. & Young, R.J. (1983), *Fracture Behavior of Polymers*, Elsevier Applied Science, London

[2] Bucknall, C.B. (1977), *Toughened plastics*, Applied Science Publishers Ltd., London

[3] Kambour, R.P. & Russell, D.R. (1971), *Polymer*, **12**, p237

[4] Sjoerdsma, S.D., Dekkers, M.E.J. & Heikens, D. (1982). *J. Mater. Sci.*, **17**, p2605

[5] Hayashi, K., Morioka, T. & Toki, S. (1993) *J. Appl. Polym. Sci.*, **48**, p411

[6] Kato, K. (1967). *Polym. Eng. Sci.*, **7**, p38

[7] Kinloch, A.J., Shaw, S.J, Tod, D.A & Hunston, D.L. (1983). *Polymer*, **24**, p1341

[8] Newman, S. & Strella, S. (1965), *J. Appl. Polym. Sci.*, **9**, p2297

[9] Goodier, J.N. (1993). *Trans. Am. Soc. Mech. Engs.*, **5**, p39

[10] Broutman, L.J. & Panizza, G. (1971), *Int. J. Polym. Mater.*, **1**, p95

[11] Argarwal, B.D. & Broutman, L.J. (1974), *Fibre Sci Tech.*, **7**, p63

[12] Guild, F.J. & Kinloch, A.J. (1994), *J. Mater. Sci. Lett.*, **13**, p629

[13] Schemer, B., Kuriyama, T. & Friedich, K. (1995). *J. Mater. Sci. Lett.*, **14**, p660

[14] Bagheri, R. & Pearson, R.A. (1996), *Polymer*, **20**, p4529

[15] Arminda, M.L. & Rein, J.M. (1995), *Macromolecules*, **28**, p5841

[16] Plummer, C.J.G., Beguelin, P. & Kausch, H.H. (1996). *Polymer*, **37**, p7

[17] Muratoglu, O.K. & Weinberg, M. (1995). *Polymer*, **36**, p4771

[18] Yee, A.F. & Pearson, R.A. (1986), *J. Mater. Sci.*, **21**, p2462

[19] Huang, Y. & Kinloch, A.J. (1992), *J. Mat. Sci.*, **27**, p2753

[20] Huang, Y. & Kinloch, A.J. (1992), *J. Mat. Sci.*, **27**, p2763

[21] Huang, Y. & Kinloch, A.J. (1992), *Polymer*, **33**, p5338

[22] Guild, F.J. & Kinloch, A.J. (1995), *J. Mater. Sci.*, **30**, p1689

[23] Yee, A.F., Li, D. & Xiaowei, L. (1993), *J. Mater. Sci.*, **28**, p6392

[24] Li, D., Yee, A.F., Powers, K.W., Wang, H.C. & Yu, T.C. (1993), *Polymer*, **34**, p4471

[25] Donald, A.M. & Kramer, E.J. (1982), *J. Appl. Polym. Sci.*, **27**, p3729

[26] Bubeck, R.A., Buckley, D.J., Kramer, E.J. & Brown, H. (1991), *J. Mater. Sci.*, **26**, p6249

[27] Borggreve, R.J.M., Gaymans, R.J., Schuijer, J. & Ingen Housz, J.F, (1987). *Polymer*, **28**, p1489

[28] Dompas, D. & Groeninckx, G. (1994). *Polymer*, **35**, p4743

[29] Wu, S. (1985). *Polymer*, **26**, p1855

[30] Wu, S. (1988). *J. Appl. Polym. Sci.*, **35**, p549

[31] Wu, S. (1992). *Polym. Int.*, **29**, p229

[32] Lazzeri, A. & Bucknall, C.B. (1993), *J. Mater. Sci.*, **28**, p6799

[33] Lazzeri, A. & Bucknall, C.B. (1995), *Polymer*, **36**, p2895

[34] Yee, A.F. & Pearson, R.A. (1989), in *Fractography and failure mechanisms of polymers and composites*, Elsevier Applied Science, London

[35] Breuer, H., Haaf, F. & Stabenow, J. (1977), *J. Macromol. Sci.-Phys.*, **B14**, p387

[36] Speroni, F., Castoldi, E., Fabbri, P. & Casiraghi, T. (1989), *J. Mater. Sci.*, **24**, p2165

[37] Bucknall, C.B., Karpodinis, A. & Zhang, X.C. (1994), *J. Mater. Sci.*, **29**, p3377

[38] Sjoerdsma, S.D. (1989). *Polym. Commun.*, **30**, p106

[39] He, C., Butler, M.F. & Donald, A.M. (1997), in conference papers of *the 10th International Conference on Deformation, Yield and Fracture of Polymers*, Cambridge

[40] Jansen, B.J.P., Rastogi, S., Meijer, H.E.H & Lemstra, P.J. (1997), in conference papers of *the 10th International Conference on Deformation, Yield and Fracture of Polymers*, Cambridge

[41] Bucknall, C.B., Partrige, I.K. & Ward, M.V. (1984). *J. Mater. Sci.*, **19**, p2064

[42] Gloagen, J.M., Lefebvre, J.M. & Wrotecki, C. (1993). *Polymer.*, **34**, p443

[43] Julien, O., Beguelin, Ph., Monnerie, L. & Kausch, H.H. (1996). *?*, **?**, p233

[44] Beguelin, Ph., (1996). *Thèse de Doctorat*, Ecole Polytechnique Fédérale de Lausanne.

[45] Barwick, A.J, Chisholm, M.S, Fraser I.M & Moore, D.R, (1994). *ICI internal report.*

[46] *Rubber-toughened plastics*, (1989). Edited by Riew C.K., Advances in Chemistry series 222, ACS, Washington DC.

[47] Jung, W.R & Fraser I.M, (1993). *ICI internal report.*

[48] Bascom, W.D., Moulton, R.J., Riew, C.K. & Siebert, A.R. (1981). *J. Mater. Sci.*, **16**, p2657

[49] Guild, F.J. & Kinloch, A.J. (1994), *J. Mater. Sci. Lett.*, **13**, p629

[50] Davy, P.J. & Guild, F.J. (1988), *Proc. Royal Soc.*, **A148**

[51] Harlow, D.G. & Phoenix, S.L. (1981), *Int. J. of Fract.*, **17**, p601

[52] Leath, P.L. & Duxbury, P.M. (1993), *Physical Review B*, **49**, p14905

[53] Meakin, P. (1991), *Science*, **252**, p226

[54] Ettelaie, R. (1996), *ICI internal report*

[55] Vujosevic, M. & Krajcinovic (1997), *Int. J. Solids Struct.*, **34**, p1105

[56] Weibull, W. (1951), *J. Appl. Mech.*, **18**, p293

[57] Curtin, W.A. & Scher, H. (1992), *Physical Review B*, **45**, p2620

[58] Termonia, Y., Meakin, P. & Smith, P. (1985), *Macromolecules*, **18**, p2246

[59] Termonia, Y. & Meakin, P. (1986), *Nature*, **320**, p429

[60] Termonia Y. & Walsh, D.J. (1989), *J. Mater. Sci.*, **24**, p247

[61] Termonia Y. & Smith, P. (1987), *Macromolecules*, **20**, p835

[62] López-Sancho, M.P., Guinea, F. & Louis, E. (1988), *J. of Phys. A*, **21**, pL1079

[63] Hassold, G.N. & Srolovitz, D.J. (1989), *Phys. Rev. B*, **39**, p9273

[64] Kahng, B., Batrouni, G.G., Redner, S. & De Arcangelis, L. (1988), *Phys. Rev. B*, **37**, p765

[65] De Arcangelis, L. & Herrmann, H.J. (1989), *Phys. Rev. B*, **39**, p2678

[66] Duxbury, P.M., Leath P.L. & Beale, P.D. (1987), *Phys. Rev. B*, **36**, p367

[67] Li, Y.S. & Duxbury, P.M. (1987), *Phys. Rev. B*, **36**, p5411

[68] Karttunen, M.E.J., Niskanen, K.J. & Kaski, K. (1994), *Phys. Rev. B*, **49**, p9453

[69] Mori, Y., Kaneo, K. & Wadachi, M. (1991), *J. Phys. Soc. Jpn.*, **60**, p1591

[70] Taguchi, Y.-H. (1994), *Mat. Sci. Eng.*, **A176**, p295

[71] Shimamura, S. & Kuriyama, K. (1991), *J. Mater. Sci.*, **26**, p6027

[72] Shimamura, S. & Sotoike (1992), *J. Mater. Res.*, **7**, p1286

[73] Shimamura, S. (1994), *Mater. Sci. Eng.*, **A176**, p303

[74] Binder, K. (1984). *Applications of the Monte Carlo method in statistical physics.* Topic in current physics, **36**, Springer, Berlin.

[75] Cleaver, D.J & Allen, M.P. (1991). *Phys. Rev. A*, **43**, p1918

[76] Qian, Y.H., d'Humieres, D., Lallemand, P. (1992), *Europhys. Lett.*, **17**, p479

[77] Griffith, A.A. (1920), *Phil. Trans. Roy. Soc.*, **A221**, p163

[78] Goult, R.J., Hoskins, R.F., Milner, J.A. & Pratt, M.J. (1974)), *Computational Methods in Linear Algebra*, Stanley Thornes, London.

[79] Mandelbrot, B. (1982)), *The Fractal Geometry of Nature*, Freeman, San Francisco.

[80] Fraser, I. (ICI) private communication.

[81] Beguelin, Ph. & Kausch, H.H., Extended abstact for *EURODYMAT, Sept. 22-26, 1997*, Toledo.

[82] Bruaset, A.M. & Tveito, A. (1994), *Bit*, **34**, p177

[83] Manteuffel, T.A. (1980), *Math. of Comp.*, **34**, p473

[84] Seager, M.K. (1986), *Parallel computing*, **3**, p35

[85] Meurant, G. (1987), *Parallel computing*, **5**, p267

Appendix A

Convergence criterion for SOR and CG

A.1 Definitions

The Ostrowski-Reich theorem states that :

if **A** is symetric positive definite and $0 \leq \omega \leq 2$ then the SOR method converges $\forall\, \mathbf{x}^{(0)}$

And a sufficient condition for the CG method to converge is also **A** symmetric positive definite.

An $n \times n$ matrix $\mathbf{A} = (a_{ij})$ is *symmetric* if $\mathbf{A} = \mathbf{A}^T$, or $\forall i, j \;\; a_{ij} = a_{ji}$; and **A** is *positive definite* if $\mathbf{xAx} > 0 \;\; \forall\, \mathbf{x} \neq \mathbf{0}$.

A.2 Demonstration of convergence

Eq. 4.8 is equivalent to :

$$-\mathbf{Kx} = -\mathbf{f} \tag{A.1}$$

In the case where we want to solve Eq. A.1 with either the SOR or the CG methods, we first must make sure that matrix $-\mathbf{K}$ is *symetric positive definite.* From the construction of $\mathbf{K}$ (Eq. 4.9), it is obvious that $-\mathbf{K}$ is *symetric.*

To show next that $-\mathbf{K}$ is *positive definite*, we must prove that :

$$\forall\, \mathbf{x} \neq \mathbf{0},\ \mathbf{x}\,(-\mathbf{K})\,\mathbf{x} > 0 \tag{A.2}$$

With $\mathbf{x} = \{x_i\}$ and $-\mathbf{K} = \{-k_{ij}\}$ Eq. A.2 can be rewritten as follows :

$$\begin{aligned}\mathbf{x}\,(-\mathbf{K})\,\mathbf{x} &= \sum_i x_i \sum_j -k_{ij}x_j \\ &= \sum_i x_i \left[\left(\sum_{j\neq i} -k_{ij}x_j\right) - k_{ii}x_i\right]\end{aligned}$$

We know that the diagonal elements of $\mathbf{K}$ are the sum of the other column (or row) elements : $\forall\, i,\ k_{ii} = -\sum_{j\neq i} k_{ij}$. Thus :

$$\begin{aligned}\mathbf{x}\,(-\mathbf{K})\,\mathbf{x} &= \sum_i x_i \left[\left(\sum_{j\neq i} -k_{ij}x_j\right) + \sum_{j\neq i} k_{ij}x_i\right] \\ &= \sum_i x_i \sum_{j\neq i} k_{ij}\,(x_i - x_j)\end{aligned}$$

If $j = i$, the missing term of the inner sum is null, therefore it can be added to the other terms without changing the sum value :

$$\begin{aligned}\mathbf{x}\,(-\mathbf{K})\,\mathbf{x} &= \sum_i x_i \sum_j k_{ij}\,(x_i - x_j) \\ &= \sum_i \sum_j k_{ij}\left(x_i^2 - x_i x_j\right)\end{aligned}$$

Reversing the indexes i and j, this last form is equivalent to :

$$\begin{aligned}\mathbf{x}\,(-\mathbf{K})\,\mathbf{x} &= \sum_j \sum_i k_{ji}\left(x_j^2 - x_j x_i\right) \\ &= \sum_i \sum_j k_{ji}\left(x_j^2 - x_i x_j\right)\end{aligned}$$

Therefore, adding the two forms together :

$$2.\mathbf{x}\,(-\mathbf{K})\,\mathbf{x} = \left[\sum_i \sum_j k_{ij}\left(x_i^2 - x_i x_j\right)\right] + \left[\sum_i \sum_j k_{ji}\left(x_j^2 - x_i x_j\right)\right]$$

K being *symetric*, $k_{ij} = k_{ji}$, therefore :

$$\begin{aligned}\mathbf{x}\,(-\mathbf{K})\,\mathbf{x} &= \frac{1}{2}\sum_i \sum_j k_{ij}\left(x_i^2 - 2x_i x_j + x_j^2\right) \\ &= \frac{1}{2}\sum_i \sum_j k_{ij}\,(x_i - x_j)^2\end{aligned}$$

For $j = i$, the term of the inner sum is null, therefore it can be eliminated from the sum without changing its value :

$$\mathbf{x}\,(-\mathbf{K})\,\mathbf{x} = \frac{1}{2}\sum_i \sum_{j \neq i} k_{ij}\,(x_i - x_j)^2$$

If $i \neq j$, $k_{ij} \geq 0$ and $\exists\, j \neq i \;/\; k_{ij} > 0$, a node is always connected to at least one of its neighbours with an unbroken bond ($k_{ij} \neq 0$). Thus :

$$\forall\, i,\;\; \sum_{j \neq i} k_{ij}\,(x_i - x_j)^2 > 0$$

Therefore :

$$\mathbf{x}\,(-\mathbf{K})\,\mathbf{x} > 0$$

We then have proved that $-\mathbf{K}$ is *positive definite* and that both methods, SOR and CG, are suitable to solve Eq.4.8.